MODELLING, SIMULATION AND TRAJECTORY CONTROL OF AN AIRBORNE WIND ENERGY SYSTEM FOR WIND POWER GENERATION

A THESIS SUBMITTED TO
THE BOARD OF GRADUATE PORGRAMS
OF
MIDDLE EAST TECHNICAL UNIVERSITY, NORTHERN CYPRUS CAMPUS

BY

MUHAMMAD RAMEEZ RASHID

IN PARTIAL FULFILLMENT OF THE REQUIREMENTS
FOR
THE DEGREE OF MASTER OF SCIENCE
IN SUSTAINABLE ENVIRONMENT AND ENERGY SYSTEMS PROGRAM

SEPTEMBER 2022

Approval of The Board of Graduate Programs

Prof. Dr. Cumali Sabah
Chairperson

I certify that this thesis satisfies all the requirements as a thesis for the degree of Master of Science

Assoc. Prof. Dr. Ceren İnce Derogar
Program Coordinator

This is to certify that we have read this thesis and that in our opinion it is fully adequate, in scope and quality, as a thesis for the degree of Master of Science.

Asst. Prof. Dr. Anna Prach
Supervisor

Examining Committee Members:

Prof. Dr. Murat Fahrioğlu	METU NCC/ EEE	
Asst. Prof. Dr. Anna Prach	METU NCC/ ASE	
Asst. Prof. Dr. Erdoğan Kaygan	GAU/ School of Aviation	

I hereby declare that all information in this document has been obtained and presented in accordance with academic rules and ethical conduct. I also declare that, as required by these rules and conduct, I have fully cited and referenced all material and results that are not original to this work.

Name, Surname: Muhammad Rameez, Rashid

Signature :

ABSTRACT

MODELLING, SIMULATION AND TRAJECTORY CONTROL OF AN AIRBORNE WIND ENERGY SYSTEM FOR WIND POWER GENERATION

Rashid, Muhammad Rameez
Master of Science, Sustainable Environment and Energy Systems Program
Supervisor: Asst. Prof. Dr. Anna Prach

September 2022, 107 pages

Significant progress is being made in developing creative and cost-effective technologies to reduce our dependence on fossil fuels and enable the transition towards renewable energies. Airborne Wind Energy (AWE) systems refer to the generation of useable power by airborne devices such as kites, wing gliders, parafoils, and drones. They can reach higher altitudes and leverage an abundant and previously unused wind resource than a conventional wind turbine. On the other hand, they need far less material to transmit forces of similar magnitude, which could lead to lower system costs and significantly decreased environmental footprint. The thesis mainly focuses on a ground-based power-generating AWE system which generates power using the tether's tension. The main goals of the thesis are to develop a simulation model that accurately represents the three-dimensional flight dynamics of an AWE kite and a control architecture that guides the flight path along the desired figure-of-eight trajectory to maximize the system's potential for power generation. A thorough literature review regarding key AWE concepts, dynamic models and control strategies is presented initially. The kite is modelled as a point mass, assuming a rigid and massless tether. The simulation model is verified by analyzing the system's dynamic response for the roll angle, pitch angle and reeling speed inputs. A two-loop control architec-

ture is developed. The outer loop establishes a reference trajectory using a two-point tracking approach and creates a reference for the course angle. The inner loop tracks the course angle by adjusting the steering input using a PID controller. The effects of system parameters on PID gains and cut-off frequencies are investigated, and they are tuned accordingly to maximize power production. Finally, the system's performance in terms of cycle efficiency is also evaluated.

Keywords: Airborne wind energy, Power kite, Crosswind kite power, Mathematical modelling, Trajectory control.

ÖZ

RÜZGAR ENERJİSİ ÜRETİMİ İÇİN HAVADAN RÜZGAR ENERJİSİ SİSTEMİNİN MODELLENMESİ, SİMÜLASYONU VE YÖRÜNGE KONTROLÜ

Rashid, Muhammad Rameez
Yüksek Lisans, Sürdürülebilir Çevre ve Enerji Sistemleri Programı
Tez Yöneticisi: Dr. Öğr. Üyesi. Anna Prach

Eylül 2022 , 107 sayfa

Fosil yakıtlara olan bağımlılığımızı azaltmak ve yenilenebilir enerjilere geçişi sağlamak için yaratıcı ve uygun maliyetli teknolojilerin geliştirilmesinde önemli ilerleme kaydedilmektedir. Havadaki Rüzgar Enerjisi (AWE) sistemleri, uçurtmalar, kanatlı planörler, parafoiller ve dronlar gibi havadaki cihazlar tarafından kullanılabilir güç üretilmesini ifade eder. Geleneksel bir rüzgar türbininden daha yüksek irtifalara ulaşabilir ve bol ve daha önce kullanılmayan bir rüzgar kaynağından yararlanabilirler. Öte yandan, benzer büyüklükteki kuvvetleri iletmek için çok daha az malzemeye ihtiyaç duyarlar, bu da daha düşük sistem maliyetlerine ve önemli ölçüde azaltılmış çevresel ayak izine yol açabilir. Tez, temel olarak, ipin gerilimini kullanarak güç üreten, yer tabanlı bir güç üreten AWE sistemine odaklanmaktadır. Tezin ana hedefleri, bir AWE uçurtmasının üç boyutlu uçuş dinamiklerini doğru bir şekilde temsil eden bir simülasyon modeli ve sistemin güç potansiyelini en üst düzeye çıkarmak için uçuş yolunu istenen sekizlik yörünge boyunca yönlendiren bir kontrol mimarisi geliştirmektir. nesil. Temel AWE kavramları, dinamik modeller ve kontrol stratejileri ile ilgili kapsamlı bir literatür taraması başlangıçta sunulmaktadır. Uçurtma, katı ve kütlesiz bir ip olduğu

varsayılarak noktasal bir kütle olarak modellenmiştir. Simülasyon modeli, sistemin yalpa açısı, yükselme açısı ve sarma hızı girdileri için dinamik tepkisini analiz ederek doğrulanır. İki döngülü bir kontrol mimarisi geliştirildi. Dış döngü, iki noktalı bir izleme yaklaşımı kullanarak bir referans yörünge oluşturur ve rota açısı için bir referans oluşturur. İç döngü, bir PID kontrolörü kullanarak direksiyon girişini ayarlayarak rota açısını izler. Sistem parametrelerinin PID kazançları ve kesme frekansları üzerindeki etkileri araştırılır ve güç üretimini en üst düzeye çıkarmak için buna göre ayarlanır. Son olarak, sistemin çevrim verimliliği açısından performansı da değerlendirilir.

Anahtar Kelimeler: Havadan rüzgar enerjisi, Rüzgar enerjisi, Yan rüzgar uçurtma gücü, Matematiksel modelleme, Yörünge kontrolü.

To everyone who has supported me through out my education

ACKNOWLEDGMENTS

I would like to extend my sincere gratitude to my supervisor Dr Anna Prach, for her constant guidance, support, and valuable insight and knowledge on the subject matter that steered me through this research.

I am grateful to the department of Sustainable Environment and Energy Systems (SEES) at the Middle East Technical University, Northern Cyprus Campus (METU NCC) for the good fortune of completing my Masters's degree, and the department of aerospace engineering for the valuable experience of working as a teaching assistant.

To all the faculty and staff members of the Middle East Technical University, My gratitude to you for all you have done. I truly appreciate your efforts and the time you spent teaching and helping me on many occasions.

And finally to my family and friends and, most importantly, to my parents. Thank you for always being so supportive and helping me every step of the way

TABLE OF CONTENTS

LIST OF TABLES

TABLES

LIST OF FIGURES

FIGURES

CHAPTER 1

INTRODUCTION

1.1 Global Energy Scenario

Energy is an essential ingredient of modern global society. Our continuous reliance on energy to feed the global demand has significantly increased the primary world energy consumption. The first boom in this increment started with the industrial revolution and has been growing ever since, as seen in Fig.1.1.

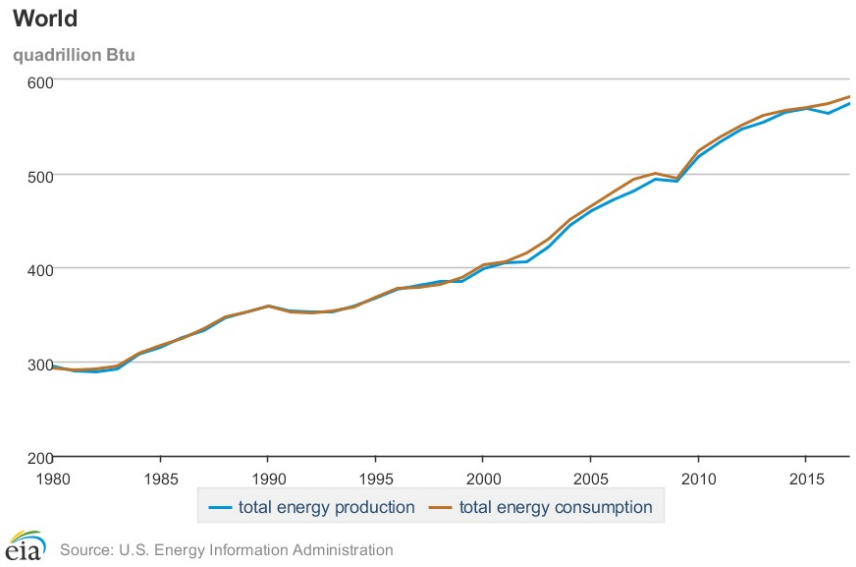

Figure 1.1 Total Global Energy Production and Consumption (Energy Information Administration, 2019b).

Consequently, the demand for production has also increased at the same pace. Although the world is tremendously dependent on the constant supply of energy, many

consumers are unaware of the most basic question. Where does this energy come from? Fossil fuels are the most significant energy source and still dominate the energy market (British Petroleum, 2019). Over the past three decades, a continued increase has been observed in the consumption of fossil fuels. In 2018 alone, oil consumption grew by an average of 1.5%. Natural gas increased by 5.3%, recorded as one of the fastest since 1984, and coal consumption doubled its 10-year average growth, growing by 1.4% (Energy Information Administration, 2019a).

1.2 Carbon Emissions and Climate Change

The excessive burning of fossil fuels in achieving the global energy demand has had many adverse effects on the environment and poses a threat to humanity. Combustion of fossil fuels produces carbon dioxide and other greenhouse gas emissions directly linked to global warming and climate change. Data presented in Figs.1.2 and 1.3 show the relationship between the increase in global atmospheric carbon dioxide emissions and the global mean average temperature rise.

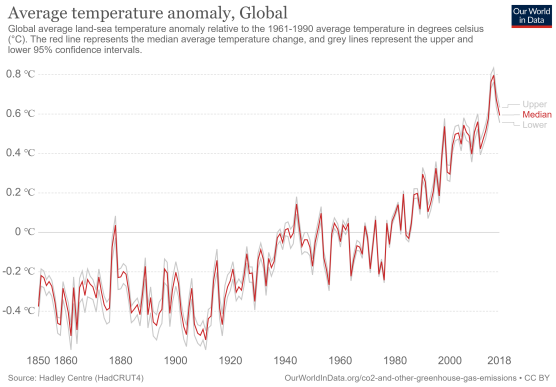

Figure 1.2 Global Average temperature Anomaly (Ritchie & Roser, 2020)

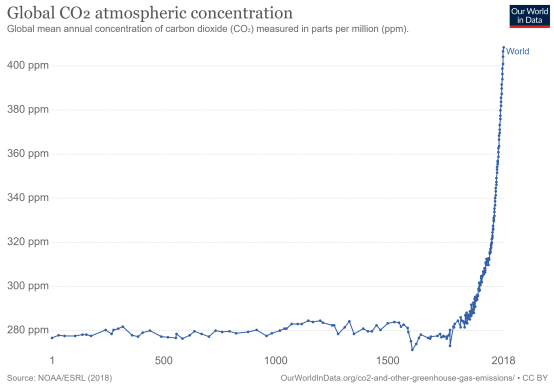

Figure 1.3 Global CO2 concentration (ppm) (Ritchie & Roser, 2020)

Most of the energy used throughout the world is consumed as electrical energy. Traditional sources for electrical power generation are steam power plants, gas and oil-based power generators, and hydroelectric power plants. Most steam power plants burn coal to produce steam, which drives the turbine. The turbine, in turn, runs a

generator to produce electricity. Heavy oil is used in diesel generators to produce electricity, and natural gas-based plants drive a turbine through the direct combustion of natural gas. All of these methods have a significant amount of greenhouse emissions associated with them.

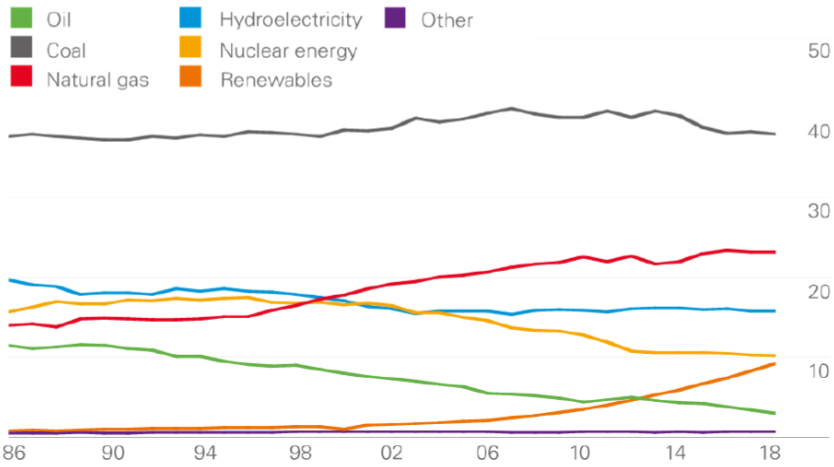

Figure 1.4 Percent share of electricity generation by source (British Petroleum, 2019).

Fossil fuels dominate the global electricity generation mix, as shown in Fig.1.4. Among fossil fuels, coal is the most significantly used for power generation and is the biggest contributor to global CO2 emissions. According to the Intergovernmental Panel on Climate Change's (IPCC) analysis of the literature in 2011, burning coal releases 1 kg of CO2 per kWh of electricity produced. In comparison, heavy oil produces 0.7 kg of CO2 per kWh of electricity, and the number for natural gas is around 0.4 - 0.5 kg of CO2 per kWh of electricity.

1.3 Economic Viability of Renewable Energy

A notable increase in generation capacity by renewable sources has been observed in recent years (Vakitbilir et al., 2022). In 2018, the share of renewable energy in the global electric power generation was recorded at 26% (International Energy Agency, 2019). Research on new renewable energy technologies is essential in making them available in larger amounts and economically and environmentally viable. Low-cost fossil fuels and hindered technological development were major socio-

economic implications for making renewable energy generation unsuccessful in the past few decades. Nowadays, renewables have become the cheapest source of power generation in many parts of the world. In 2018, a noticeable decline was seen in the weighted costs of electricity from all commercially available renewable energy power generation sources. Concentrated solar power, solar photovoltaics, onshore wind and bio-energy experienced the largest declines. For onshore wind generators that started generating in 2018, the average levelized cost of electricity (LCOE) was 0.056 $\mathrm{USD/kWh}$, which is 13% less than in 2017 and 35% less than in 2010 (IRENA, 2019). The cost of onshore wind power is now at the lower end of the cost range of fossil fuels (Rizvi et al., 2022). Fig.1.5 displays a cost contrast for new generating resources' projected Levelized Cost of Electricity, including fossil fuels and renewables entering service in 2025. However, wind energy costs need to decline further to stay economically appealing to investors and consumers.

Plant type	Capacity factor (percent)	Levelized capital cost	Levelized fixed O&M[1]	Levelized variable O&M	Levelized transmission cost	Total system LCOE	Levelized tax credit[2]	Total LCOE including tax credit
Dispatchable technologies								
Ultra-supercritical coal	85	47.57	5.43	22.27	1.17	76.44	*NA*	76.44
Combined cycle	87	8.40	1.59	26.88	1.20	38.07	*NA*	38.07
Combustion turbine	30	16.17	2.65	44.33	3.47	66.62	*NA*	66.62
Advanced nuclear	90	56.12	15.36	9.06	1.10	81.65	-6.76	74.88
Geothermal	90	20.38	14.48	1.16	1.45	37.47	-2.04	35.43
Biomass	83	39.92	17.22	36.44	1.25	94.83	*NA*	94.83
Non-dispatchable technologies								
Wind, onshore	40	29.63	7.52	0.00	2.80	39.95	*NA*	39.95
Wind, offshore	44	90.95	28.65	0.00	2.65	122.25	*NA*	122.25
Solar photovoltaic[3]	29	26.14	6.00	0.00	3.59	35.74	-2.61	33.12
Hydroelectric[4,5]	59	37.28	10.57	3.07	1.87	52.79	*NA*	52.79

Figure 1.5 Estimated LCOE for new generating resources going into operation in 2025, in dollars per MWh) (Energy Information Administration, 2020).

1.4 Wind Energy Potential

The concept of harnessing useful power from wind was used in early civilization to propel sailing vessels initially and to drive windmills for grinding grains. However, it was not until the beginning of the 20th century that a basis for wind energy technology was developed and directly applied to electricity generation, thanks to the pioneering efforts of Albert Betz and others in an emerging industry (Betz, 1926). The power

that can be extracted from wind can be calculated using the following equation;

$$P = \frac{1}{2}\,\rho\,C_p\,A\,V^3 \tag{1.1}$$

where P is the extracted power, ρ is the air density, C_p is the power coefficient, A is the area swept by rotor blades, and V is the free stream velocity of the air. The wind turbine's design and architecture influences access to higher velocities, performance and the rotor area. Keeping everything else constant and only increasing the velocity through a wind turbine increases the power three folds. Wind gradients or velocities near the earth's surface are typically low due to surface friction or no-slip condition and increase with increasing heights above the surface. Escalating hub heights of modern wind turbines minimize the impact of surface friction and enable them to work in high-quality resource regimes with higher wind speeds to extract more power (Veers et al., 2019). The swept area A is another important factor that affects the output power. Scaling the wind turbines to reach higher altitudes and sweep greater areas for maximum power output has significant material investment and capital, operational and maintenance costs.

Wind turbine technology has developed rapidly over the past decade. The data released by the Global Wind Energy Council indicated that the wind energy industry installed 51.3 GW of new capacity in 2018. Despite the growth of the number of wind turbines worldwide, several limitations and challenges restrict the available potential of wind energy resources. A significant engineering problem for the most optimal and efficient operation of wind turbines is the analysis of its huge structural parts that comprise the tower, rotor hub, blades and ground foundation

1.5 Challenges Associated with Wind Turbines

Average ratings of wind turbines have increased almost linearly in the last 20 years. In 1985, the rating capacity of wind turbines was under 1 MW with a rotor diameter of around 15 meters. The average rating in 2012 was 2.5 MW, with rotor diameters spanning 100 meters. Onshore turbines today are about 2.5-3 MW in average size,

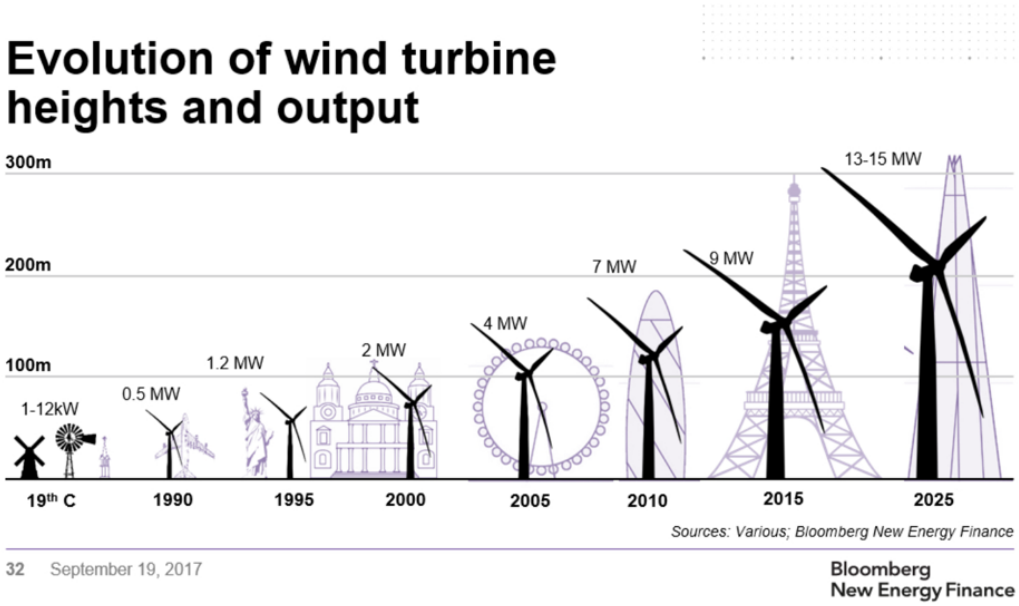

Figure 1.6 Evolution of wind turbine heights and output

with blades approximately 50 meters long. An average offshore wind turbine has a rating of about 3-4 MW. Today's largest wind turbines have a rated capacity of 7.5 MW with rotor diameters of over 120 meters, longer than a football field. 15 MW turbines are planned for the near future, and 20 MW ones are considered possible (EWEA, 2022) theoretically. In general, the challenges associated with modern wind turbine technology start early in the construction phase. They are linked to every subsequent step, including transportation, installation, operations and maintenance, and decommissioning.

The requirement of Wind turbine projects to run smoothly and on schedule is certainly not barrier-free. Nowadays, turbines are designed on a magnificent scale, and designers turn to low-wind turbine technology for less suitable wind sites since many existing wind sites are already in use. The evolving industry creates new obstacles related to uncertain wind and weather conditions and uncertainty over the production and delivery of the equipment. The sites with good wind resources, i.e. near the lakes, wetlands and rocky landscapes, often involve complex Geo-technical parameters. The challenge during construction is to minimize distress to areas while installing the site infrastructure and building turbines safely and efficiently.

A further limiting factor in the growth of wind turbines is land transport. The dimen-

sions of a conventional over-the-road trailer, which is 4.1 m high by 2.66 m wide, are a benchmark for cost-efficient transportation. The weight factor remains under 80,000 lbs gross vehicle weight, corresponding to a cargo weight of approximately 42,000 lbs. Loads over 4.83 m high trigger costly utility and additional assistance. These limits most affect the size and base diameter of wind turbines. The dimensional limitation is even more evident in rail transport (Thresher & Laxson, 2006). Access to the site in terms of land transportation is another major issue.

Increasing the overall size of the turbine has several effects on the assembly and installation of turbines. Average hub heights for larger wind turbines of 2.5-3 MW power output are around 80-100 m, which increase with increasing the rated capacity. As the wind turbine's hub masses and tower heights increase, tower diameters and shell thickness must increase to safely support the bending and buckling loads. Both these factors increase the associated costs. Crane costs are expected to run from $ 40,000 to $ 50,000 for installing a 2.5 MW turbine on a 110 m tower. while costs could be as much as $ 138,000 to upright a 5 MW turbine on a 156 m tower. Other restrictive factors are that cranes of this lifting ability are scarce, difficult to transport, require large crews and are expensive to mobilize, assemble and dismantle (Thresher & Laxson, 2006).

Massive foundations are required to support large wind turbines. Typically, concrete with a blend of Portland cement and other aggregate materials are used in construction for the foundations of wind turbines (Berndt, 2015). A significant amount of CO2 is generated in the production of Portland cement and accounts for 5-7% world's human-induced CO2 emissions (Worrell et al., 2001). The contribution of reinforced concrete foundations to material component emissions for a 2 MW onshore wind turbine is 24% (Martínez et al., 2009). Whereas, for offshore 2 Wind Turbines with Concrete Gravity Base Foundations, Reinforced Concrete and Ballast Contribution to Climate Change Impact of Material Components were determined as 37% (Birkeland, 2011).

Wind turbines are mega engineering structures designed to function regularly, under constant complex loads, for a lifespan of 20 years or more. The Blade lengths of such structures reach 80 meters, and towers are well over 100 meters high, sometimes

over 200 meters high, equivalent to a 60-floor building. To put these dimensions in perspective, three A380-800 Airbuses, each with a wing span of 80 m, could fit within one wind turbine rotors swept area.

As turbines become larger, addressing necessary issues such as changing aerodynamic loads, rotor wakes, and the aero-elastic behaviour of massive flexible structures to extract useful power from the wind becomes challenging. The rotor of a 1.5 turbine is about 70 metres, whereas, A 3 turbine has a rotor diameter of approximately 99 m. While the length of the blade is increased by only 41%, the blade root flap bending moment can rise by 160% (Malcolm & Hansen, 2002). The physical models are further complicated by the structural dynamics of composite materials and significant non-linear bending (Stäblein et al., 2017). The blade should be flexible enough to adapt to shifting wind patterns, stiff enough to avoid coming into contact with the tower, durable for at least two decades, and have a surface finish that is resistant to erosion from moisture and dirt, all of which have a substantial cost associated with it.

The materials used in 1990s-era blades, based on affordable composite fibres and sturdy epoxy resins, are still used in modern blades (Cousins et al., 2019). The turbine's overall efficiency is thus reduced due to reasons such as icing of the blades, insects and erosion through abrasive particles. Beyond blades, to prevent the failure of other essential components such as mechanical drives, bearing and bearing load supports and electrical drive components require significant maintenance operations (McKenna et al., 2016). The costs of operation and maintenance represent a considerable proportion of the wind turbine's overall annual costs. Operations and maintenance costs can easily account for 20% - 25% of the total level costs per kWh produced for a new turbine over the turbine's life.

CHAPTER 2

LITERATURE REVIEW

2.1 Introduction to Airborne Wind Energy (AWE) Systems

Developing new strategies to utilize high-altitude wind energy has been the subject of ongoing research in recent years. Miles Loyd pioneered the idea of airborne wind energy (Loyd, 1980). His work at the Lawrence Livermore National Laboratory was inspired by the energy crises of the late 1970s. His revolutionary concept redefined the boundaries of wind energy science. The basic idea was to build a machine to extract energy from the wind without a tower connected to the ground by a tether, similar to a kite. The fundamental motive behind such a device is very straightforward: the outermost region of the blades is aerodynamically the most effective component of a wind turbine since it extracts wind energy from the most efficient swept area. The outer 30% of the blades produce more than half of the total power (Diehl, 2013). The theory was to utilize only the efficient tip part and eliminate the rest of the inefficient structural parts of the blades and the tower itself by a tether. This gave rise to a new generation of wind energy systems known as AWE systems. An illustration of such a system is presented in Fig.2.1.

AWE thus refers to power generation by airborne platforms such as kites, wing gliders, para-foils, or aircraft. AWE systems use airborne platforms that either fly through the air or are tethered to the ground. The power is generated either as a traction force that can be used for mechanical purposes, such as moving a vehicle or a sea vessel, or in the form of electricity. This definition completely redefines the realms of wind energy. The area swept by the wind energy system is no longer subject to any direct limitations, as was previously limited by the diameter of a wind turbine rotor. AWE

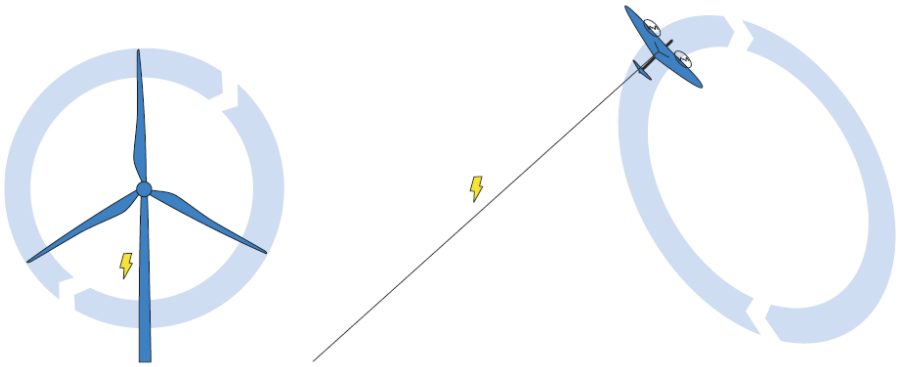

Figure 2.1 An AWE system in comparison to a conventional wind turbine (Diehl, 2013).

devices can sweep larger areas using far less material to optimize the total energy output. The exclusion of large foundations, towers and blades leads to significantly lower system costs. The cost of massive structural elements is half the total wind turbine capital costs, which comprise most of the overall wind energy costs. AWE devices can also operate at higher altitudes where winds are more consistent and stronger than those near the ground. They can easily reach 300-600 meters in altitude, which is twice to four times the height of a standard wind turbine tower (Zillmann & Bechtle, 2018). A distinctive feature of AWE systems is mobility, which allows them to be deployed at various locations both on- and offshore, including moving ground or sea vehicles. Thus, AWE systems have great potential to complement the existing wind energy systems as a cost-effective, sustainable energy source with a lower environmental footprint.

2.2 Crosswind Kite Power

Crosswind refers component of the wind velocity vector that is perpendicular to the direction of travel as sketched in Fig.2.2. Direct crosswind motion occurs when an AWE system flies in an orientation where the tether is parallel to the wind. The potential power that may be generated increases significantly as the apparent speed through the air of the airborne system is increased above the wind speed. For example,

every recreational kite flyer or kite surfer knows that the tension in the lines increases dramatically as soon as a kite begins to fly quickly in the crosswind direction. Hobby kite flyers use their hands to actively counteract the tension, whereas kite surfers make use of the powerful crosswind to reach great speeds and pull off amazing feats.

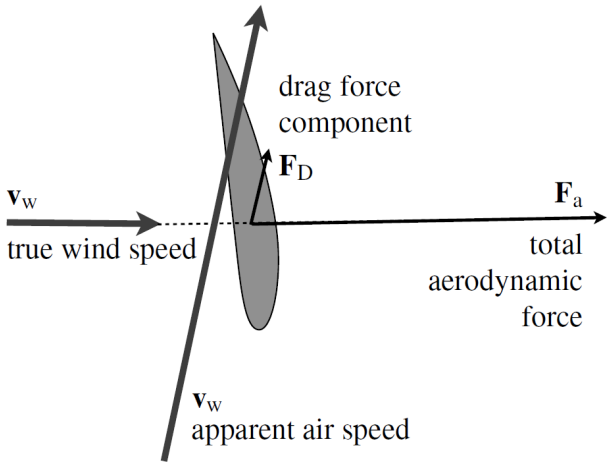

Figure 2.2 Sketch of a wing in crosswind motion (Diehl, 2013).

The observation stated above is supported by the fact that an airfoil's aerodynamic lift force is directly proportional to the square of the velocity, or more precisely, with apparent airspeed experienced at the airfoil.

$$F_{Lift} = \frac{1}{2}\,\rho\,A\,C_L\,v_a^2 \tag{2.1}$$

Where ρ is the air density, A is the airfoil area, v_a is the apparent airspeed at the wing, and C_L is the lift and drag coefficient. As a result, the power output of a kite flying in crosswind motion is substantially higher than a kite maintained motionless in the sky. An AWE system flying in the crosswind direction with a ten times faster velocity than the wind speed will increase the lift and drag forces by a factor of a hundred. It is vital that the atmospheric wind can sustain the kite's high speed and that either the speed of the kite itself or the tension in the tether can be used to capture a portion of the enormous energy that the flying wing may theoretically extract from the wind field.

Miles Loyd was the first to investigate the idea of generating power by airborne devices flying fast in a crosswind direction. He estimated the amount of power flying tethered wings could generate, a concept he called "crosswind kite" (Loyd, 1980). The main idea is as follows; an AWE system flying fast loops on circular trajectories in a crosswind direction while being connected to the ground with a tether significantly increases the Power output. The power is generated either by pulling a load on the ground using the tether tension, which he titled the lift mode of power generation or by using the high apparent wind speed to operate a small turbine mounted on the flying device, which he called the drag mode. The classification of lift and drag modes is presented in further detail later in Section 2.5.

Loyd calculated the theoretical power that can be extracted from the wind by a tethered AWE system in either lift or drag mode under idealized conditions as

$$P = \frac{2}{27}\,\rho\,A\,v_w^3\,C_L\,\left(\frac{C_L}{C_D}\right)^2 \tag{2.2}$$

where A is the wing area, v_w is the wind speed, and C_L and C_D are the lift and drag coefficients. Theoretically according to (Diehl, 2013) , a conventional wing with C_L = 1 , C_D = 0.03 , and operating at a wind speed of 13 $\mathrm{m/s}$ wind would produce 217 kW of power per m^2 of wing area. The tether drag, however, is pretty substantial, so this is not realistic. A more accurate estimate of the overall drag coefficient would be, for instance, C_D = 0.07, resulting in a theoretical power output of 40 $\mathrm{kW/m^2}$ of wing area. Although none of the competitive AWE firms or research teams has experimentally achieved this high power density, it has been confirmed by thorough computer models and seems plausible.

Using Eq.(2.2) to calculate an AWE system's power output and compare it to a large-scale wind turbine is interesting. Diehl (Diehl, 2013) Considered an AWE system has a tethered wing that is comparable in scale to the wing of an Airbus 380. let the wing have a lift of C_L = 1 and a drag of C_D = 0.07, including the effects of the tether drag. The wing has a wing span of 80 m and an area of A = 845 m^2, weighing about 30 tonnes and operating at a wind speed of V_w = 13 $\mathrm{m/s}$. Theoretically, a wing of such dimensions could generate about 34 MW of power. To support the loads on the wing, assume a modern fibre tether with a tensile strength of 1 GPa. The corresponding tether would require a cross-sectional area of 90 cm^2, or a diameter

of 11 cm. If the wing flies at an altitude of 500 m with an elevation angle of $30°$, it would require a tether length of 1000 m, yielding a tether volume of 9 m^3 and a weight of about 9 tonnes. The system would generally require an airborne mass of 39 tonnes to generate 34 MW. To be more realistic, the hypothetical power production is reduced to 30 MW.

The power output is then compared to one of the biggest wind turbines operational today, The Enercon E-126 of 7.5 MW rated power. The power output of 30 MW is the equivalent of four such turbines. Each turbine has three rotor blades weighing 65 tonnes with a rotor diameter of 126 m. Therefore, only the 12 blades of these four turbines weigh 780 lb, 20 times as much as the AWE system itself. if the weight of the tower and other components is accounted for, the total weight of the turbine soars to 12 400 tonnes, 300 times the weight of the AWE components. Thus it can be assumed that, for both the systems, the electrical generators are comparable in size and that the foundations required for the AWE system are much smaller. This results in substantial savings in material costs (Diehl, 2013).

2.3 Power and Efficiency Analysis of AWE systems

It is important to define a metric to analyze the performance of an AWE system based on the useful power output. The energy extracted from the wind is limited by the Betz limit for conventional wind energy systems. However, for AWE systems, the analysis is not so simple. Determining the area from which an AWE system can draw power is not a straightforward task. After each pass of an AWE system through its trajectory, the area has time to restore its airflow. The kite's performance, measured in terms of its aerodynamic efficiency (C_L and C_D), and its mode of operation determines its swept area.

The theoretical maximum power that can be generated from the wind by an AWE system is given by Eq.(2.2). It can be re-arranged and written as

$$\begin{aligned} P &= \left(\frac{1}{2}\,\rho\,A\,v_w^3\right)\left(\frac{4}{27}\frac{C_L^3}{C_D^2}\right), \\ &= \left(\frac{1}{2}\,\rho\,A\,v_w^3\right)\zeta\,. \end{aligned} \tag{2.3}$$

The term in the first bracket is the kinetic energy of wind per unit time passing through a cross-sectional area A of the kite, and ζ is the power harvesting factor (Diehl, 2013). It is intriguing to compare the power harvesting factor with the Betz limit, which establishes a ceiling on the amount of power that may be drawn from a particular cross-section of the wind field. Current wind turbines are close to reaching the Betz limit, which is $\frac{27}{16}$. Therefore, the value $\frac{27}{16}\zeta$ can be interpreted as the additional power that a wing of size A can harvest compared to a wind turbine of the same swept area A.

Highly efficient modern wings with a lift coefficient of 1 and a drag coefficient of 0.07 have power harvesting factors as high as 30. This is still a theoretical number and has not yet been realized in real-life applications. For an AWE system, the maximum acquired power harvesting factor is 8, as reported by Makani. Rigid wings have a high power harvesting factor due to their high lift-to-drag ratios. For flexible wings, the values are typically lower, around 5.

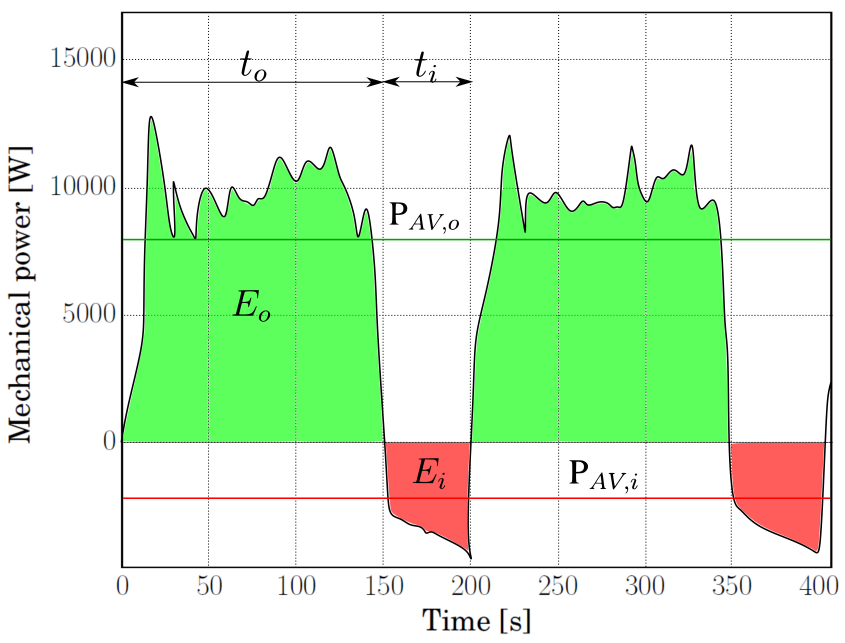

Figure 2.3 Illustration of mechanical power output for two power cycles

.

A more appropriate and systematic approach to determine the system's performance is given (Fechner & Schmehl, 2013). A power output of an AWE system is illustrated

in Fig.2.3. The efficiency of the complete power cycle is determined as a ratio of the reel-out time over the complete cycle time. The ratio is termed the duty cycle. The reeling speeds determine the duty cycle. Higher duty cycles refer to longer traction phases hence the system spends more time producing power than consuming power. The duty cycle is defined as

$$D = \frac{t_o}{t_o + t_i} \,. \tag{2.4}$$

The system consumes a certain amount of energy while reeling in the tether. The system's efficiency in terms of the mechanical energy generated at the ground station vs the energy consumed is termed the pumping efficiency (η_p) over the whole cycle. It is calculated as the ratio of net mechanical energy over the energy generated in the traction phase.

$$\eta_p = \frac{E_o - E_i}{E_o} \,. \tag{2.5}$$

The average mechanical power over the complete power cycle can now be determined as

$$P_{AV,cyc} = D\, \eta_p\, P_{AV,o} \,. \tag{2.6}$$

The cyclic efficiency of the system is given as

$$\eta_{cyc} = \frac{P_{AV,cyc}}{P_{AV,o}} = D\, \eta_p \,. \tag{2.7}$$

The cyclic efficiency is considered a good performance metric to evaluate the performance of a pumping AWE system. Other efficiencies related to the electrical machinery at the ground station are also considered to find the total efficiency of the system.

2.4 The Wind Window

The wind window is a fundamental concept in kitesurfing which is widely applicable in AWE systems. The window defines the flight envelope of the kite as shown in Fig.2.4. It is positioned on the downwind side and is a half dome in shape. The dome's radius is the distance between the ground station and the kite, which is the tether length. The kite's position within the window is defined using the elevation (θ) and azimuth (ϕ) angles.

The window has different power zones. The area in front of the ground station, directly downwind, is the high power zone marked in red. A kite flying in this area moves quickly and produces the greatest force. As the kite is moved away from this downwind area, either moving up or across the window, it enters the medium power zone coloured in red. As the kite moves further downwind, it reaches the low power zone. The leading edge of your kite will quickly fly forward in the power zones. The kite then slows down as it reaches low power.

Generally speaking, if the kite is turned using gentle steering movements, it should stay at low power. These small steering movements mean that the leading edge always points towards the low power zone. However, when a kite is turned more sharply, the leading edge will aim deeper into the wind window. Also, in stronger wind, the power zones are expected to expand. In light wind, the power zones retract, and the kite needs to sit deeper in the window to support its own weight. To help get a

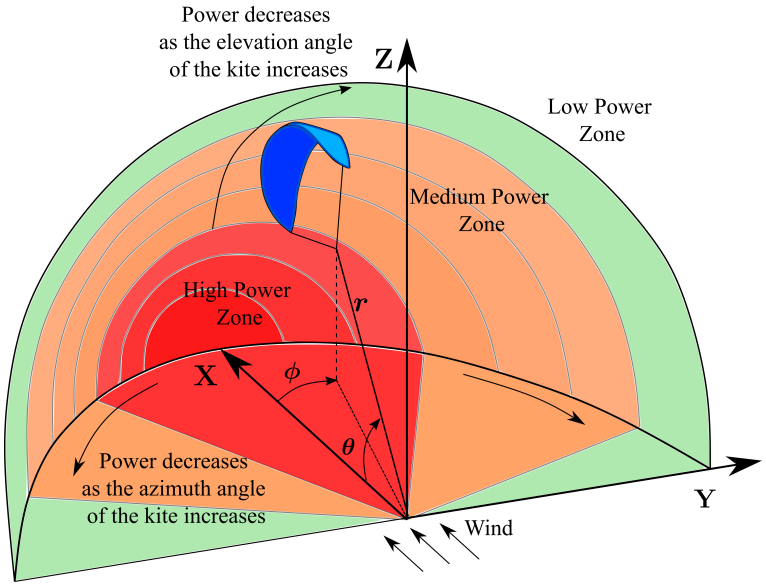

Figure 2.4 The wing window

better understanding of why the power zones are where they are, the wind window is analyzed from the cross-wind direction, as illustrated in Fig.2.5. It can be seen that a kite positioned downwind, at high power, cuts across the path of the wind. In the low power zone, a kite positioned near the edge of the window lines up with the wind and interacts less with the airflow. Another reason for high power being downwind is the kite's flying speed. The kite moves much faster in the high power zone. As the kite

flies faster, there is a drastic increase in the airflow across it and the pull from it.

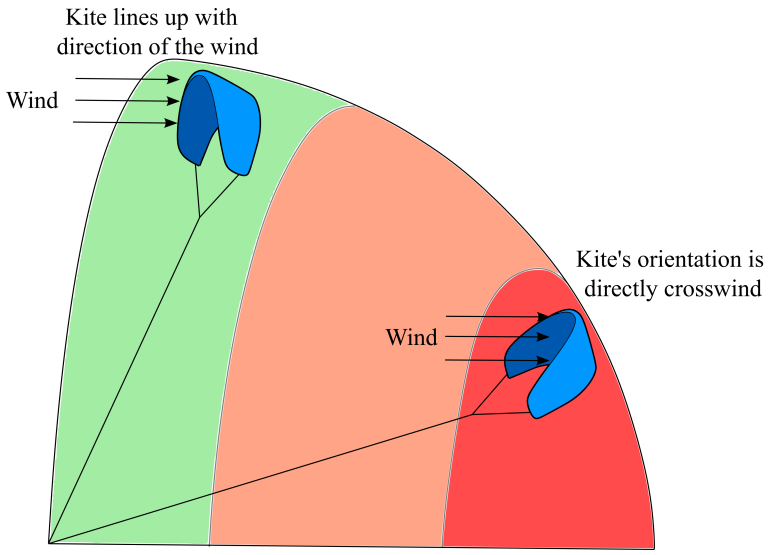

Figure 2.5 The wing window from the cross wind direction

2.5 Classification of AWE systems

AWE systems are generally classified into two broad categories; a categorization based on the mode of power generation, as shown in Fig.2.6, and a classification based on the structure of the AWE system as shown in Figs.2.7 and 2.8. It has already been established that an AWE system has three main components, a ground station, at least one flying system and a tether that connects the airborne system to the ground. Systems that produce power on board the aircraft are termed on-board power generation systems (Diehl, 2013) or in some literature as Fly-Gen AWE systems (Cherubini et al., 2015). Ground-based generation systems or Ground-Gen AWE systems produce power on the ground. Based on structure, AWE systems might have flexible or rigid wings. Because most AWE systems are denser than air, they depend on aerodynamic lift force to maintain their altitude. A few AWE systems are lighter than air and can remain passively in the air. All of the above classifications are individually defined in this section.

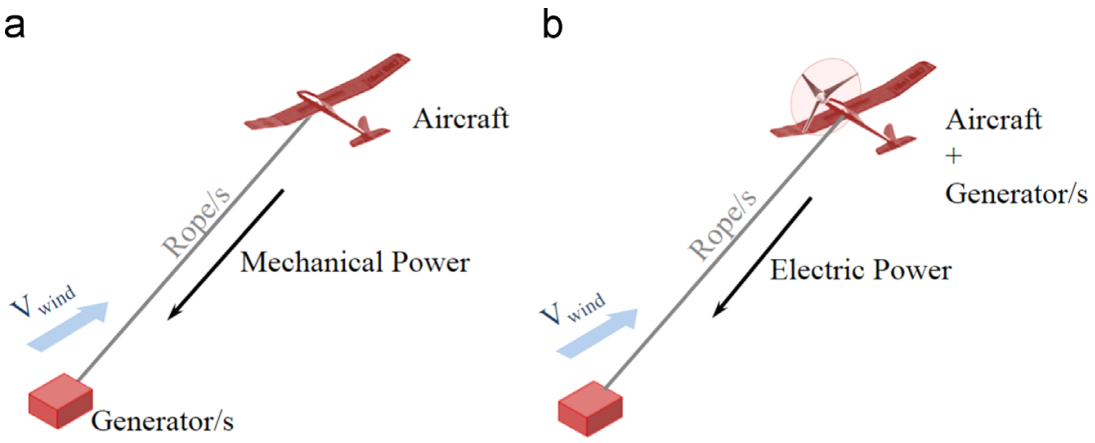

Figure 2.6 An illustration of (a) Ground based power generation and (b) On board power generation (Cherubini et al., 2015).

2.5.1 On-board power generation - Drag mode

On-board power generation systems produce electrical power through turbines mounted on the flying aircraft. Power is generated using the high apparent wind speed to drive the turbine and transmitted to the ground through an electric cable that simultaneously acts as a tether. Since the turbine induces an extra drag, this power generation mode is also called drag mode (Loyd, 1980). The concept of on-board power generation was first patented in 1976 (Payne & McCutchen, 1976) since then, many teams and companies are currently working on different concept designs for on-board AWE systems, as shown in Fig.2.7. A significant advantage of the on-board power generation system is the constant power production during its operation except for take-off and landing maneuvers which consume energy instead. Using the standard available quad-rotor control technology, the turbines can be used in motor mode for stable take-off and landing maneuvers. For the downsides, tether drag is a major issue since the tether in such systems needs to transmit significant amounts of power and withstand the strong tension force. Such systems need a high voltage cable with increased isolation to minimize the ohmic losses. Contrarily, isolation expands the diameter of the tether, which significantly increases the system's tether drag. The weight of the onboard turbine is also a major obstacle in designing On-Board AWE power generation systems.

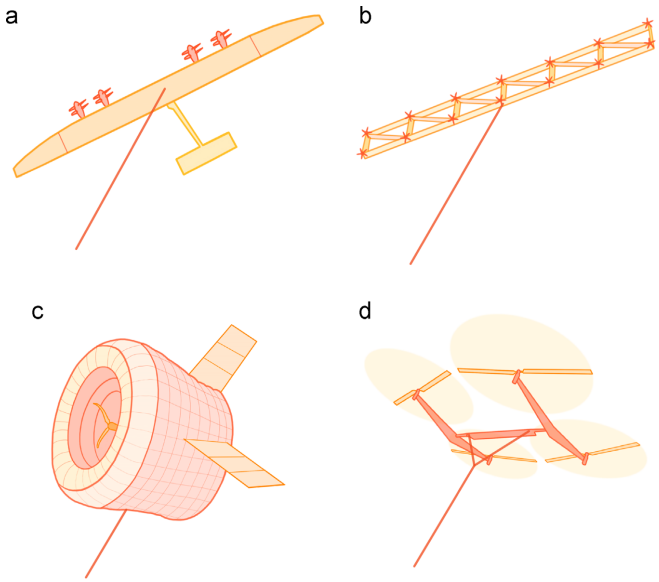

Figure 2.7 Different concepts of on-board power generation AWE systems. (a) A four-turbine drone design (b) A flying frame composed of wing segments and onboard turbines (c) A wind turbine mounted in the centre of an autonomous lifting aerostat (d) An Auto rotating quadrotor.(Cherubini et al., 2015).

2.5.2 Ground based power generation - Lift Mode

Another concept of generating power from fast-flying tethered air crafts is to use a strong tether instead of a high voltage electrical cable. Examples of some tethered wings are shown in Fig.2.8. The mechanical work of a traction force delivered through the tether from the aircraft to the ground station results in the production of electrical energy. Since the conversion to electrical energy is achieved on the ground, this concept is termed ground-based generation or traction power generation (Diehl, 2013). It is also called lift mode when power is generated using crosswind motion (Loyd, 1980). Ground-based generators are further classified as fixed ground stations and moving ground stations. Moving ground systems are considerably more complicated, and no functioning prototype has yet been created. Most of the research in academics and private institutions focuses on fixed ground generation systems. As the name suggests, fixed ground stations are fixed on the ground and produce power by the winch's constant winding and unwinding motion to drive the electrical generator. Net power is produced in a two-phase cycle: a generation or production phase

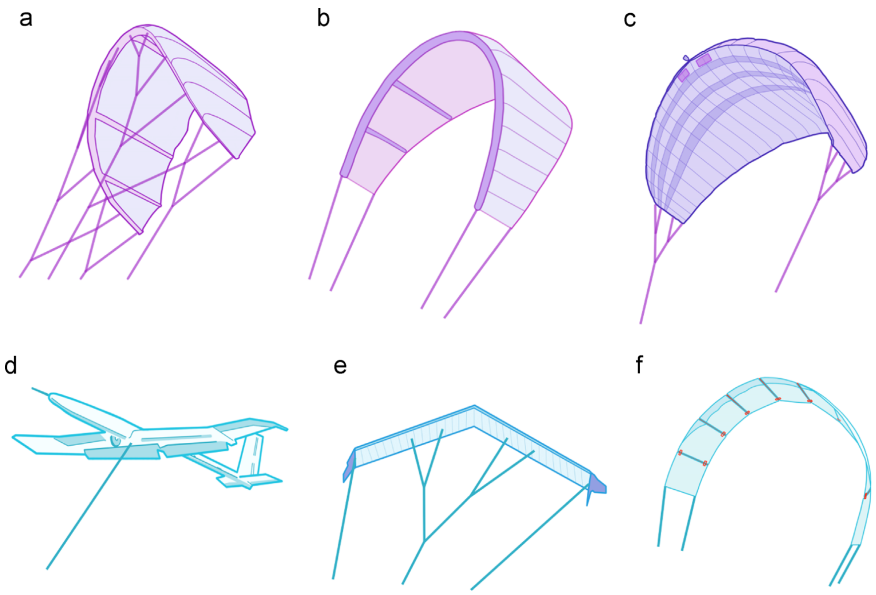

Figure 2.8 Different wing concepts in a ground-based generation. (a) Leading Edge Inflatable (LEI) kite, (b) LEI C-kite, (c) Foil kite, (d) Glider, (e) Swept rigid wing, (f) Semi-rigid wind (Cherubini et al., 2015)

in which energy is produced and a recovery or retraction phase, which consumes a small amount of energy. During the production phase, the aerodynamic lift procured due to the crosswind motion of the aircraft produces strong traction or an unwinding/pulling force on the tether, which drives the electrical generators. Since the tether constantly unwinds around the winch to produce power, the power-producing phase is also termed the reel-out phase in the literature. The electrical motors rewind the tether around the winch in the recovery or reel-in phase to bring the aircraft to its original position for the next generation cycle. A schematic of generation and recovery phases is shown in Fig.2.9. Pumping mode is another term for ground-based power production.

The power produced during the production phase must be greater than that consumed during recovery for a net positive energy balance. An efficient operation of an AWE system is highly dependent on a control system that enhances the aircraft's aerodynamic characteristics and controls its flight path. The optimum flight path consists of high-speed loops in the reel-out phase and the dive or plunge movement of the aircraft towards the ground during the reel-in phase. These maneuvers are performed

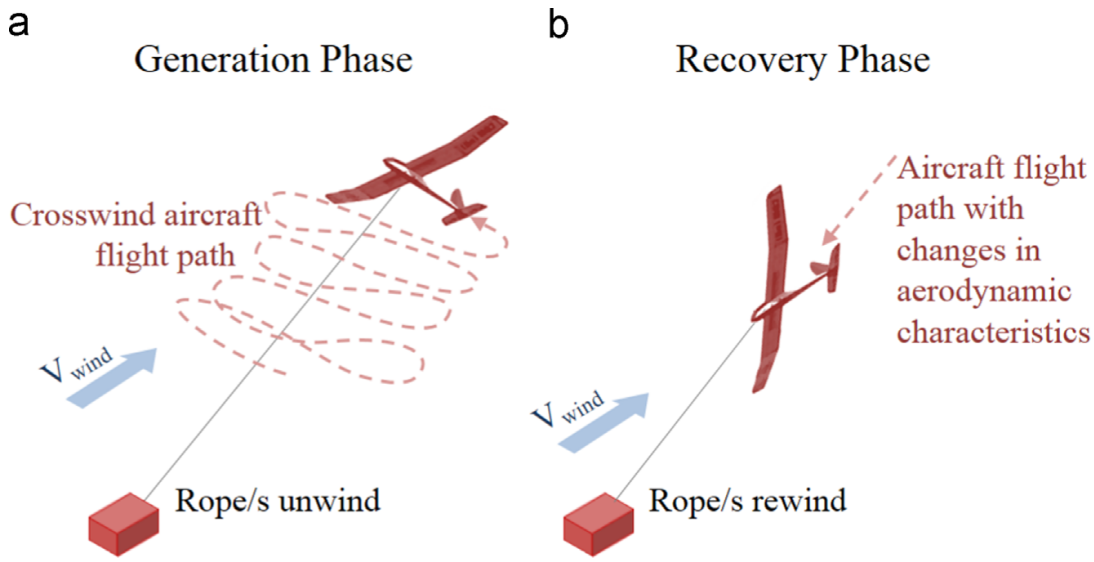

Figure 2.9 A schematic of generation (reel-out) and recovery (reel-in) phase for a ground-based AWE generation system.(Cherubini et al., 2015)

in high crosswinds and are heavily dependent on automatic control for efficient execution and maximum power production. Different types of control mechanisms used in ground-based power generators are shown in Fig.2.10.

2.5.3 Flexible vs rigid wings

Another basic classification category is based on the structure of AWE system airfoils. Some airborne systems have a light and flexible wing that appears very similar to kites and parasails, while others have sturdy rigid bodies that resemble drone air crafts or mimic the tips of a wind turbine blade. Flexible wings maintain their form because of the uniform distribution of the aerodynamic loads. For a specific surface area, they may be incredibly lightweight. The lightweight characteristics and moderate flight speeds of such wings render them safe in the event of a crash, enabling them to operate close to human populations. Most AWE systems with ground-based power generation use different variations and concepts of lightweight flexible wings.

Contrary to flexible wings, rigid wings retain their form irrespective of the airflow. They need more mass for a given wing surface area and are consequently heftier. Due

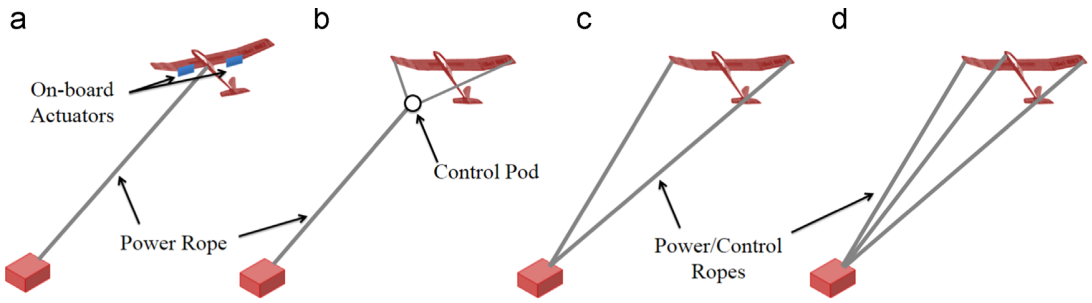

Figure 2.10 Illustration of flight trajectory control by (a) On-board actuators, (b) On-board control pod, (c) Power ropes used for control action and tension transmission (d) Power ropes with additional tether for tension transmission (Cherubini et al., 2015)

to their high lift-to-drag ratios, they can achieve very high speeds with considerably higher power output per wing area. However, the increased weight and higher velocities also increase the risk of severe damage in a crash event. On-board power generation systems utilize rigid wing-type air crafts to support the weight of onboard generators.

2.6 System Models In The Literature

In recent research, the concept of generating electrical energy from high-altitude winds using flexible winged kites connected to a fixed ground station using a strong tether is also known as the Ladermill, as shown in Fig.2.11. The Ladermill concept was first proposed by Dr W.J Ockels in 2001 (Ockels, 2001). Research on the Ladermill concept began during 2004-2006, followed by publishing the first academic papers (Breukels & Ockels, 2005; Lansdorp & Ockels, 2005; Lansdorp et al., 2005). The first successful test of a Ladermill prototype was successfully conducted in 2007 (Lansdorp et al., 2007)

As mentioned in section 2.5, AWE systems are characterized into two main categories based on power generation and structure. The literature reviewed and the models presented in this section are based on AWE systems with ground-based power generation

and flexible tethered wings.

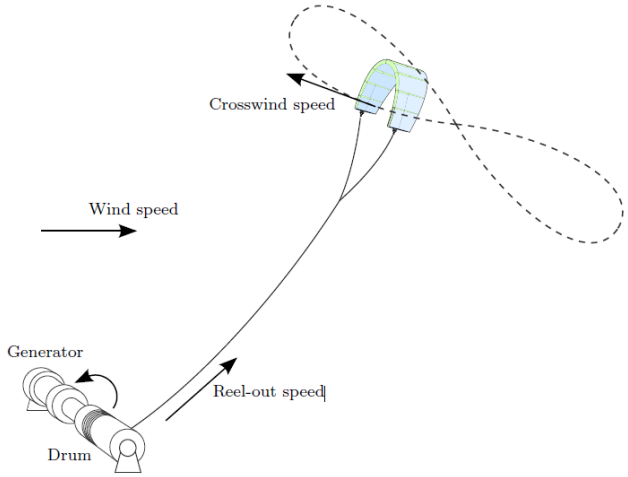

Figure 2.11 Ladermill concept with a LEI-kite(De Groot, 2010)

2.6.1 Point mass model

A point mass is the most basic approach for modelling an AWE system. A Point mass modelled as a simple 2 or 3 degrees of freedom model assumes that all the forces act on the kite's centre of gravity. The model does not consider inertia effects, attitude dynamics and flexible modes. Such a rudimentary model is beneficial for early inspections of flight trajectories and approximating the kite's power output. It is not suitable for higher-order, more precise simulations. The model, however, still manages to attain a reasonable level of detail and can be implied for quicker, real-time simulations. The simpler models are more suitable when it comes to analytical tasks like optimization and control design. Some examples of point mass models used in the literature are present in (Diehl et al., 2001; Houska & Diehl, 2007; Ockels, 2001; Williams, 2006)

Figure 2.12 presents a basic demonstration of a point mass model with the apparent velocity V_a, lift force vector L, drag force vector D, tether tension T_t and weight of the kite W. The drag force is defined such that it always acts parallel to the apparent velocity vector with zero side slip, whereas the direction of the lift force is always

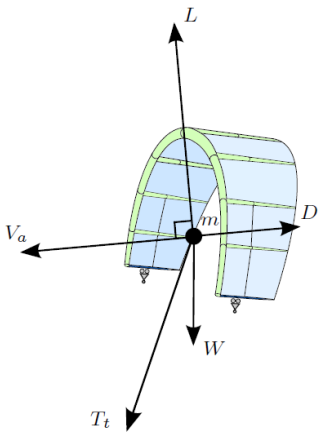

Figure 2.12 Point mass model of a LEI-kite (De Groot, 2010)

perpendicular to the apparent velocity vector. The orientation of the lift vector is determined by the roll movement of the kite relative to the aerodynamic velocity vector. The kite's trajectory is guided by changing the angle of attack and roll angles, i.e manipulating lift and drag vectors.

2.6.2 Four-point mass model

A more realistic and robust model is presented by Fechner (Fechner et al., 2015). A four-point kite model is a straightforward particle-based system with rotational inertia on every axis. Fig.2.13 illustrates a simple four-point mass model with the four points defined as A, B, C and D. Points P_0 to P_{KCU} discretize the tether into finite line segments, where the subscript KCU stands for the kite control unit and marks the location of the control pod. The kite's mass is split among points A, B, C, and D. The aerodynamic forces are computed separately for each point. The total aerodynamic force gives the net effect of the forces acting on the system. Other modelling parameters such as the mass of the tether and the control unit's mass are also considered. Such a modelling frame is considered more accurate and robust and allows the model to help better estimate the effect of gravity and inertia on the steering response. It is also more stable even at low tether forces.

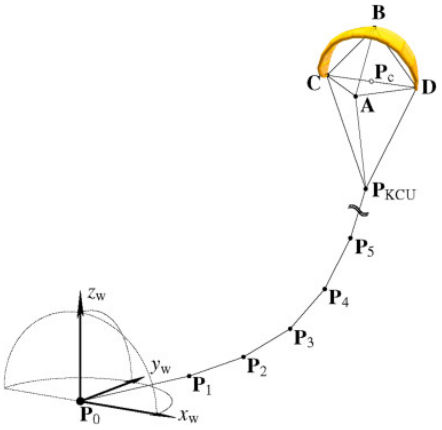

Figure 2.13 Four point kite model (Fechner et al., 2015)

2.6.3 Rigid body models

A rigid body is a perfect representation of a finite solid body that ignores any internal distortion in its shape or structure. Rigid body models, as opposed to point mass models, consider the orientation of the kite and, as a result, take into account the inertia qualities and attitude dynamics. A common practice in flight dynamics and control literature is to model aircraft as rigid bodies with 6 degrees of freedom, three for translation and three for rotation. The system is modelled so that the forces and moments applied to the body result in the required outputs of position, velocity, attitude, and angular velocity. The accuracy of such models depends on the modelling of the aerodynamic parameters. The exact approach may also be used to model surf kites for AWE systems. Such models allow for the dynamics of the kite to be controlled via the applied forces and moments, making them more suitable for the application of low-level control design.

A method for simulating a surf kite as a rigid body with six degrees of freedom is described by Paul Williams (Williams, Lansdorp, Ruiterkamp, et al., 2008). The method is similar to the modelling techniques used in rigid body flight dynamics. However, basic flight dynamic models do not address the impact of a kite's arc shape on aerodynamics. The aerodynamic forces and moments acting on the kite are modelled using the aerodynamic derivatives. An impediment to using such models is that the aerodynamic derivatives need to be determined experimentally or estimated by im-

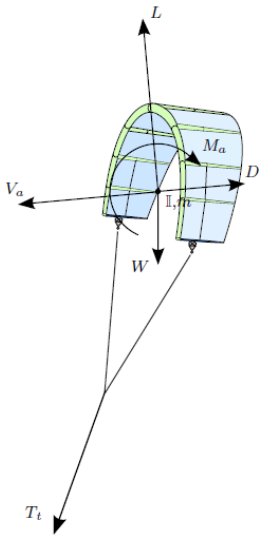

Figure 2.14 An illustration of a rigid body model (De Groot, 2010)

plementing complex computer simulations such as the Vortex Lattice Method (Melin, 2000). Six Degree of freedom rigid body models are used in the literature by (De Groot, 2010; Gros et al., 2013; Liu et al., 2020)

Boris Houska proposed a 9 degree of freedom model that combines a rigid body model with a point mass model, accounting exclusively for the inertia of the tether and ignoring the inertia of the body. According to Houska, since kites are relatively lightweight structures, the effects of kite body inertia can be neglected. The tethers and partly the control mechanism are the principal contributors to the mass of the entire system. This model's aerodynamic forces and moment functions are also described using effective aerodynamic derivatives, much like in the six degrees of freedom models. The limitations to the application of point mass and rigid body models are more perceptible by noticing a kite does not create directional changes solely due to pitch, roll or yaw steering actions. In reality, the kite continuously undergoes structural deformations during its flight. Such structural deformations produce further changes in the position and orientation of the aerodynamic forces and moments, as well as changes in inertia characteristics.

2.6.4 Higher order models

A way to obtain more precise simulations is to use models with a higher order of accuracy that thoroughly considers the kite's structural deformations. Examples of high fidelity models are multi-plate models, lumped parameter models, multi-body dynamic models and finite element method (FEM) models.

The multi-plate model attempts to simulate a kite's continual deformation in response to control inputs, which rigid body kite models ignore. Accounting for such deformations makes it difficult to determine the angle of attack, the side slip angle, and the location of the centre of gravity, which is no longer fixed. In 2007, Williams (Williams et al., 2007) proposed modelling the arch-shaped construction of a surf kite with two flat plates joined by a friction-less hinge, as shown in Fig.2.15a. The movement of the plates is coupled through translation and rotation via the hinge. The kite's shape is roughly approximated by enabling each plate to have a varied pitch and roll angle. Modelling accuracy can be increased by extending the concept of two plate kite model to a multi-plate model, as shown in Fig.2.15b. Due to the coupled nature of the plate, the equations of motion are derived using the Lagrangian approach for simplicity. For modelling simplicity, the equations of motion are determined using the Lagrangian method due to the coupled structure of the plate. However, an analytical solution to the equations of motion is highly challenging due to their tremendous complexity and non-linearity.

The four-point mass model presented in Section 2.6.2 is further expanded by segmenting a kite as a collection of point masses linked by visco-elastic spring elements to simulate the elastic behaviour of a kite in response to steering inputs. The method suggested by Furey (Furey & Harvey, 2007) is also known as the particle-based simulation or lumped parameter method. The point masses are connected to each other with constraints as shown in Fig.2.16.

Still, higher-order models of extreme complexity are multi-body models. The study of multi-body systems examines the dynamic behaviour of linked rigid or flexible entities, each capable of experiencing significant translational and rotational motion. Breukels(Breukels & Ockels, 2008) developed a multi-body kite model using the

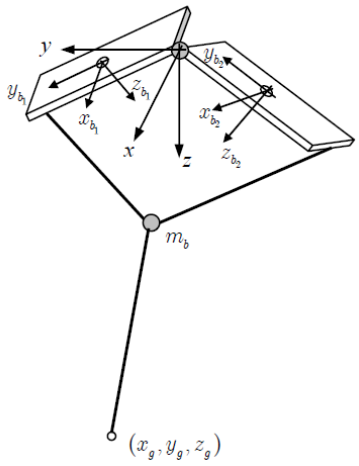

(a) A simple two plate kite model (Williams et al., 2007)

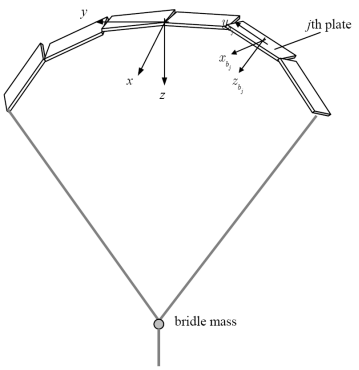

(b) Multi-plate kite model (Williams, Lansdorp, Ruiterkamp, et al., 2008)

Figure 2.15 Higher order Multi plate kite models

MSC. ADAMS simulation program. The developed model is capable of simulating the structural deformations of a kite to a very high degree of accuracy; however, it is very time-consuming to construct and requires a lot of computing power.

2.7 Control Strategies

Most of the papers published early in the last two decades have addressed the issue of regulating the flight path of tethered wings using the Non-linear Model Predictive Control (NMPC) Strategy. The earliest attempts to control tethered wings using NMPC can be found in (Diehl et al., 2004). The control strategy is based on the model presented by Diehl in (Diehl et al., 2001) and focuses on trajectory control only without any reference to power generation

To regulate a tethered wing's flight cycle, which also accounts for energy generation (Canale et al., 2007) employed an NMPC control law. The flight path is controlled by manipulating the roll angle of the kite. Two controllers are developed simultaneously for the traction and retraction phases. The NMPC control law aims to harvest the maximum mechanical energy from the wind for power generation. The optimum

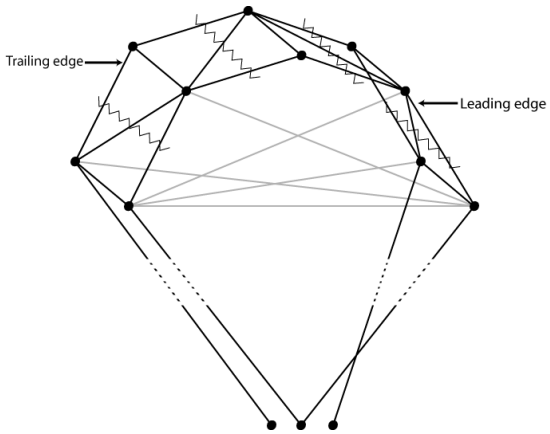

Figure 2.16 Lumped Parameter model (Furey & Harvey, 2007)

trajectory is shown to be periodic cycles of the lying figure of eights for the traction phase. (Canale et al., 2009) further investigated an NMPC strategy for different ground station configurations. (L. M. Fagiano, 2009) used a similar approach to investigate the relationship between system variables such as the tether length, kite area and aerodynamic efficiency, and the power production in the pumping cycle.

Using the NMPC method once more, (Williams, Lansdorp, Ruiterkamp, et al., 2008) investigated the utilization of power kites for two purposes: the pulling of ground vehicles using kite power and ground-based electric power generation. It was assumed that the tether reeling speed, roll angle and the kite's angle of attack were controlled under the NMPC law for power production.

The NMPC approaches mentioned above involve maximizing a tethered kite's average power output in pumping trajectory mode by simultaneously analyzing the flight steering and the ground winch control inputs. NMPC has certain benefits; however, solving it can be challenging due to its inherent complexity, need for accurate models and high computation costs. (Behrooz et al., 2018).

(Houska & Diehl, 2007) employed the optimal control strategy to control a pumping kite cycle. The tether reeling speed, roll angle, and coefficient of lift were the control inputs that had to be optimised to maximise the objective function, which was the cycle power. Again, lying-eights emerged as the most efficient trajectories. However, the drawback of optimum control is yet again its inherent complexity. The evaluation and execution of the optimum feedback control pose a formidable issue unless a

problem has a particular configuration (such as the linear, unconstrained models that yield the standard LQ regulator).

Over the Last, the tendency has changed from centralised control that solved for several control variables simultaneously, addressed by NMPC, to a decentralised method based on a single control variable to control the flight trajectory. Bearing in view that the winch subsystem at the ground and the airborne tethered kite subsystem are two separate components that interact to form the entire pumping kite system. The objective is to generate a pumping kite cycle with decentralised control, implying that only locally accessible control parameters are used in the control loops. The calculated control action is only executed for the subsystem under consideration. Such an approach is demonstrated by (Erhard & Strauch, 2012; L. Fagiano et al., 2013; Jehle & Schmehl, 2014) in both simulated and experimental flight conditions.

2.8 Developments in AWE Research and Markets

The framework for the thorough investigation and research in the field of AWE systems was established by Miles Lloyd in 1980. During 1980 and 2000, research on AWE remained stagnant, while the Danish three-bladed wind turbine established itself as the de facto standard in ground-based wind power generation technology. AWE development began to pick up the pace again towards the turn of the century through the developments in the tether and modern control technologies. The active institutions and major stakeholders participating in AWE research are illustrated in Fig.2.17 and 2.18 respectively

KiteGen Research is one of the first businesses to test a fixed ground-based power generation AWE system prototype. Their invention is based on a Leading edge inflatable C-Kite with onboard electrical sensors and is operated by two power ropes from a ground control station. In 2006, KiteGen Research successfully demonstrated its first prototype. The company is presently focusing on building a new 3 MW generator named the "KiteGen Stem". An ex-partner of KiteGen founded Kitenergy, an Italian business pursuing a similar idea by using two power ropes to operate a foil kite. The prototype has a 60 kW rating power.

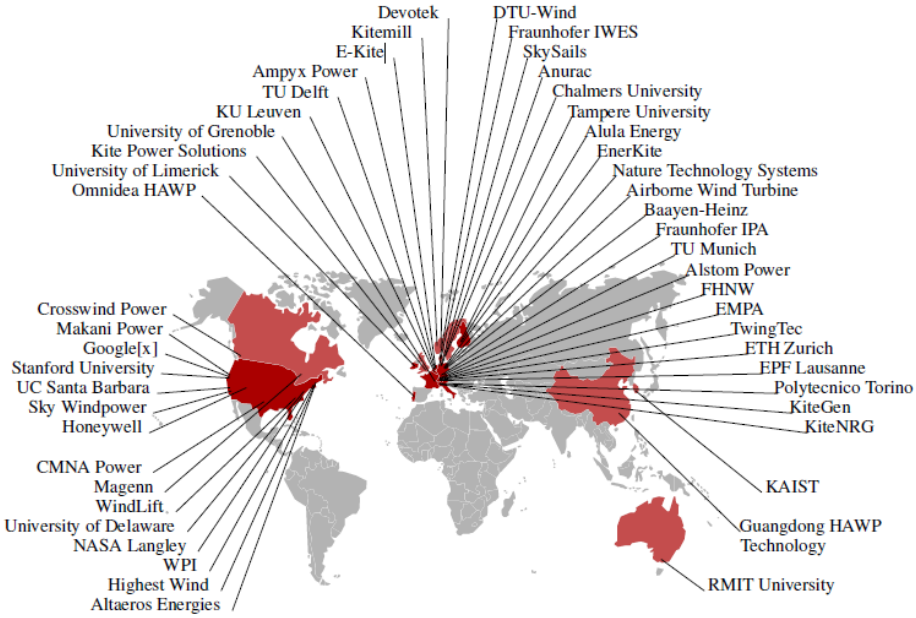

Figure 2.17 Research and development in AWE by country and team (Diehl, 2013)

The German business SkySails is working on a parasail-based wind propulsion system for cargo ships. Based on their ship propulsion technology, a new subsidiary of the firm called "SkySails Power" was established that focuses on Ground generation AWE systems. The AWE system uses a foil kite with a single tether and a control unit, which regulates the lengths of kite bridles to steer the kite and adjust its angle of attack. The control pod is powered and can communicate with the ground station via electrical lines embedded with the tether. A mobile AWE system with a capacity of 250 kW to 1 MW and an offshore system with a capacity of 1 to 3.5 MW are currently under development.

In 1996, Professor Ockels started his first study on AWE systems at the Technical University of Delft. Ockels established a special research team in 2004 to advance the technology to the prototype level. The research team has already tested a variety of wings, including foil kites and kite planes. TU Delft and the Karlsruhe University of Applied Sciences launched a project to create and test a portable 20 kW experimental kite generator. Currently, the TU Delft uses an LEI kite with a 25 m^2 surface area. In 2012, the wing demonstrated autonomous launch configuration and fully automatic operation of its 20 KW system. An automated launch and recovery system is being

Figure 2.18 Some major companies and institutions involved in AWE (Zillmann & Bechtle, 2018)

created for 100 m^2 LEI kites.

In ground-based power generation with rigid wings, A swiss company, TwingTec, has developed a 100-kW generation system. Similarly, Ampyx Power, a Dutch company, uses a rigid tethered wing connected to a generator on the ground. Ampyx Power is one of the few businesses that has developed an AWE system capable of performing autonomous takeoff, pumping cycles, and landing procedures. Their demonstrator system AP3 is designed to have a rated power of 150 kW and flight altitude of 200-450 m. Ampyx Power has begun developing its first commercial AWE design, a 35 m^2 AP-4 wing capable of producing a rated power of 2 MW, comparable to the power output of a large wind turbine. They also plan for an AP5 system with a 200-250 m^2 wing area and a 5 MW rated power output.

25 years since Loyd's work, Makani Power Inc. began creating its Airborne Wind Turbine (AWT) prototypes. Makani has tried several AWE concepts throughout the last few years, including ground-based generation with soft and rigid wings, single and multi-tether systems, and stationary and moving ground stations. The company created a brand-new concept for a bimodal flight to address issues with autonomous takeoff and landing. It utilizes a rigid wing with onboard generators for power production. The onboard generators work as rotors like a quadcopter for take-off and

landing phases. The flight mode shifts to pumping mode as the tether unwinds and the system reaches its operational altitude. The tether length remains fixed, and the aircraft flies in circular trajectories to produce drag power which is transferred to the ground station via electric lines embedded in the tether. Currently, Makani is developing the M600, a 600 kW prototype with eight onboard turbine generators and a 28 m wing span. Following the M600, Makani intends to create an offshore AWT with a nominal power of 5 MW, 6 turbines and a 65 m wingspan.

These activities suggest that the investment environment strives to develop novel wind energy technologies commercially. The market for AWE is expanding due to rising global electricity demand and investments in renewable energy projects. Additionally, the government and other national and international organisations are adopting several strategies, including providing financial support, to hasten the construction of such a project, which also has a significant impact on the market for AWE. In addition, this technology is quite affordable, which further stimulates the market for this technology. The demand for electricity is also sparked by industrial development and urbanisation in developing nations, favourably impacting this industry's expansion. Consequently, the factors mentioned above promote the development of AWE markets (IndustryARC, 2022).

CHAPTER 3

DYNAMIC MODELLING OF AN AIRBORNE WIND ENERGY SYSTEM

The first step in analyzing the physics of a system is to model its dynamic behaviour. Dynamic modelling helps to predict a physical system's motion under different constraints and operational scenarios. Such studies make it possible to evaluate a system's overall performance and feasibility before developing an experimental prototype. This approach saves a significant amount of investment in manufacturing costs and time.

Numerous models with varying degrees of accuracy have been presented in the literature to describe the behaviour of tethered wing AWE systems. The most complicated models can accurately represent an AWE system's aerodynamics behaviours and wing deformations, as discussed in Section 2.6.4. However, they have a very high computational cost. A better degree of detail is still offered by models with intermediate levels of complexity, allowing them to be utilised for quicker, real-time simulations. These models are easily employed and better suited for controller design and optimization tasks.

3.1 Model Description

The following contents of the chapter present the development of an AWE system model of intermediate complexity. The models previously discussed in the literature are re-evaluated to select the best-suited design parameters under the scope of this thesis. The main requirement of the model is to run in real-time for controller design. The model is based on a two-line kite model presented in (Diehl et al., 2001), where the kite is modelled as a point mass with the following assumptions. The first as-

sumption is that the orientation of the kite is coupled to the direction of the apparent wind and the kite automatically adjusts itself to the apparent wind speed. The second assumption is that the tether is mass-less and considered a rigid line; therefore, it does not have any associated drag. The third and final assumption is a constant angle of attack for the entire flight cycle. In contrast to the first and the final assumption, an improved point mass model is presented that accounts for a variable angle of attack. Since the angle of attack is a function of the kite body orientation and the apparent wind direction, the two parameters are not considered as coupled anymore in the model presented as follows.

3.2 Model Kinematics

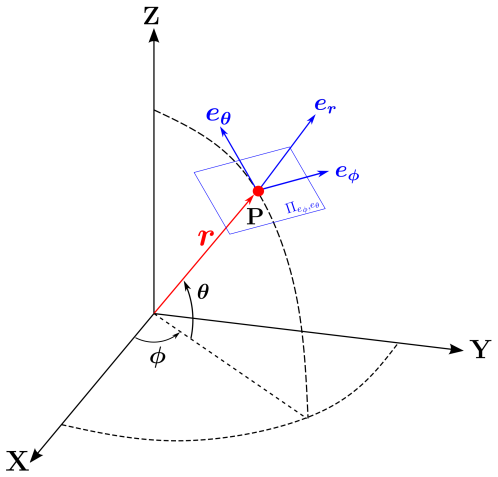

Figure 3.1 Point mass kite (P) in spherical coordinates

3.2.1 Coordinate Frames

The Inertial Frame: A Cartesian coordinate system $(\mathbf{X}, \mathbf{Y}, \mathbf{Z})$ is treated as an inertial frame with orthonormal basis $(\vec{e_x}, \vec{e_y}, \vec{e_z})$, whose origin fixed on the ground. The winch or the ground station is positioned at the origin and serves as the tether's point of attachment. The atmospheric wind speed vector $\vec{\mathbf{V}}_\mathbf{w}$ is aligned with the $\vec{e_x}$ direction and can be written as $\vec{\mathbf{V}}_{\mathbf{w}[\mathbf{I}]} = \begin{bmatrix} \mathbf{V_w} & 0 & 0 \end{bmatrix}'$. Vectors written in the inertial frame are denoted with the subscript $\mathbf{I}$.

The Local Frame: To model the three dimensional dynamics of a kite considered as a point mass, its position in the inertial frame is represented by the spherical coordinate system ($\boldsymbol{r}, \boldsymbol{\phi}, \boldsymbol{\theta}$), with the basis ($\vec{e_r}, \vec{e_\phi}, \vec{e_\theta}$), as shown in Fig.3.1 $\boldsymbol{r}$ is the radial length from the ground station to the kite. Since the tether is modelled as perfectly rigid, $\boldsymbol{r}$ also represents the tether length. The angle $\boldsymbol{\theta}$ is the elevation angle, and $\boldsymbol{\phi}$ corresponds to the azimuth angle. In the following derivation of the model dynamics, the spherical coordinate system is referred to as the Local frame and is denoted by the subscript **L**.

The Body Fixed Frame: A non-inertial frame is attached to the kite body, with orthonormal basis ($\vec{x_b}, \vec{y_b}, \vec{z_b}$). It is similar to the body frames attached to the fixed wing air crafts in flight dynamics literature (Beard & McLain, 2012; Etkin, 1959), with $\vec{x_b}$ points towards the leading edge of the kite in the longitudinal direction and $\vec{y_b}$ points in the transverse direction. according to an orthonormal basis, $\vec{z_b}$ is pointed downwards. It is useful in describing the kite orientation with respect to the local frame.

The Apparent Wind Frame: A non-inertial frame that aligns with the direction of the apparent wind. it is defined by the orthonormal basis ($\vec{x_a}, \vec{y_a}, \vec{z_a}$), where $\vec{x_a}$ is oriented towards the direction of the apparent wind. It is analogous to the wind frames defined in flight dynamics literature for fixed wing air crafts (Beard & McLain, 2012; Etkin, 1959) for a zero side slip angle. The apparent wind frame is used in modelling the direction of the aerodynamic force vectors. The body fixed frame and the apparent wind frame are illustrated in Fig.3.2

3.2.2 Kite position and transformation matrices

The position of the kite in the inertial coordinate system is given by

$$\vec{\mathbf{P}_{[\mathbf{I}]}} = \begin{bmatrix} X \\ Y \\ Z \end{bmatrix} = \boldsymbol{r} \begin{bmatrix} \cos\theta\cos\phi \\ \cos\theta\sin\phi \\ \sin\theta \end{bmatrix}. \tag{3.1}$$

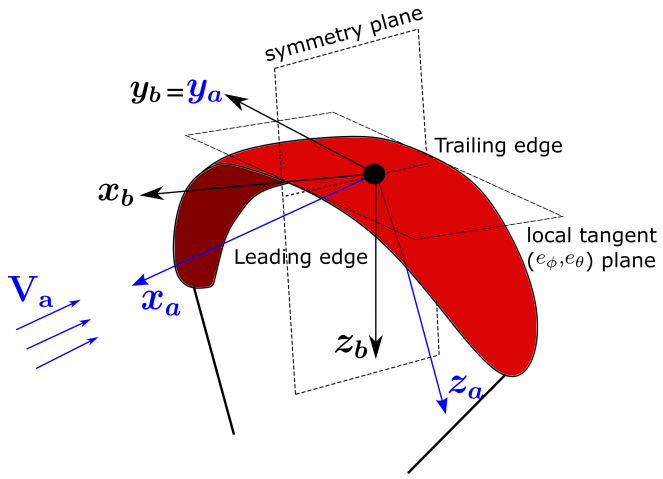

Figure 3.2 The Body fixed frame $(\vec{x_b}, \vec{y_b}, \vec{z_b})$ and apparent wind frame $(\vec{x_a}, \vec{y_a}, \vec{z_a})$. $\vec{x_a}, \vec{x_b}, \vec{z_a}$ and $\vec{z_b}$ lie on the symmetry plane of the kite. If no rotation around the longitudinal axis is assumed, $\vec{y_a} = \vec{y_b}$ lie on the local tangent plane

Point $\mathbf{P}$ also serves as the local frame's origin, which is written in the inertial frame by the orthonormal vectors

$$\begin{aligned}
\vec{e_r} &= \frac{\partial \mathbf{P}}{\partial r}\frac{1}{r} = \begin{bmatrix}\cos\theta\cos\phi & \cos\theta\sin\phi & \sin\theta\end{bmatrix}', \\
\vec{e_\phi} &= \frac{\partial \mathbf{P}}{\partial \phi}\frac{1}{r\cos\theta} = \begin{bmatrix}-\sin\phi & \cos\phi & 0\end{bmatrix}', \\
\vec{e_\theta} &= \frac{\partial \mathbf{P}}{\partial \theta}\frac{1}{r} = \begin{bmatrix}-\sin\theta\cos\phi & -\sin\theta\sin\phi & \cos\theta\end{bmatrix}'.
\end{aligned} \tag{3.2}$$

The rotation matrix from the local frame to the inertial frame is given by

$$\mathbf{R}_L^I = \begin{bmatrix}\vec{e_r} & \vec{e_\phi} & \vec{e_\theta}\end{bmatrix} = \begin{bmatrix}\cos\theta\cos\phi & -\sin\phi & -\sin\theta\cos\phi \\ \cos\theta\sin\phi & \cos\phi & -\sin\theta\sin\phi \\ \sin\theta & 0 & \cos\theta\end{bmatrix}. \tag{3.3}$$

Similarly, the rotation matrix from the inertial to the local frame can be written as inverse or transpose of $\mathbf{R}_L^I$

$$\mathbf{R}_I^L = (\mathbf{R}_L^I)^T = (\mathbf{R}_L^I)^{-1} = \begin{bmatrix}\cos\theta\cos\phi & \cos\theta\sin\phi & \sin\theta \\ -\sin\phi & \cos\phi & 0 \\ -\sin\theta\cos\phi & -\sin\theta\sin\phi & \cos\theta\end{bmatrix}. \tag{3.4}$$

3.2.3 Velocities and acceleration

The velocity of the kite in the local frame $(\vec{e_r}, \vec{e_\phi}, \vec{e_\theta})$ is given by

$$\vec{\mathbf{V}}_{\mathbf{k},[L]} = \frac{\mathrm{d}\vec{\mathbf{P}}}{\mathrm{d}t} = \frac{\partial \vec{\mathbf{P}}}{\partial r}\dot{r} + \frac{\partial \vec{\mathbf{P}}}{\partial \phi}\dot{\phi} + \frac{\partial \vec{\mathbf{P}}}{\partial \theta}\dot{\theta}\,. \tag{3.5}$$

Substituting the values of the partial derivatives from Eq.3.2, the velocity of the kite can be written as

$$\vec{\mathbf{V}}_{\mathbf{k},[L]} = \dot{r}\ \vec{\mathbf{e}}_{\mathbf{r}} + r\dot{\phi}\cos\theta\ \vec{\mathbf{e}}_{\phi} + r\dot{\theta}\ \vec{\mathbf{e}}_{\theta}\,,$$

$$\vec{\mathbf{V}}_{\mathbf{k},[L]} = \begin{bmatrix} \dot{r} \\ r\dot{\phi}\cos\theta \\ r\dot{\theta} \end{bmatrix}. \tag{3.6}$$

The apparent wind experienced by the kite is the vectorial combination of the true or atmospheric wind and the kite velocity. Lift and drag forces acting on the kite are calculated as a function of the apparent wind speed. The apparent wind velocity in the Local frame can be written as

$$\vec{\mathbf{V}}_{\mathbf{a},[L]} = \mathbf{R}_I^L\ \vec{\mathbf{V}}_{\mathbf{w}[I]} - \vec{\mathbf{V}}_{\mathbf{k},[L]}\,, \tag{3.7}$$

where $\vec{\mathbf{V}}_{\mathbf{w}[I]} = \begin{bmatrix} \mathbf{V_w} & 0 & 0 \end{bmatrix}'$ is wind vector in the written in the inertial coordinate system and $\mathbf{R}_I^L$ is the Rotation matrix from the inertial to the local coordinate system. All the vectors must be written in the same coordinate system.
Finally, the acceleration of the kite in the local coordinate system can be defined as

$$\vec{\mathbf{a}}_{\mathbf{k},[L]} = \ddot{\vec{\mathbf{P}}} = \frac{\mathrm{d}^2\vec{\mathbf{P}}}{\mathrm{d}t^2}\,,$$

$$\vec{\mathbf{a}}_{\mathbf{k},[L]} = \begin{bmatrix} \ddot{r} - r\dot{\theta}^2 - r\dot{\phi}^2\cos^2\theta \\ r\ddot{\phi}\cos\theta + 2\dot{r}\dot{\phi}\cos\theta - 2r\dot{\phi}\dot{\theta}\sin\theta \\ r\ddot{\theta} + 2\dot{r}\dot{\theta} + r\dot{\phi}^2\cos\theta\sin\theta \end{bmatrix}. \tag{3.8}$$

At this point, it is important to introduce the roll angle and angle of attack applied to the kite system. These concepts help to define the orientation of the apparent wind frame to model the aerodynamic forces in Sections 3.2.6 and 3.3 respectively.

3.2.4 Roll angle

The concept of roll angle applied to the kite system is similar to the one defined in flight mechanics literature for a fixed-wing aircraft. The roll angle is the angle through which a fixed wing is rotated about its longitudinal axis by the action aileron input. Consider a two-line kite shown in Fig.3.3 as a rigid body with two cables connected to its left and right wingtips. The steering cables mimic the action of ailerons. It is possible to roll the wing by an angle ψ by a net change in length Δl of the left l_L and right l_R steering cables.

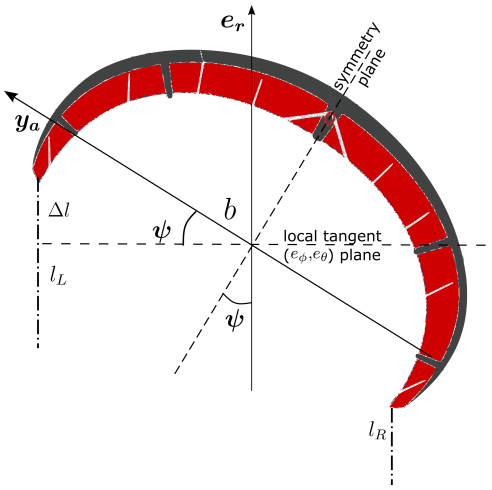

Figure 3.3 Illustration of roll angle from a kite's leading edge

$$\begin{aligned} \Delta l &= l_L - l_R = b \sin \psi \,, \\ \psi &= \arcsin \frac{\Delta l}{b} \,, \end{aligned} \tag{3.9}$$

where Δl represents the change in length of the steering cables and b is the kite's wing span. ψ shows the rotation of the kite's transversal axis about the local tangent (e_ϕ, e_θ) plan.

3.2.5 Angle of attack

The angle of attack is defined as the angle between the longitudinal body axis and the apparent wind speed vector. The notion of a partial angle of attack $\Delta\alpha$ is used here,

which is the angle between the tangent plane and the apparent wind velocity.

$$\Delta\alpha = \arcsin\left(\frac{\vec{\mathbf{V}}_\mathbf{a} \cdot \vec{\mathbf{e}}_\mathbf{r}}{\vec{\mathbf{V}}_\mathbf{a}}\right). \tag{3.10}$$

The total angle of attack α for the kite, as illustrated in Fig.3.4, can be written as

$$\alpha = \alpha_0 + \Delta\alpha\ . \tag{3.11}$$

$\Delta\alpha$ depends on the apparent wind speed, which in turn is dependent on kite dynamics. The quantity α_0 is an important modelling parameter. Its function is similar to the pitch angle in fixed wing aircraft literature (Beard & McLain, 2012; Etkin, 1959). The notion of pitch angle used in the thesis describes it with respect to the local tangent plane, as opposed to the longitudinal axis of the inertial frame in common literature. In some airborne wind energy literature, it is also referred to as the base angle of attack (L. M. Fagiano, 2009). α_0 can be chosen as a constant value or changed as a steering input to control the total angle of attack. For $\alpha_0 = 0$, the cross-section of the kite is aligned with the local tangent plane (e_ϕ, e_θ). Increasing or decreasing the base angle of attack directly influences the traction force.

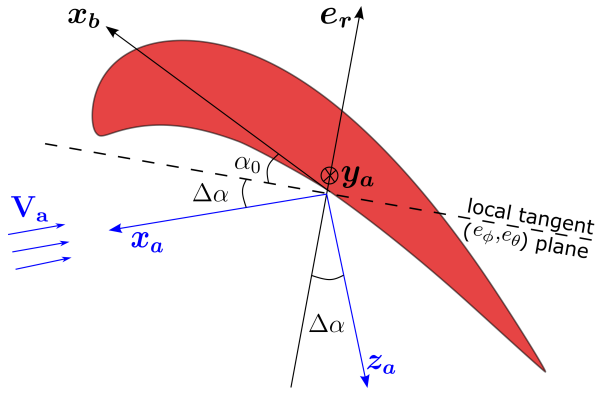

Figure 3.4 Cross section of the kite symmetry plane showing the pitch angle α_0, partial angle of attack $\Delta\alpha$, and the total angle of attack α

3.2.6 Kite orientation

To model the aerodynamic forces acting on the kite, it is first necessary to define the basis for the apparent wind coordinate system. Since the longitudinal axis of the

apparent wind frame always aligns with the apparent wind direction, it can be defined as

$$\vec{\boldsymbol{x_a}} = -\frac{\vec{\mathbf{V_a}}}{\|\vec{\mathbf{V}}_\mathbf{a}\|} \,. \tag{3.12}$$

The drag force acting on the system can now be modelled in the $-\vec{\boldsymbol{x_a}}$ direction and the lift force in the $\vec{\boldsymbol{z_a}}$ direction. To find $\vec{\boldsymbol{y_a}}$, a null rotation around the $\vec{\boldsymbol{x_a}}$ axis (i.e ψ = 0) is considered. A new intermediate axis $\tilde{\mathbf{y_a}}$ is introduced in the local tangent plane (e_ϕ, e_θ) for ψ = 0, such that initially $\tilde{\mathbf{y_a}} = \vec{\boldsymbol{y_a}}$, $\tilde{\mathbf{y_a}} \perp \vec{\boldsymbol{e_r}}$ and $\tilde{\mathbf{y_a}} \perp \vec{\boldsymbol{x_a}}$. The intermediate axis $\tilde{\mathbf{y_a}}$ is therefore defined as

$$\tilde{\mathbf{y_a}} = \frac{\vec{\boldsymbol{e_r}} \times \vec{\boldsymbol{x_a}}}{\|\vec{\boldsymbol{e_r}} \times \vec{\boldsymbol{x_a}}\|} \,. \tag{3.13}$$

Finally, an anti-clockwise rotation ψ is considered along the longitudinal axis. Using the Rodriguez formula, it is now possible to rotate the vector $\tilde{\mathbf{y_a}}$ by an amount of ψ around $\vec{\boldsymbol{x_a}}$. $\vec{\boldsymbol{y_a}}$ can now be defined as

$$\vec{\boldsymbol{y_a}} = \tilde{\mathbf{y_a}} \cos\psi + (\vec{\boldsymbol{x_a}} \times \tilde{\mathbf{y_a}}) \sin\psi + \vec{\boldsymbol{x_a}}(\vec{\mathbf{x_a}} \cdot \tilde{\mathbf{y_a}})(1 - \cos\psi) \,. \tag{3.14}$$

Since the basis for the apparent wind coordinate system form an orthonormal system of vectors, $\vec{\boldsymbol{z_a}}$can be defined as

$$\vec{\boldsymbol{z_a}} = \vec{\boldsymbol{x_a}} \times \vec{\boldsymbol{y_a}} \,. \tag{3.15}$$

3.3 Model Dynamics

The equations of motion for the kite are set up using classical mechanics. From Newton's 2nd law of motion

$$\begin{aligned} \sum \vec{\mathbf{F}}_k &= m\, \vec{\mathbf{a_k}} \,, \\ m\, \vec{\mathbf{a_k}}_{[L]} &= \left(\vec{\mathbf{F}}^T + \vec{\mathbf{F}}^g + \vec{\mathbf{F}}^{aero}(\alpha, \psi)\right)_{[L]} \,, \end{aligned} \tag{3.16}$$

where m is the kite mass, $\vec{\mathbf{F}}^T$ is the tether Tension, $\vec{\mathbf{F}}^g$ is the gravitational force, and $\vec{\mathbf{F}}^{aero}$ is the aerodynamic force written as a sum of lift and drag forces acting on the kite. The forces acting on the kite are illustrated in Fig.3.5. It is important to note that all the forces are resolved in the local coordinate system and are calculated as follows.

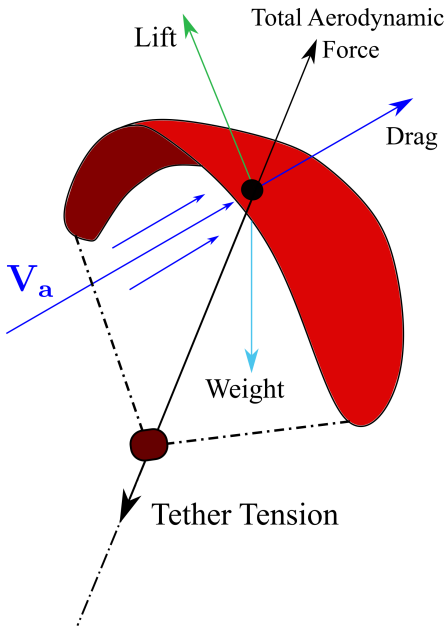

Figure 3.5 Force Balance on the kite

3.3.1 Tether tension

It is the pulling force which unwinds the tether from the winch and acts in the $-\vec{e_r}$ direction. The tether tension is calculated as

$$\vec{\mathbf{F}}^T = \begin{bmatrix} \mathbf{F}_{\boldsymbol{r}}^T \\ \mathbf{F}_{\boldsymbol{\phi}}^T \\ \mathbf{F}_{\boldsymbol{\theta}}^T \end{bmatrix} = \begin{bmatrix} -T \\ 0 \\ 0 \end{bmatrix}_L . \tag{3.17}$$

3.3.2 Gravitational force

Since the tether is assumed to have no mass, the overall force of gravity acting on the kite is due to the weight of the kite only. The vector of the gravitation force in the inertial coordinate system is directed towards the $-$Z axis. The gravitation force in the local frame is written as

$$\vec{\mathbf{F}}^g = \begin{bmatrix} \mathbf{F}_{\boldsymbol{r}}^g \\ \mathbf{F}_{\boldsymbol{\phi}}^g \\ \mathbf{F}_{\boldsymbol{\theta}}^g \end{bmatrix} = \mathbf{R}_I^L \begin{bmatrix} 0 \\ 0 \\ -m\,g \end{bmatrix}_I = \begin{bmatrix} -m\,g\sin\theta \\ 0 \\ -m\,g\cos\theta \end{bmatrix}_L . \tag{3.18}$$

3.3.3 Aerodynamic forces

The total aerodynamic force acting on the kite consists of the lift and the drag forces, which are calculated as

$$\begin{aligned} \vec{\mathbf{F}}^{Lift}(\alpha,\psi) &= \frac{1}{2}\,\rho\,A\,C_L(\alpha)\,\|\mathbf{V_a}\|^2\,\vec{\boldsymbol{z_a}}(\psi), \\ \begin{bmatrix} \mathbf{F}_{\boldsymbol{r}}^{Lift} \\ \mathbf{F}_{\boldsymbol{\phi}}^{Lift} \\ \mathbf{F}_{\boldsymbol{\theta}}^{Lift} \end{bmatrix}(\alpha,\psi) &= \frac{1}{2}\,\rho\,A\,C_L(\alpha)\,\|\mathbf{V_a}\|^2 \begin{bmatrix} \boldsymbol{z_{a,r}} \\ \boldsymbol{z_{a,\phi}} \\ \boldsymbol{x_{a,\theta}} \end{bmatrix}, \end{aligned} \tag{3.19}$$

$$\begin{aligned} \vec{\mathbf{F}}^{Drag}(\alpha,\psi) &= \frac{1}{2}\,\rho\,A\,C_D(\alpha)\,\|\mathbf{V_a}\|^2\,\vec{\boldsymbol{x_a}}(\psi), \\ \begin{bmatrix} \mathbf{F}_{\boldsymbol{r}}^{Drag} \\ \mathbf{F}_{\boldsymbol{\phi}}^{Drag} \\ \mathbf{F}_{\boldsymbol{\theta}}^{Drag} \end{bmatrix}(\alpha,\psi) &= \frac{1}{2}\,\rho\,A\,C_D(\alpha)\,\|\mathbf{V_a}\|^2 \begin{bmatrix} \boldsymbol{x_{a,r}} \\ \boldsymbol{x_{a,\phi}} \\ \boldsymbol{x_{a,\theta}} \end{bmatrix}, \end{aligned} \tag{3.20}$$

where ρ is the air density, A is the kite's surface area, $C_L(\alpha)$ and $C_D(\alpha)$ are the lift and drag coefficients calculated as a function of the angle of attack of the kite. The net aerodynamic force can now be written as

$$\vec{\mathbf{F}}^{aero}(\alpha,\psi) = \vec{\mathbf{F}}^{Lift}(\alpha,\psi) + \vec{\mathbf{F}}^{Drag}(\alpha,\psi). \tag{3.21}$$

3.3.4 Lift and drag coefficients

The lift and drag coefficients of the kite are required to accurately model the aerodynamic forces acting on the kite. The design procedure involves specifying the wing geometry for airfoils to determine the lift and drag coefficient values to ensure that the system performs as intended for the specified wingspan. According to the thin airfoil theory for 2-D infinite wings, the lift distribution acts linearly for a certain range of angles of attack (Anderson, 2001) and can be written as

$$C_l(\alpha) = a_0(\alpha - \alpha_{L=0})\,. \tag{3.22}$$

where a_0 is the slope of the lift curve plotted against the angle of attack, α is the angle of attack and $\alpha_{L=0}$ is the angle of attack for zero lift. According to the thin airfoil theory, the lift slope is always equal to 2π for any airfoil shape. The slope of the lift curve is also expressed in other aerodynamics literature as $C_{L\alpha}$.

The thin airfoil implies that the wing extends indefinitely, i.e. there are no wingtips on the lifting surface (Anderson, 2005). Furthermore, the thin airfoil theory assumes that the lift slope increases indefinitely at a constant rate as the angle of attack increases. However, in reality, the lift coefficient reaches a maximum value and decreases as the angle of attack increases further. Also, a type of drag called the "induced drag" is introduced by the wingtips. The slope of the lift curve is decreased as the induced drag increases. The theory can further be extended to 3-D finite wing forms to account for the induced drag at the wingtips (Anderson, 2001).

Despite its limitations, it is considered appropriate to calculate the lift coefficient using the thin airfoil theory. Otherwise, calculating the lift coefficient would require an experimental aerodynamic analysis of the kite. A similar aerodynamic analysis of an arc-shaped kite presented in (Oehler & Schmehl, 2018) shows the lift coefficient of a kite in the traction phase could reach as high as 1.6. The thin airfoil theory provides a good approximation to calculate the lift coefficient for an acceptable range of angle of attack.

For the drag coefficient, only the profile drag is considered and taken as a constant.

3.3.5 Apparent forces

Newton's 2nd law of motion is only valid when the acceleration is specified with respect to an inertial frame of reference. To reconcile Newton's law with non-inertial frames of reference, apparent forces must be introduced. For objects in motion around a circle or a sphere, if the acceleration in a non-inertial frame of reference is specified as a*, then

$$a = a^* + a_{app} \, . \tag{3.23}$$

Newton's 2nd law can now be written as

$$F - ma_{app} = ma^* \, . \tag{3.24}$$

The quantity $-ma_{app}$ is the inertial or apparent force, and a_{app} is referred to as the inertial or apparent acceleration. The apparent acceleration experienced by the kite can be obtained by deriving the position twice in the local frame; hence Eq.(3.8) can

be re-written as

$$\ddot{\vec{\mathbf{P}}} = \begin{bmatrix} \ddot{r} \\ r\ddot{\phi}\cos\theta \\ r\ddot{\theta} \end{bmatrix} + \underbrace{\begin{bmatrix} -r\dot{\theta}^2 - r\dot{\phi}^2\cos^2\theta \\ +2\dot{r}\dot{\phi}\cos\theta - 2r\dot{\phi}\dot{\theta}\sin\theta \\ +2\dot{r}\dot{\theta} + r\dot{\phi}^2\cos\theta\sin\theta \end{bmatrix}}_{-\frac{1}{m}\vec{\mathbf{F}}^{app}}. \tag{3.25}$$

Note that the the first vector in Eq.(3.25) corresponds to a^* and the second vector corresponds to a_{app} in Eq.(3.23) respectively. The apparent forces experienced by the kite are a sum of centrifugal and Coriolis forces and can be written as

$$\begin{aligned} \vec{\mathbf{F}}^{app} = \begin{bmatrix} \mathbf{F}_{\boldsymbol{r}}^{app} \\ \mathbf{F}_{\boldsymbol{\phi}}^{app} \\ \mathbf{F}_{\boldsymbol{\theta}}^{app} \end{bmatrix} &= m \begin{bmatrix} r\dot{\theta}^2 + r\dot{\phi}^2\cos^2\theta \\ -2\dot{r}\dot{\phi}\cos\theta + 2r\dot{\phi}\dot{\theta}\sin\theta \\ -2\dot{r}\dot{\theta} - r\dot{\phi}^2\cos\theta\sin\theta \end{bmatrix}, \\ &= \underbrace{m \begin{bmatrix} r\dot{\theta}^2 + r\dot{\phi}^2\cos^2\theta \\ 0 \\ -r\dot{\phi}^2\cos\theta\sin\theta \end{bmatrix}}_{Centrifugal force} + \underbrace{m \begin{bmatrix} 0 \\ -2\dot{r}\dot{\phi}\cos\theta + 2r\dot{\phi}\dot{\theta}\sin\theta \\ -2\dot{r}\dot{\theta} \end{bmatrix}}_{Coriolis Force}. \end{aligned} \tag{3.26}$$

3.3.6 Equations of motion

Newton's 2nd law of motion can now be written as

$$m \begin{bmatrix} \ddot{r} \\ r\ddot{\phi}\cos\theta \\ r\ddot{\theta} \end{bmatrix} = \vec{\mathbf{F}}^T + \vec{\mathbf{F}}^g + \vec{\mathbf{F}}^{aero}(\alpha, \psi) + \vec{\mathbf{F}}^{app}. \tag{3.27}$$

Resulting in the three equations of motion for the system, presented below

$$\ddot{r} = \frac{1}{m}\left(\mathbf{F}_{\boldsymbol{r}}^T + \mathbf{F}_{\boldsymbol{r}}^g + \mathbf{F}_{\boldsymbol{r}}^{aero} + \mathbf{F}_{\boldsymbol{r}}^{app}\right). \tag{3.28}$$

$$\ddot{\phi} = \frac{1}{mr\cos\theta}\left(\mathbf{F}_{\boldsymbol{\phi}}^T + \mathbf{F}_{\boldsymbol{\phi}}^g + \mathbf{F}_{\boldsymbol{\phi}}^{aero} + \mathbf{F}_{\boldsymbol{\phi}}^{app}\right). \tag{3.29}$$

$$\ddot{\theta} = \frac{1}{mr}\left(\mathbf{F}_{\boldsymbol{\theta}}^T + \mathbf{F}_{\boldsymbol{\theta}}^g + \mathbf{F}_{\boldsymbol{\theta}}^{aero} + \mathbf{F}_{\boldsymbol{\theta}}^{app}\right). \tag{3.30}$$

3.3.7 Traction force and power generation

Assuming that $\ddot{r}$ can be controlled directly, the tether tension T can be computed directly from Eq.(3.28)

$$\begin{aligned} \mathbf{F}_{\boldsymbol{r}}^{T} = -T = m\ddot{r} - \mathbf{F}_{\boldsymbol{r}}^{g} - \mathbf{F}_{\boldsymbol{r}}^{aero} - \mathbf{F}_{\boldsymbol{r}}^{app}, \\ T = -m\ddot{r} + \mathbf{F}_{\boldsymbol{r}}^{g} + \mathbf{F}_{\boldsymbol{r}}^{aero} + \mathbf{F}_{\boldsymbol{r}}^{app}. \end{aligned} \tag{3.31}$$

The power generated by the kite at the ground station can then be calculated as

$$\begin{aligned} P &= T\, \vec{\mathbf{V}}_{\mathbf{k}r}\ , \\ &= T\, \dot{r}\ . \end{aligned} \tag{3.32}$$

3.4 Control Inputs

Most models discussed in the literature consider a four-tethered concept to represent the actuator steering inputs for the system, as shown in Fig.3.6. The primary tether is wound around the winch at the ground station and separates into two tethers at a junction as it approaches the kite. The two tethers are further coupled to the leading edge of the kite. Most of the traction force generated at the wing is transferred through the primary tether to the ground station for power generation. A control pod is secured in place at the junction. Two steering tethers originate from the pod and are connected at the tips of the trailing edge of the kite. Actuators in the control pod adjust the steering tether length by tugging on one and relaxing the other. The kite is hence steered in the desired heading by the action of the actuators.

The same concept could be applied to the two tether concepts presented in this model. In the literature reviewed, it is mostly that both the tethers originate and are steered from the ground (Sánchez-Arriaga et al., 2017). The objective is to emphasise the steering input—the change length of the steering tethers—that produces a corresponding change in the heading trajectory. The desired result can also be achieved using the concept presented in Fig.3.6. The model assumes a rigid kite structure instead of flexible behaviour. The assumption is deemed viable since the internal mechanisms that modify the flight trajectory may take several forms. In essence, the same steering input causes a flexible kite to bend and yaw and a rigid wing to roll.

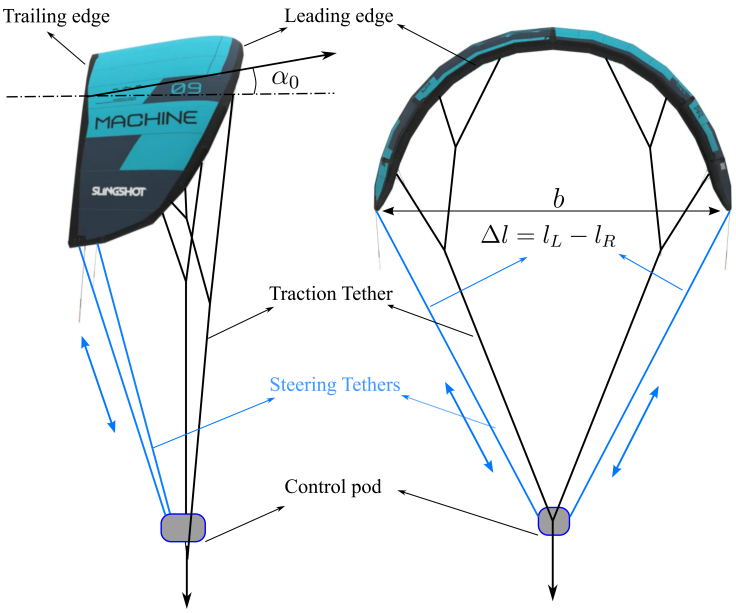

Figure 3.6 Four tether kite concept. The steering tethers are shown in blue, and the traction tether is shown in black

3.4.1 Roll angle

In consideration of the discussion above, the model presented in the thesis acts on the roll angle to steer the kite in the desired heading direction. The physics of the roll angle ψ is presented in Section 3.2.4. It is assumed that generating a differential in length Δl of the two tethers allows for direct control of the roll angle. The steering input for the roll angle is then defined as $\delta_\psi = \Delta l$. A positive steering input induces a positive roll which turns the kite in the right direction and vice versa. The roll angle defined in the model is only valid in the $(-\frac{\pi}{2}, \frac{\pi}{2})$ interval. The roll angle directly affects the lift force acting on the system, as shown in equations 3.14, 3.15 and 3.19

3.4.2 Pitch angle

The pitch angle or the base angle of attack α_0 introduced in Section 3.2.5 is set as a control variable to alter the magnitude of the lift force acting on the kite. Taking Fig.3.6 into consideration again, by shortening the steering length of both the tethers by the same amount, the pitch angle is increased, which also increases the angle of attack. The effect of the pitch angle and consequently the angle of attack on the

system dynamics can be inferred from the equations 3.19 and 3.22. A higher angle of attack corresponds to a greater lift force acting on the kite. A greater lift force, in turn, equals a higher traction force, which means more power is generated at the ground station. The pitch angle is assumed to be controlled directly and can be chosen as a constant value or varied at will during the operational cycle. It is generally desired to have a higher angle of attack during the traction phase. Whereas the angle of attack is decreased during the retraction phase to consume less power at the ground station.

3.4.3 Reel-out velocity

From Eq.(3.28) it is assumed that the tether acceleration can be controlled directly by controlling the reel in and reel out velocities of the tether. The literature concluded that the maximum power is produced when the kite unrolls at approximately one-third of the wind velocity (Loyd, 1980).

$$\mathbf{V}_{reel-out} \approx \frac{1}{3}\mathbf{V}_{\mathbf{w}}. \tag{3.33}$$

As a result, since the goal of the production phase is to maximize power output, we want to manage the tether acceleration to achieve the necessary reel-out speed. Similarly, finding a balance between time and energy is necessary throughout the recovery phase. While a faster reel-in speed reduces the time between the production cycles, it also consumes more energy and puts the kite at risk of losing control. Conversely, even though the energy consumption is low and the kite is aerodynamically more stable for a slower reel-in speed, the system's overall efficiency is significantly decreased. Therefore, when working out the reel-in velocity, it is essential to strike a balance between time and energy consumption.

CHAPTER 4

MODEL VALIDATION THROUGH OPEN-LOOP SIMULATIONS

This chapter presents the open-loop simulations of the dynamic model introduced in Chapter 3. The dynamic system is modelled and simulated in Matlab/Simulink©. This chapter aims to verify the model's dynamic behaviour by analysing its response to different control inputs. The model's response is first analysed for each control input to understand the dynamic behaviour. A coupled simulation, including all the control inputs, is presented at the end of the chapter to analyse the power generation potential. The physical parameters of the kite used in the simulation are taken from the F-one surf kite and presented in Table 4.1

Table 4.1 Kite specifications for open-loop simulations

Area (A)	12 m^2
Mass (m)	3.34 kg
Wing span (b)	3.5 m

4.1 Model Behaviour For Different Wind Speeds

The kite is simulated under different wind speeds to analyse the model's behaviour for varying wind conditions. All the control inputs are set as zero, i.e. no roll and pitch control inputs are applied, and the tether length is kept constant. It is evident from Eq.(3.19) that increasing the magnitude of the wind velocity increase the lift force acting on the kite. A greater lift causes an increase in the elevation angle $\boldsymbol{\theta}$. The effect of different wind speeds on the elevation angle is shown in Fig.4.1. For very

low wind speeds, the lift force is not sufficient to raise the kite and $\vec{\mathbf{F}}^{g} > \vec{\mathbf{F}}^{lift}$, the kite, therefore, falls to the ground. Since the kite has a minimal mass, even low wind speeds are adequate to lift the system to its equilibrium elevation. As the wind speed increases, the equilibrium elevation increases accordingly. For higher wind velocities, the equilibrium elevation is observed around $85°$.

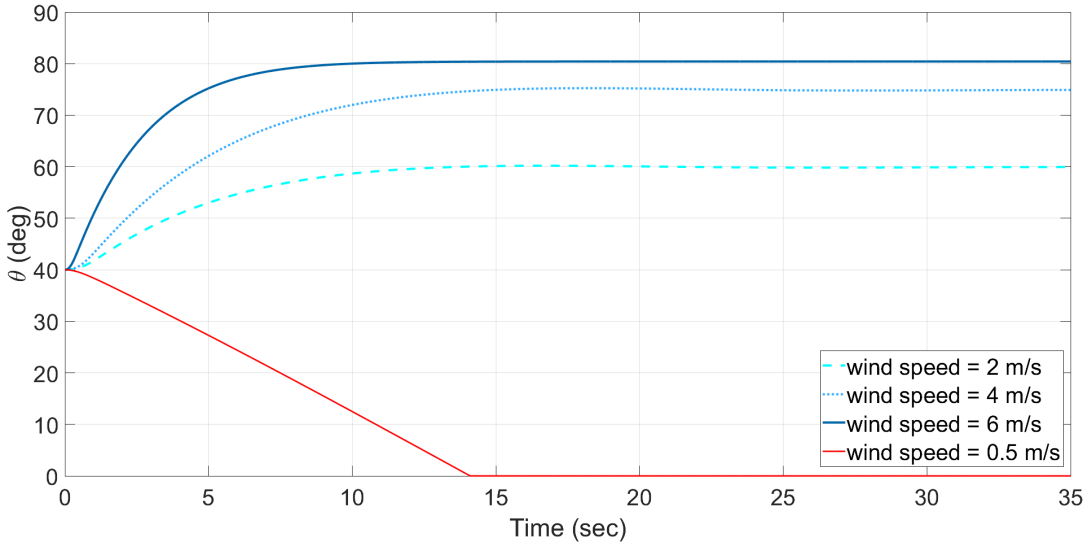

Figure 4.1 Effect of different wind speeds on the elevation angle $\boldsymbol{\theta}$ for zero roll and pitch inputs

4.2 Effect Of Roll Angle (ψ) Input On Kite Dynamics

As discussed in Section 3.4.1, by creating a difference in the length of the steering tethers Δl, the kite can be steered in the desired direction, and a change in its azimuth position, i.e the state variable $\boldsymbol{\phi}$ is anticipated. The roll behaviour of the kite is simulated and verified as seen in Fig.4.2. A symmetrical pulse input of 0.5 m and -0.5 m is applied for 10 seconds each. A symmetrical change in the azimuth position ($\boldsymbol{\phi}$) is observed as the kite executes a turning maneuver for the corresponding change in the roll angle (ψ). In the simulation model, the input to the roll angle is filtered through a low pass filter to remove the higher frequency parts of the signal. The simulation is performed for a constant wind speed of 5 $\mathrm{m/s}$. The tether length is kept constant, and no pitch input is applied.

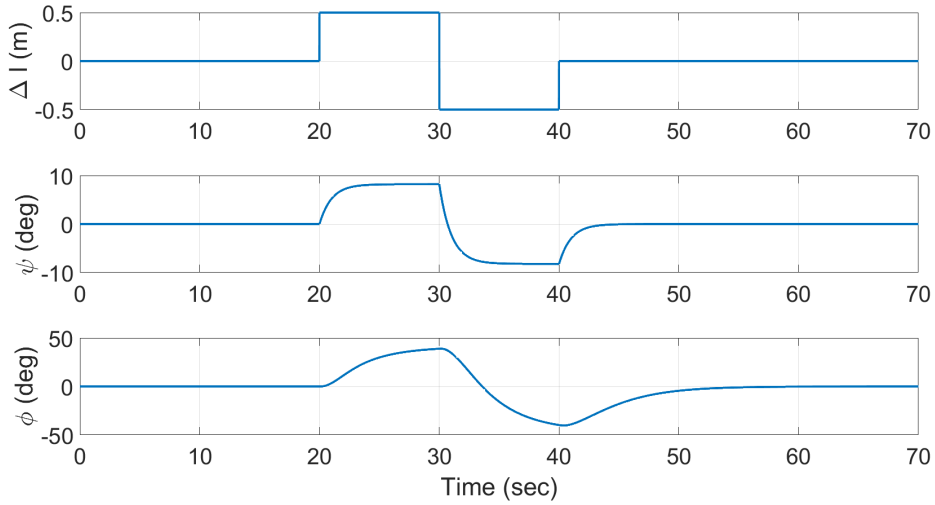

Figure 4.2 Variation in ϕ relative to the change in roll angle (ψ) as a function of the control input Δl

4.3 Effect Of Pitch Angle (α_0) Input On Kite Dynamics

The pitch angle input and, consequently, the angle of attack directly affect the model dynamics by changing the magnitude of the lift force and, subsequently, the tether tension as apparent from Eqs. (3.21) and (3.31). The effect of the pitch angle on the tether tension is reflected in Fig.4.3. The pitch angle is kept at zero in the beginning until the system reaches its equilibrium state. At t = 20 seconds, a constant pitch input of 5° is applied for 10 seconds, which increases the angle of attack from 11° to 16°. A significant increase in the tether tension from 1 kN to 1.5 kN is noted during this time interval. The opposite effect is seen as the pitch angle is lowered to -5°.

The effect of the pitch angle on model dynamics is utilized during the power production cycle. It is increased to increase the angle of attack during the production phase to have more tether tension for power generation at the ground station. During the retraction phase, it is desirable to consume minimum power hence the angle of attack is decreased to reduce the magnitude of the aerodynamic forces acting on the kite. As a result, the tension is reduced, and the kite is reeled in with less power.

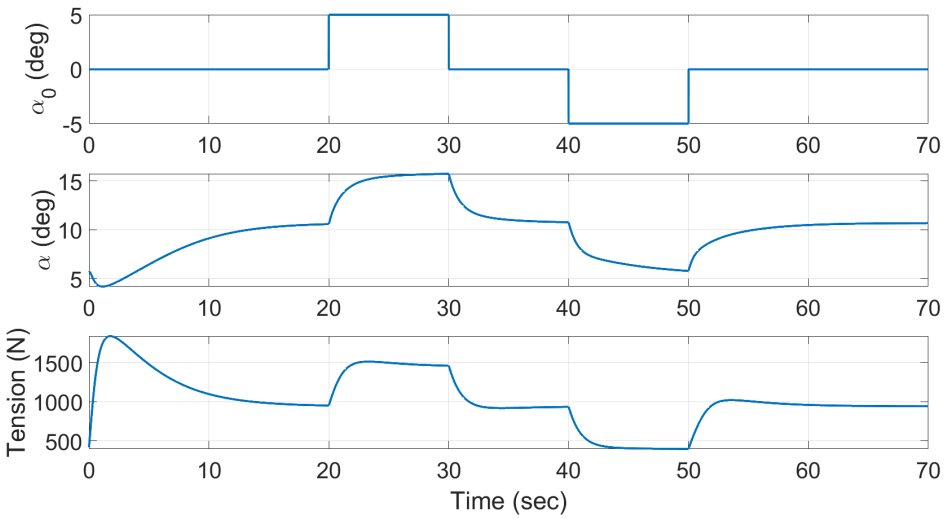

Figure 4.3 Change in Tether tension due to the change in angle of attack (α) as a function of the pitch control input (α_0)

4.4 Effect Of Reel Velocity Input On Kite Dynamics

The kite must reel out at a certain velocity to produce power at the ground station. For constant tether lengths, no power is produced. The system is simulated for a constant wind of 5 $\mathrm{m/s}$. The reel velocity is defined as 1 $\mathrm{m/s}$ for the reel out phase (20 - 50 seconds) and -1 $\mathrm{m/s}$ for the reel in phase (50 - 80 seconds). The rest of the control inputs are set as zero. The effect of the reel velocity is seen in Fig.4.4. Contrary to the desired result, there is a slight decrease in the tension during the reel-out phase, followed by an increase during the reel-in phase. The behaviour is, however, expected for low wind speeds and high tether velocities as a consequence of Eq.(3.31). The aerodynamic force due to the tether acceleration (-$m\ddot{r}$) appears with a negative sign in the equation. Therefore, the tension decreases by a factor of $m\ddot{r}$ during the reel-out phase when $\ddot{r}$ is positive and increases during the reel-in phase for negative values of $\ddot{r}$.

It is possible to attenuate the above-mentioned effect of the reel velocity by varying the angle of attack. Keeping all the simulation variables constant, the angle of attack increases during the reel-out phase and decreases during the reel-in phase by acting on the pitch angle input. The tether tension for this case is significantly increased

during the reel-out phase and decreased during the reel-in phase, as would be desired for a production cycle.

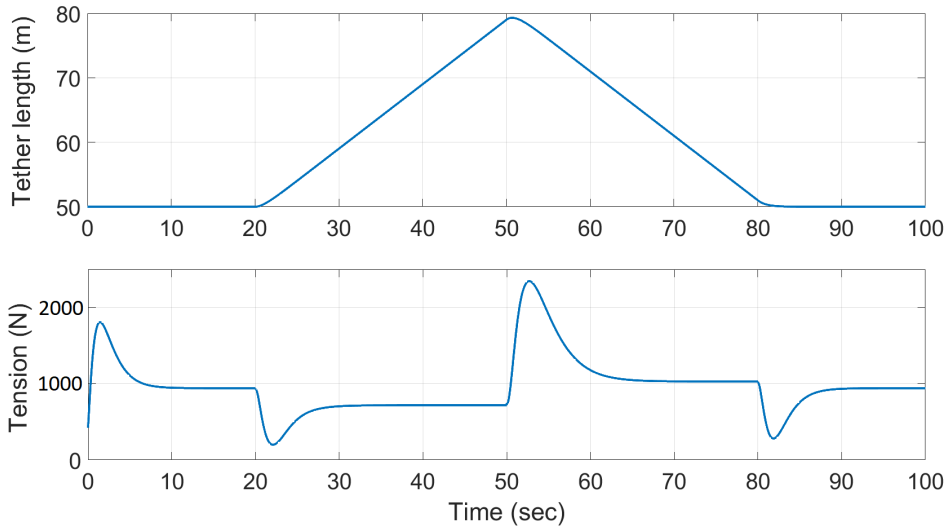

Figure 4.4 Effect of reel velocity on tether tension. Reel-out velocity is set as 1 $\mathrm{m/s}$, and reel-in velocity is set as -1 $\mathrm{m/s}$

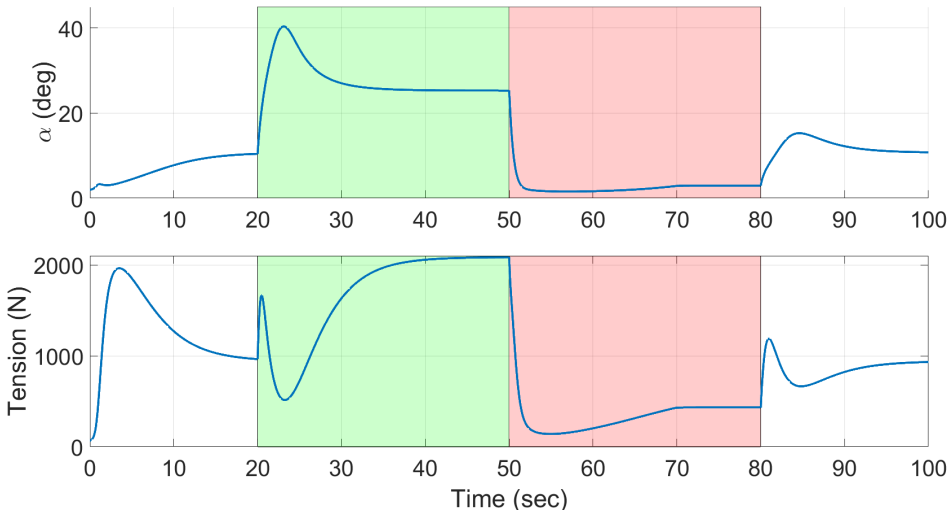

Figure 4.5 Effect of varying angle of attack on tether tension during the reel out phase (green) and the reel in phase (red)

4.5 Open Loop Power Generation

The coupled effect of the control inputs is simulated in this section to get a decent estimate of the power production potential of a kite for one production cycle. The dimensions are kept the same as used in the previous simulation in this chapter, given in Table 4.1. The open loop simulations for power production are further divided into two sub-sections. The first sub-section analyzes the power generation of a single production cycle without any reference to kite trajectory. A random trajectory is produced in the simulations presented in the second sub-section. The importance of an optimal trajectory for power production has been extensively discussed in AWE systems literature. A secondary objective of this section is to analyse the effect of the movement of the kite along a trajectory for power generation.

4.5.1 Power generation without roll induced trajectory

The system is simulated without acting on the roll angle, so no turning maneuvers are executed. The simulation parameters are given in Table 4.2

Table 4.2 Simulation parameters for an open loop power production cycle

Initial Conditions		Control Variables	
Wind speed ($\mathbf{V_w}$)	7.5 $\mathrm{m/s}$	Reel out velocity ($\dot{r}_{out}$)	2.5 $\mathrm{m/s}$
Elevation angle ($\boldsymbol{\theta}$)	50°	Reel in velocity ($\dot{r}_{in}$)	-2 $\mathrm{m/s}$
Azimuth angle ($\boldsymbol{\phi}$)	0°	Pitch angle (α_0) traction	25°
Initial tether length	100 m	Pitch angle (α_0) retraction	0°
Minimum tether length (r_{min})	100 m	Roll angle input (Δl) traction	0
Maximum tether length (r_{max})	350 m	Roll angle input (Δl) retraction	0

Fig.4.6 shows a 3-D illustration for a single production cycle. The kite reels out in a straight line along the X-axis as angle $\boldsymbol{\phi}$ is kept zero for the whole cycle. When the tether reaches its maximum length, it is reeled back in until it reaches its minimum length. During the reel-in phase, the kite elevates itself to its equilibrium elevation at 85°. The angle of attack increases during the reel-out phase and decreases during

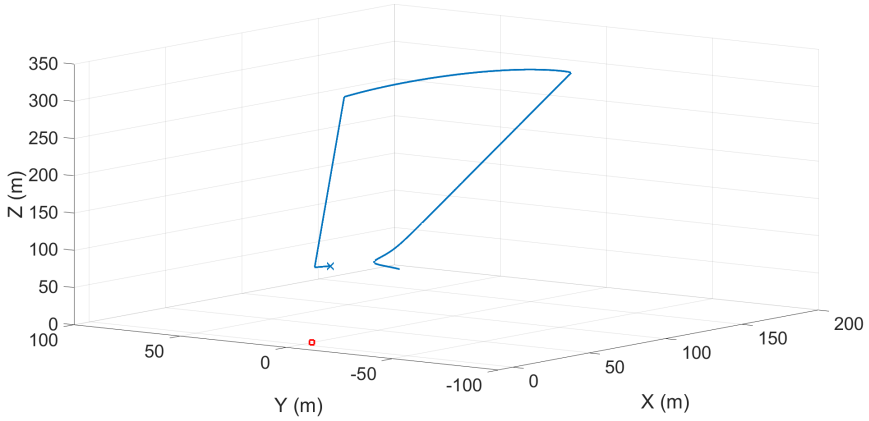

Figure 4.6 Kite trajectory for a single production cycle

the reel-in phase, as discussed in sections 4.3 and 4.4. The change in state variables ($\boldsymbol{r}, \boldsymbol{\phi}, \boldsymbol{\theta}$) and control variables is shown in Fig.4.7 and 4.8 respectively. The instantaneous power generation for one cycle during the simulation is plotted in Fig.4.9

It is seen that an average power of 2.5 kW is generated during the reel-out phase, whereas 1 kW is consumed during the reel-in phase. The complete cycle generates a net power of 1.5 kW. Section 4.5.2 compares this power generation with the power generated while considering the effects of flight in a roll-induced trajectory.

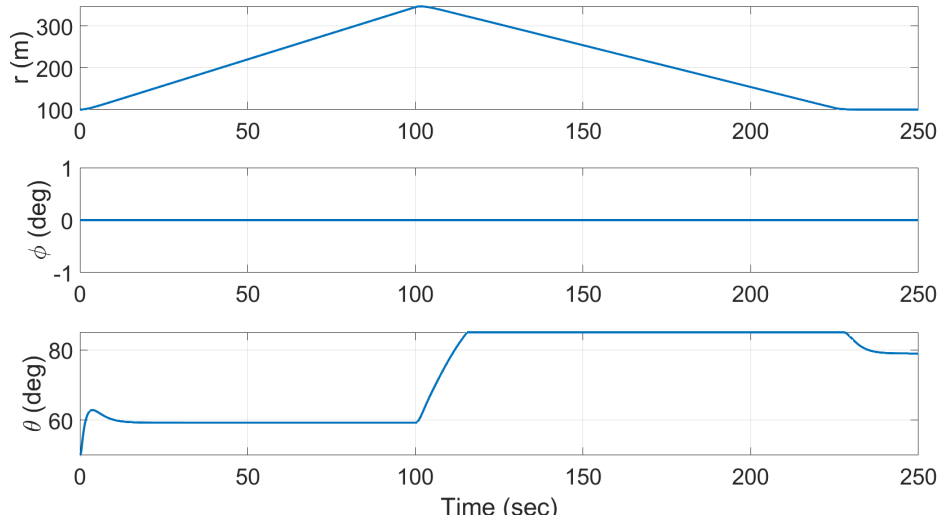

Figure 4.7 State variables for an open loop power production cycle without a roll induced trajectory

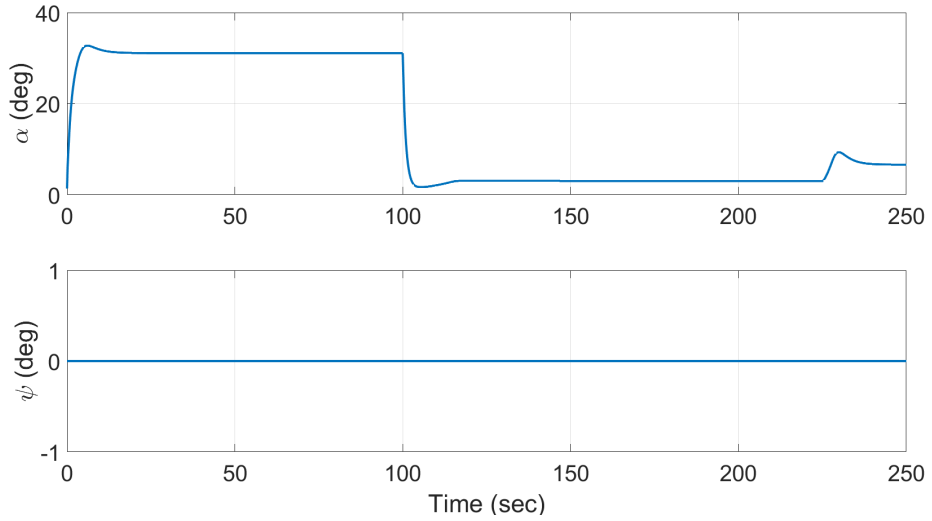

Figure 4.8 Control variables for an open loop power production cycle without a roll induced trajectory

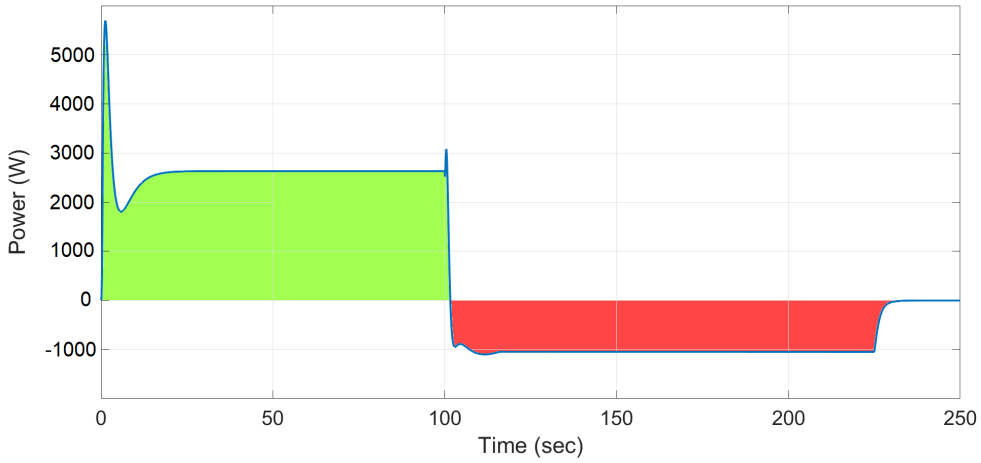

Figure 4.9 Instantaneous power generation for a single cycle without a roll induced trajectory

4.5.2 Power generation with roll induced trajectory

The simulations presented in this section are performed while acting on the roll angle to steer the kite in the desired trajectory. In the scope of open-loop simulations, no reference input trajectory is selected. The objective is to analyze the effect on power generation in an arbitrary trajectory generated by acting on the roll angle. A square wave with an amplitude of ± 3 m and frequency of 0.05 Hz is applied as the input

(Δ_l) to the roll angle. The simulation parameters are given in Table 4.3

Table 4.3 Simulation parameters for an open loop power production cycle with roll induced trajectory

Initial Conditions		Control Variables	
Wind speed ($\mathbf{V_w}$)	7.5 $\mathrm{m/s}$	Reel out velocity ($\dot{r}_{out}$)	2.5 $\mathrm{m/s}$
Elevation angle ($\boldsymbol{\theta}$)	$50°$	Reel in velocity ($\dot{r}_{in}$)	-2 $\mathrm{m/s}$
Azimuth angle ($\boldsymbol{\phi}$)	$0°$	Pitch angle (α_0) traction	$25°$
Initial tether length	100 m	Pitch angle (α_0) retraction	$0°$
Minimum tether length (r_{min})	100 m	Roll angle input (Δl) traction	$\pm 3m$, 0.05 Hz
Maximum tether length (r_{max})	350 m	Roll angle input (Δl) retraction	0

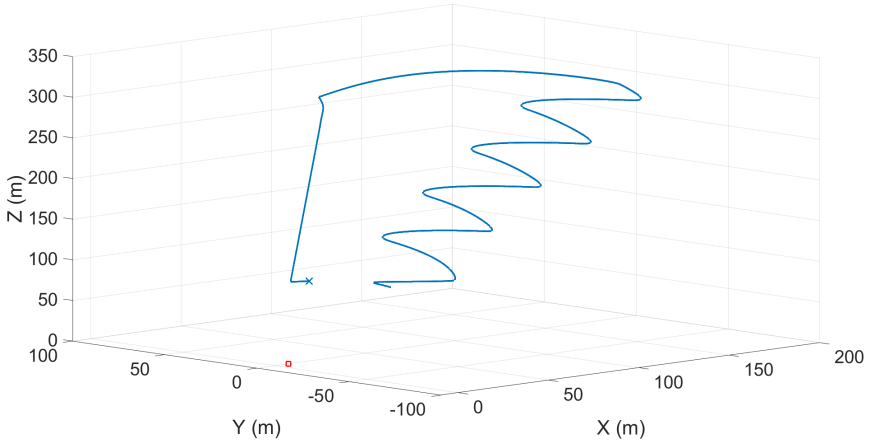

Figure 4.10 Kite trajectory for a single production cycle

Fig.4.10 shows a 3-D illustration for a single production cycle. The kite reels out along the X-axis and is steered in a curved trajectory alternating between a positive and a negative azimuth angle as a response to the roll input. When the tether reaches its maximum length, it is reeled back in until it reaches its minimum length. During the reel-in phase, the kite elevates itself to its equilibrium elevation at $85°$. The angle of attack is increased during the reel-out phase and deccreased during the reel-in phase, as discussed in Sections 4.3 and 4.4. The roll input is only applied during the reel-out phase. The change in state variables ($\boldsymbol{r}$, $\boldsymbol{\phi}$, $\boldsymbol{\theta}$) and control variables is shown in Fig.4.11 and 4.12 respectively. The instantaneous power generation for one cycle

during the simulation is plotted in Fig.4.13

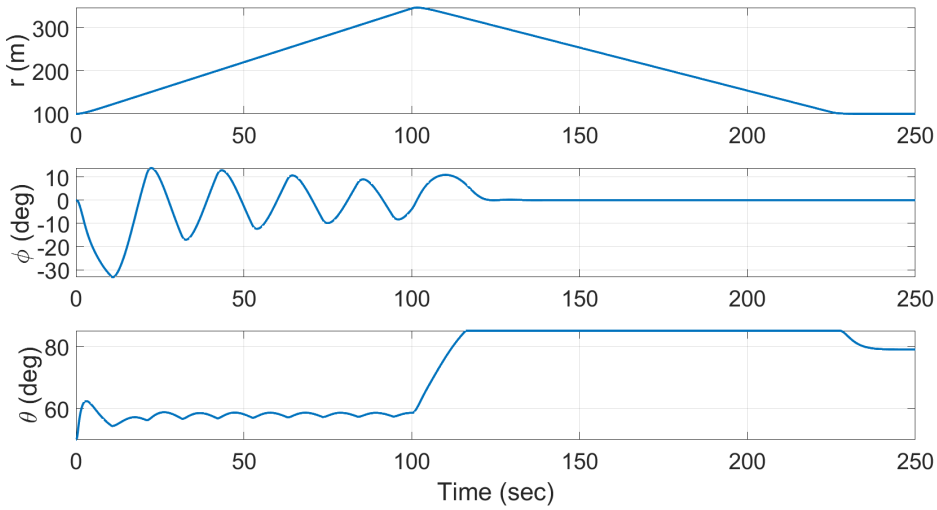

Figure 4.11 State variables for an open loop power production cycle with a roll induced trajectory

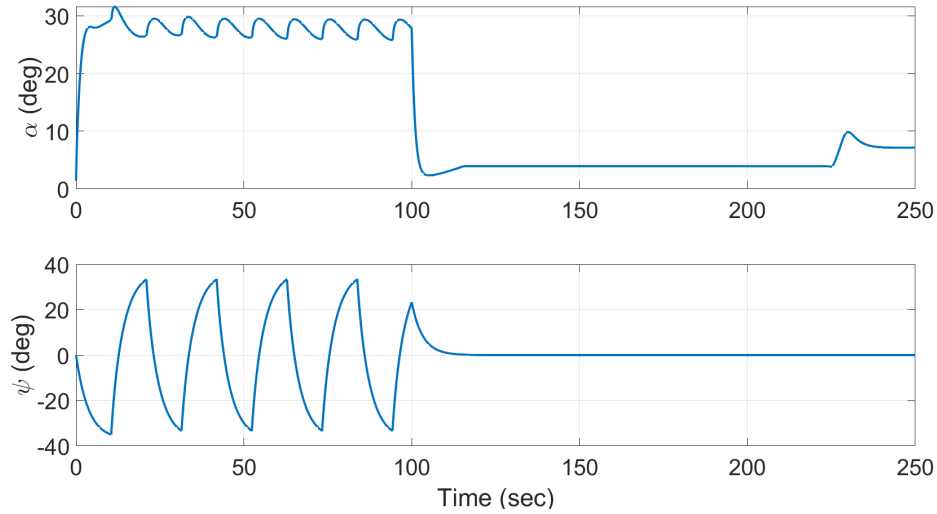

Figure 4.12 Control variables for an open loop power production cycle with a roll induced trajectory

By comparing the results with Fig.4.9, a significant increase in the instantaneous power generation is observed due to the inclusion of roll angle dynamics on kite trajectory. The increase in power production can be justified using Eq.(3.26). Adding

roll angle to the system dynamics increases the Centrifugal and Coriolis force components. Since only the centripetal force has vector projection in the $\boldsymbol{r}$ direction, which influences the tether tension and power, most of the optimal trajectories mentioned in the literature are constructed around circular or curved paths. Net power of 3.4 kW is generated for the complete cycle, which is more than twice the power output previously obtained in Section 4.5.1.

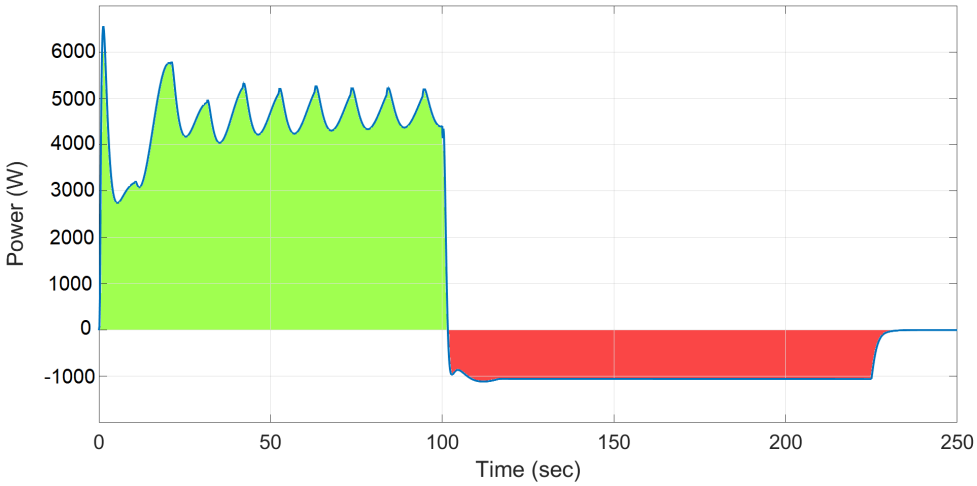

Figure 4.13 Instantaneous power generation for a single cycle with a roll induced trajectory

4.6 Scalability

Table 4.4 Kite specifcations

Area (A)	25 m^2
Mass (m)	22 kg
Wing span (b)	11 m

Compared to their large aspect ratios, the extraordinary lightweight of kites is one of the main benefits of using them as wind power extraction devices. Scaling the kites to a larger dimension to extract more wind power is extremely viable in terms of physical and economic considerations. The power output presented in Fig.4.13 is compared against a kite of larger dimensions. The physical parameters, taken from

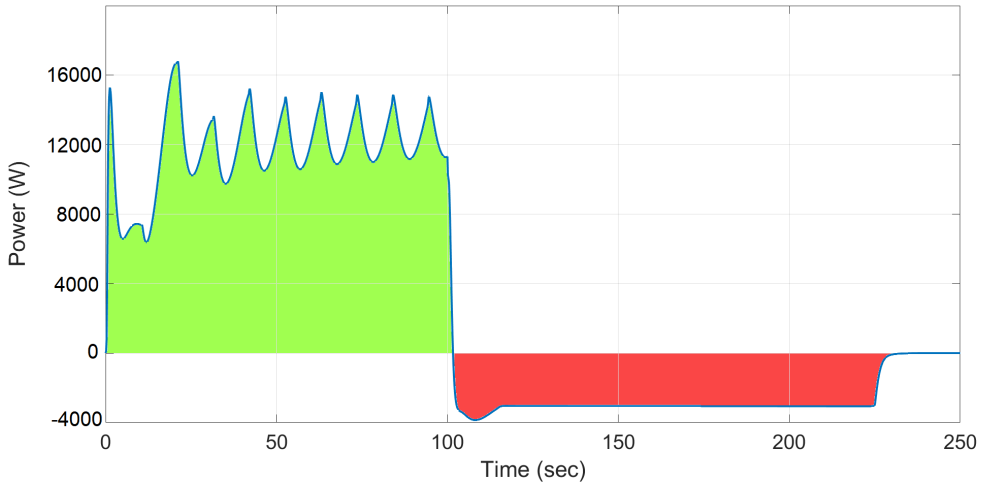

Figure 4.14 Instantaneous power generation for a single cycle of a larger scaled kite

an LEI V3 experimental prototype kite (Oehler & Schmehl, 2018), are presented in Table 4.4. The rest of the simulation parameters are kept constant with the simulation shown in Section 4.5.2 and are given in Table 4.3

The comparison of Fig.4.14 with Fig.4.13 shows a notable increase in the instantaneous power output for the reel-out phase. One complete cycle generates a total net power of about 8.5 kW.

CHAPTER 5

TRAJECTORY CONTROL OF AWE SYSTEMS

Trajectory control is a crucial aspect of AWE Systems for maximizing power output. The power output of AWE systems is significantly increased by controlling the kite to fly in what is known as a crosswind pattern, which is generally perpendicular to the direction of the wind (Loyd, 1980). Trajectory control is also necessary for safety considerations, i.e. having the kite flown in predefined trajectories minimizes the risk of system failure due to uncontrolled flight, which could lead to ground collision events and damage the ground station components. Flight trajectories with a circular basis are shown to be desirable flight paths for maximum power production during the traction phase. A similar conclusion can be inferred from the discussion presented in Section 4.5.2.

The optimum trajectories for maximising the power output are "figure-of-eight" trajectories as shown by (Canale et al., 2007; Ilzhöfer et al., 2007; Williams, 2006; Williams, Lansdorp, & Ockels, 2008). (Argatov & Silvennoinen, 2010) further made a distinction in analyzing the energy efficiencies of "laying figure-of-eight: ∞" and "vertical figure-of-eight: 8" trajectories. Although the vertical trajectories have greater energy efficiency, the most commonly used trajectory for kite control is the laying figure-of-eight. There is the risk of losing control of the kite and having it fall to the ground when flying vertical figure eight trajectories quickly towards the earth at high speeds.

The different control strategies used in kite trajectory control are mentioned in the literature in Section 2.7. The thesis employs decentralized control approach to control the kite trajectory. Separate controllers are designed for the control variables mentioned in Section 3.4. The flight trajectory controller produces the desired trajectory

by acting on a single control variable, the course angle of the kite, which is manipulated by changing the roll angle of the kite. The reeling velocities and the angle of attack are controlled separately.

5.1 Course Angle

The course angle χ introduced in this section is a critical system parameter for flight analysis and controller design. It is the angle between the local north axis and the velocity vector in the tangent plane, as shown in Fig, 5.1. The concept of course angle is used extensively in aircraft and mobile robotics literature (Beard & McLain, 2012; Corke, 2011). It conveys an impression of the aircraft's direction of heading and is used as a control input for trajectory tracking and path following applications. A dedicated frame known as the North-East-Down (NED) frame is used in most literature for navigation applications. The spherical coordinate system described in Section 3.2.1 can be used analogously to the NED navigation frame. Since the $\vec{e_\theta}$ unit vector is always pointing towards the zenith position, it can be used parallel to the direction of the North unit vector, $\vec{e_\phi}$ point in the east direction. These two unit vectors define the local tangent plane to the sphere. The course angle for the tethered kite model can then be defined as

$$\begin{aligned}\chi(t) &= \arctan 2\left(\frac{\vec{\mathbf{V}}_{\mathbf{k},[L]}(t)\cdot\vec{e_\phi}(t)}{\vec{\mathbf{V}}_{\mathbf{k},[L]}(t)\cdot\vec{e_\theta}(t)}\right), \\ &= \arctan 2\left(\frac{\dot{\phi}(t)\cos\theta(t)}{\dot{\theta}(t)}\right),\end{aligned} \tag{5.1}$$

where $\vec{\mathbf{V}}_{\mathbf{k},[L]}$ is the velocity of the kite in the local tangent frame, and arctan2 is the four quadrant inverse tangent function such that $\chi \in (-\pi, +\pi)$. if $\chi = 0$, the kite travels northward toward the zenith position. If $\chi = \frac{\pi}{2}$, the kite is travelling parallel to the ground in the east or $\vec{e_\phi}$ direction. If $\chi = \pi$, the kite travels directly towards the ground. Since the course angle depicts the kite's flight characteristics with only a single scalar variable, it is especially well suited for feedback control.

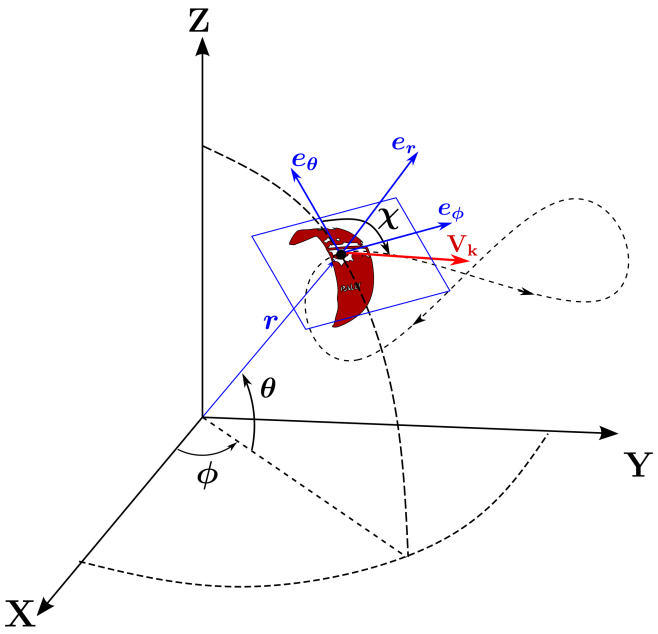

Figure 5.1 Course angle

5.2 Controller Design

A classical feedback controller is designed to control the course angle, introduced in Section 5.1, to have the airborne kite fly in the desired trajectory. The laying figure-of-eight is chosen as the desired trajectory in the scope of this thesis based on the results presented in (Argatov & Silvennoinen, 2010). Unlike the NMPC approaches mentioned in Section 2.7, the control inputs are decoupled, and separate control structures are designed for each control variable. The controller design presented in this section deals with the trajectory control of a kite in its traction phase. Reeling speeds and the angle of attack are controlled separately.

The controller design employs a cascaded control structure with outer and inner loops, as shown in Fig.5.4. The task of the overall feedback controller can be separated into guidance and control. The outer loop deals with the guidance algorithms for trajectory generation, and the inner loop deals with the control logic for trajectory tracking. The outer loop feeds back the current position of the kite in the local tangent plane in terms of ϕ and θ coordinates. A reference course angle χ_{ref} is computed by a trajectory generation algorithm using a guidance strategy of choice and fed to the inner control loop. The inner loop feeds back the current course angle χ of the kite computed using

Eq.(5.1). The control system's inner loop minimizes the course angle error e_χ by adjusting the steering input Δl. For the sake of feasibility and easy implementation, a proportional-integral-derivate (PID) controller is used to minimize the error over time.

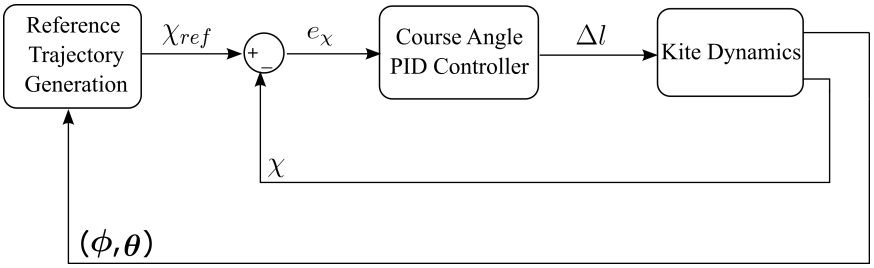

Figure 5.2 Control structure based on the course angle

5.3 Outer-Loop : Trajectory Generation

The outer loop of the control structure shown in Fig.5.4 parameterizes the flight trajectory using either a continuous reference source or a few reference points. In either case, the Reference Trajectory Generation block generates a reference course angle to guide the kite on the desired reference path. This section discusses two guidance strategies that produce a laying figure-of-eight reference trajectories.

5.3.1 Path following control algorithm

In the first approach, a path-following algorithm is adapted that is similar to the ones used in mobile robotics and aerospace application. The desired reference trajectory is pre-computed as a function of time using the Lissajous curves (JUN et al., 2014)

$$\begin{aligned} \phi_{ref}(t) &= \phi_0 + \Delta\phi \cos t \,, \\ \theta_{ref}(t) &= \theta_0 + \Delta\theta \sin 2t \,. \end{aligned} \tag{5.2}$$

The required reference course angle to change the direction of the kite velocity vector towards a point on the reference trajectory, as shown in Fig.5.3, is computed using

the following equation

$$\chi_{ref}(t) = \arctan 2 \left(\frac{(\phi_{ref}(t) - \phi(t)) \cos \theta(t)}{\theta_{ref}(t) - \theta(t)} \right). \tag{5.3}$$

The reference course angle is then compared with the actual course angle of the kite, and the error is fed into a PID controller that aims to minimize the course angle error by manipulating the steering input Δl.

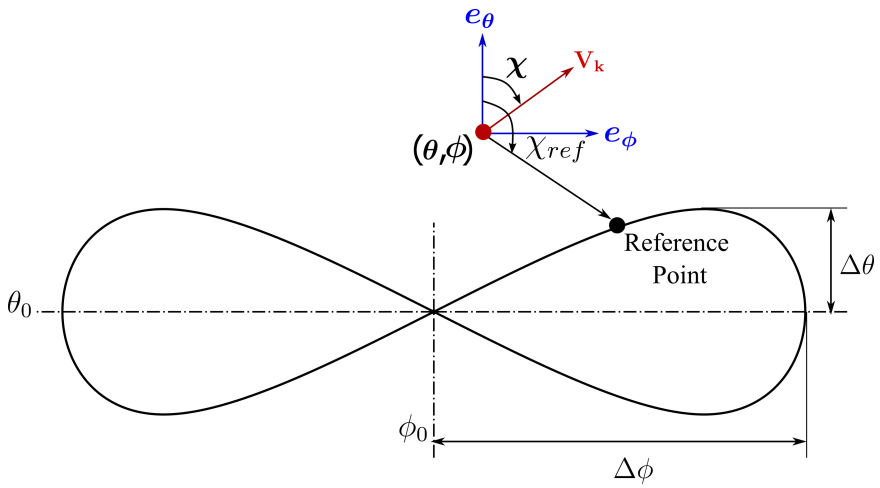

Figure 5.3 Path following guidance method

The contribution of such an approach to the goals of this thesis is limited to its introduction since the initial simulation results obtained with this guidance strategy were not satisfactory and could not achieve the desired robustness. Although this approach produces beneficial results in aerospace applications where the path does not change abruptly with time, the kite has to execute sharp turns in high crosswind velocities, making tuning the controller challenging. The tuning also becomes demanding when different trajectories are pre-computed for different flight scenarios to analyze the net power produced by the system.

5.3.2 Two point control algorithm

Considering the discussion presented in Section 5.3.1, the objective of a guidance strategy is to create an algorithm with minimal tuning parameters that can produce figure-eight crosswind paths without having to compute a whole trajectory in ad-

vance to serve as a reference. In contrast to the kite strictly following a pre-defined path, giving the kite some flexibility to determine its course while tracking between two points is deemed a more elegant solution. A controller is developed that uses two points defined in the tangent flight plane by their elevation (θ) and azimuth (ϕ) coordinates. These points are termed attractors or reference points. Each point acts as a threshold to switch from one reference point to another. The kite flies between the two reference points in figures of eight trajectories until the tether reaches its maximum length.

The two-point control strategy has been proposed in the literature by (Erhard & Strauch, 2012). The control strategy is based on a bang-bang feedback controller with rapid transitions between two states. (Kamien & Schwartz, 2013). Therefore the two-point control is also referred to as the bang-bang. A similar approach to designing the controller is presented in the following steps.

1. Two Tracking points are defined in the tangent (ϕ, θ) plane. They are represented as $P_+ = (\phi_+, \theta_+)$ and $P_- = (\phi_-, \theta_-)$, where $\phi_+ > \phi_-$ and $\theta_+ = \theta_-$. Based on the position of kite in the tangent plane, one of the tracking points is set as an active reference point, $P_{ref}(t_n) = (\phi_{ref}(t_n), \theta_{ref}(t_n))$.

2. The reference course angle is obtained at every time step (n) by Eq.(5.3).

3. The actual course angle of the kite is calculated. A reference error is generated, and a PID controller acts on the steering input to minimize the error.

4. As soon as the kite reaches the desired tracking point, the active reference point is switched, and the kite starts tracking the new reference point. The reference points are switched according to the following algorithm

$$P_{ref}(t_n) = \begin{cases} P_+, & \phi(t_n) < \phi_- \\ P_-, & \phi(t_n) > \phi_+ \\ P_{ref}(t_{n-1}), & other\ . \end{cases} \tag{5.4}$$

When the active reference point has been switched, the kite begins to maneuver a turn due to the action of the inner control loop. The turn is executed so that the kite heads towards the zenith first and then towards the active reference point. The

periodic attainments of subsequent turns allow the kite to mimic laying figure-of-eight trajectories as it maneuvers between the two tracking points. The reference course angle is fed through a second-order Butterworth filter to deliver a smooth input to the inner loop control. A Butterworth filter is a low pass filter that dampens signals with frequencies higher than a chosen cutoff frequency while allowing signals with frequencies lower than the cutoff frequency (Karki, 2002).

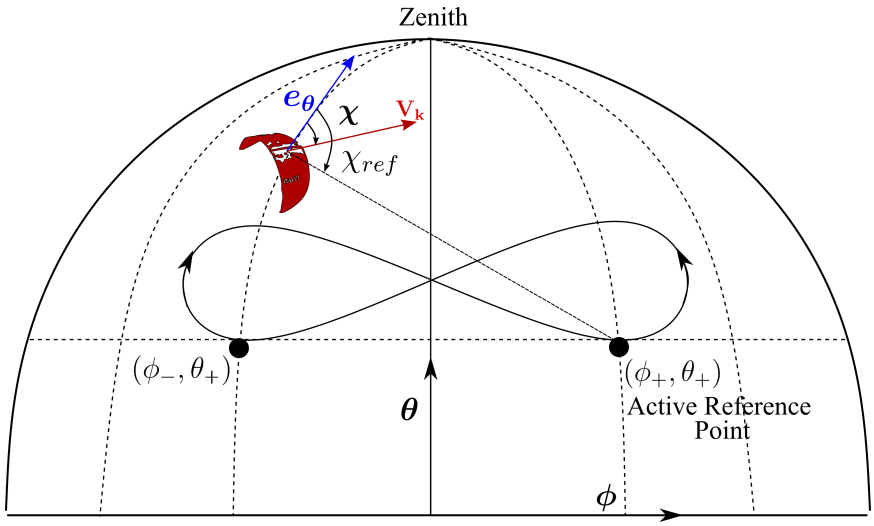

Figure 5.4 Illustration of two point reference tracking or bang-bang control guidance

Therefore, two key variables to be selected in the bang-bang guidance strategy are the tracking points and the cutoff frequency, which can be tuned intuitively to influence the geometry of the resulting trajectory. Higher cut-off frequencies have shown to execute sharper turns, while lower cut-off frequencies tend to produce wider turns. It is a control parameter optimized for maximum power generation during a pumping cycle.

5.4 Inner-Loop: Trajectory Tracking

The inner loop minimizes the course angle error generated by the outer loop to track the kite in the desired trajectory by modifying the steering input. Classical PID control is considered an appropriate control logic for trajectory tracking purposes. A PID controller operates by regulating an output to drive a system value to the desired state.

The PID control law is given as

$$\begin{aligned} e_\chi &= \chi_{ref} - \chi \,, \\ u(t) = \Delta l &= K_P e_\chi(t) + K_I \int_0^t e_\chi(t)\, dt + K_D \frac{\mathrm{d}e_\chi(t)}{\mathrm{d}t} \,, \end{aligned} \tag{5.5}$$

Where e_χ is the error signal generated by comparing the reference course angle to the actual course angle of the kite, and K_P, K_I, and K_D are the controller's proportional, integral and derivative gains. A PID control loop incorporates elements of all three types of control: proportional, integral, and derivative. The proportionality constants K_P, K_I and K_D can be tuned to alter each control's contribution. By modifying the values of these constants, one or more of the control can be made dominating or subtle in the system.

The K_P gain multiplied by the error yields the proportional control. Proportional control counteracts error by introducing an opposite impact proportional to the error. The proportional controller's objective is to have a significant immediate effect on the output and decrease the error by making the computed value of the control variable close to the desired reference. The proportional controller's impact on the output reduces as the error gets smaller.

Integral control identifies and corrects protracted trends in error throughout the simulation time. The integral action gives the cumulative error that should have been adjusted earlier. The controller output is then calculated by multiplying the cumulative error by the integral gain K_I. Integral controllers perform quite effectively to eliminate the steady state error; however, in the case of tracking a trajectory, the course angle of the kite changes abruptly with time. The change is even more accelerated for shorter trajectories and higher wind speeds corresponding to faster kite dynamics. Therefore, a significant improvement in the controller performance is not anticipated for reference tracking by the contribution of integral control.

The derivative control action identifies and resists sudden changes in the system. The derivate control, therefore, leads the system towards a smooth response. The derivative control is determined by multiplying the derivative gain K_D with the derivate or the rate of change of the reference error. If a system's output approaches its reference state too fast, the derivative control action will prevent the system from overshooting the desired state by limiting its output. This causes a damping effect that improves

overall stability. Overshoot is a highly undesired effect for a kite tracking a flight trajectory since it can introduce unnecessary oscillations in the system that can cause the kite to lose control or result in an undesirable trajectory. Derivate action also helps to provide a smooth response, especially during fast-turning maneuvers, by limiting any abrupt changes in the system.

The PID gains of the controller are initially tuned manually and then optimised for different system parameters, based on the analysis of different simulation scenarios presented in Chapter 6.

CHAPTER 6

CLOSED LOOP SIMULATIONS FOR OPTIMIZED TRAJECTORY AND POWER PRODUCTION

This chapter presents the closed-loop simulation results based on the control architecture presented in Chapter 5. The kite model is based on the dynamic equations derived in Chapter 3 and simulated in Matlab/Simulink©. The objective of this chapter is to systematically analyze the closed loop behaviour of the kite under different flight conditions and tune the control parameters to achieve the desired controller robustness.

A coherent organization of the chapter is presented in the following manner. Section 6.1 evaluates the robustness of the controller to follow a laying figure-of-eight without any reference to the power output. The PID controller gains are tuned for different flight variables in this section. Section 6.2 investigates the behaviour of a laying figure-of-eight trajectories under different configurations, such as trajectory width and position in the wing window. The control variables that influence the geometry of the figure eight trajectory are tuned to achieve an optimal trajectory configuration corresponding to maximum power production. Finally, Section 6.3 presents simulations for a complete power cycle. The main aim of the chapter is to design a robust controller to achieve maximum power output from a kite flying in crosswind figures of eight trajectories. The system's power output is also analysed in terms of its efficiency.

The physical specifications of the kite used in the simulations are presented in Table 6.1. The values are adapted from Kitepower Falcon, a 100 kW onshore operational prototype developed by Kitepower™. For the sake of coherence with the goals of this chapter, all the simulations presented in this chapter are performed using the same kite

parameters. The influence of changing the physical parameters of the kite is already discussed in sections 4.6. At this point, it can be intelligibly deduced that larger kites with greater surface areas would lead to higher power outputs. The simulations are run using the ODE 4 Runge-Kutta integration method with a fixed step size of 0.01.

Table 6.1 Kite specifications for closed-loop simulations

Area (A)	50 m^2
Mass (m)	30 kg
Wing span (b)	20 m

6.1 Closed-Loop Trajectory Tracking

This section aims to analyze the response of a closed loop control structure as illustrated in Fig. 5.4 to track a kite in a figure eight trajectory. The system's power output is not evaluated at this stage since it is imperative to initially obtain a robust control response that tracks the kite in the desired trajectory.

The system is initiated with a constant wind speed of 7 $\mathrm{m/s}$ in the X-direction. The reference points for the trajectory generation are set in the tangent (e_ϕ, e_θ) plane as $T_+ = (+15°, +50°)$, and $T_- = (-15°, +50°)$. The points are defined in degree units and converted to radians as input to the guidance algorithm. The simulations are performed with a constant tether length, and the pitch input is set as 10°. A PI controller is used initially, and the controller gains are arbitrarily estimated as $K_p = 3$ and $K_I = 1$. The cut-off frequency is specified as 90 °/sec or $\frac{\pi}{2}$ $\mathrm{rads/sec}$.

The simulations show unsatisfactory results regarding trajectory tracking using the initial controller settings. The 2D trajectory of the kite plotted in the (e_ϕ, e_θ) plane is shown in Fig.6.1. Although the bang bang switching algorithm performs as expected, switching the active reference point as the kite crosses its azimuth coordinate (Fig.6.2), the kite fails to track the elevation target. Instead of tracking the elevation at 50°, the kite tends to fly towards its equilibrium elevation at 70°. The resulting

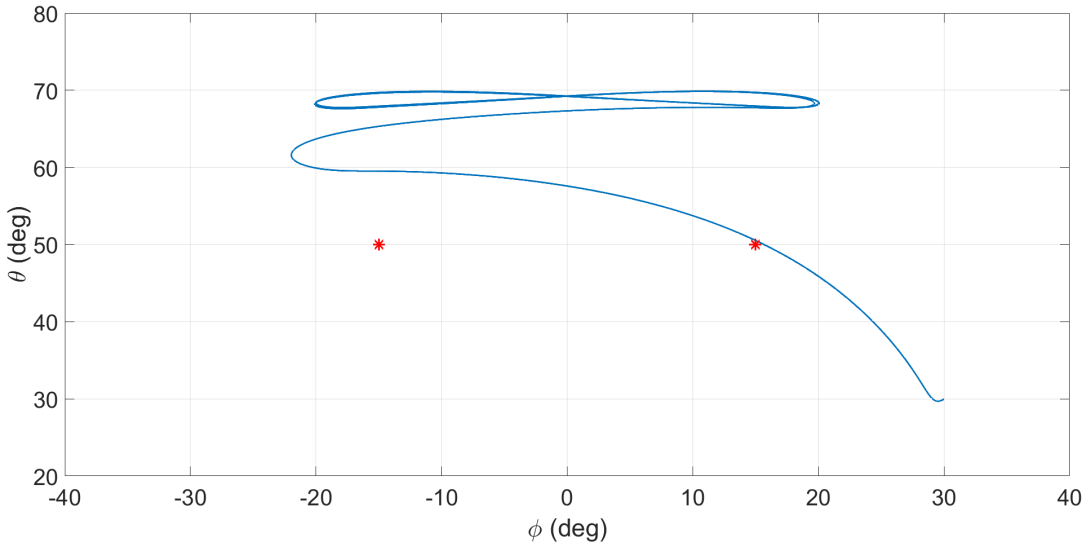

Figure 6.1 Trajectory of the kite plotted in the tangent plane for $K_P = 3$, $K_I = 1$ and $\mathbf{V_w} = 7\ \mathrm{m/s}$

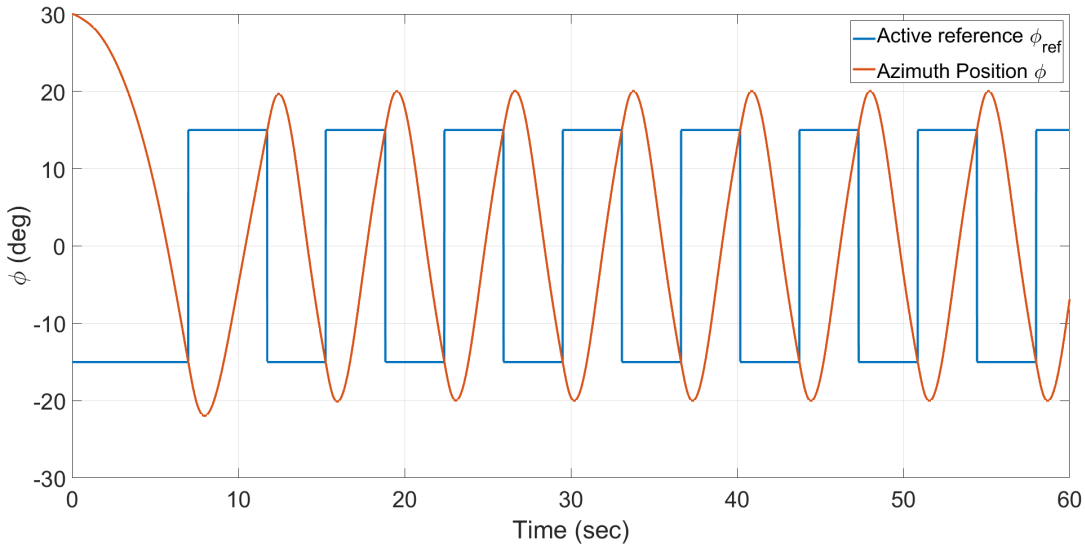

Figure 6.2 Bang-bang switching algorithm

trajectory is a flattened figure-of-eight. The response of the control inputs and the state variables is plotted in figure 6.3 and 6.4 respectively.

To achieve better performance in trajectory tracking, a more vigorous control action is required that allows reliable tracking of the reference point yet is tolerant enough to enable smooth execution of turning maneuvers as the kite tracks between two tracking points. Tracking becomes even more challenging when the active reference points

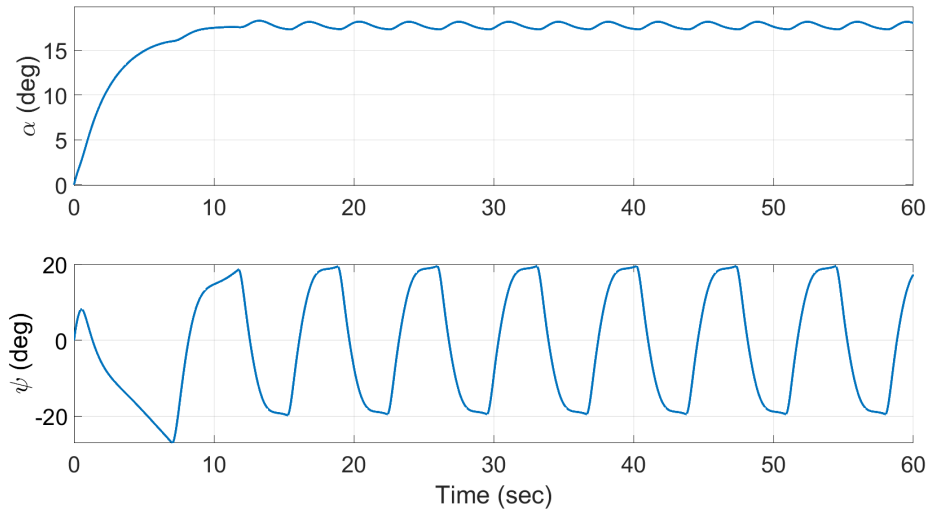

Figure 6.3 Control inputs for the kite simulated with $K_P = 3$, $K_I = 1$ and $\mathbf{V_w}$ = 7 $\mathrm{m/s}$

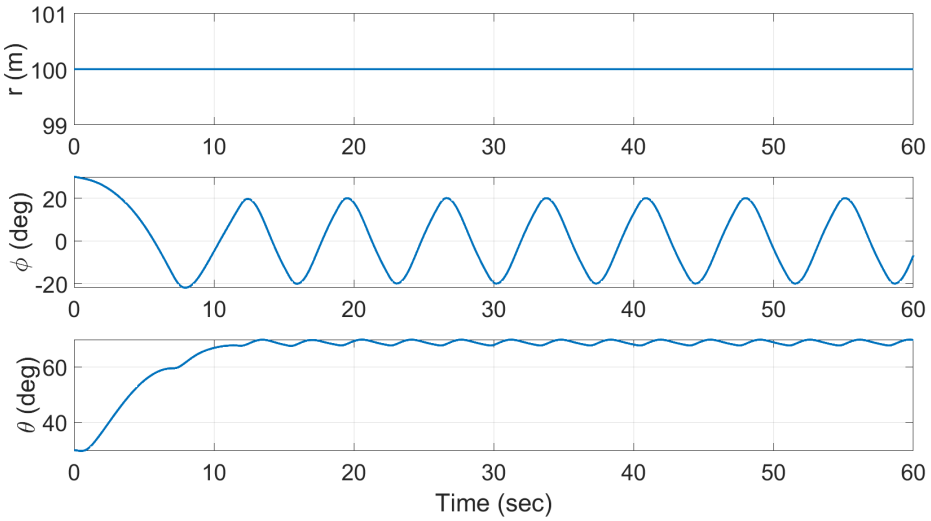

Figure 6.4 State variables for the kite simulated with $K_P = 3$, $K_I = 1$ and $\mathbf{V_w}$ = 7 $\mathrm{m/s}$

switch between on and off state for smaller trajectories. Faster wind conditions are another challenge for the tracking problem as the kite stages faster dynamics with the risk of losing control during fast-turning maneuvers.

The PID gains are tuned manually over the course of several simulations to achieve the desired robustness. Adhering to the effect of flight conditions on PID gains in

relation to the discussion presented in Section 5.4, it is noted that increasing the proportional gain considerably improves the tracking response as anticipated. Any change in the integral gain has no significant effect on the output as already anticipated. A derivate gain is also added to limit the steering output in response to faster error dynamics. It is particularly effective in bang-bang control applications where the reference abruptly switches states.

The effect of system variables on PID gains to achieve the desired robustness is also investigated. It is found that $K_P \propto \mathbf{V_w}$ and $K_D \propto b$, where $\mathbf{V_w}$ is the wind speed, and b is the wing span of the kite. Multiple simulations are performed for different wind speeds and kite geometries, the PID gains are tuned manually for each case, and a linear relationship between the PID gains and the system variables is obtained. The optimized PID gains are defined as $K_P = 3\,\mathbf{V_w}$ and $K_D = 0.5\,b$. It is worth mentioning that other system parameters, such as kite area, mass, lift and drag coefficients etc., also influence the controller gains. Although the physical parameters of the kite are kept constant throughout the simulations presented, the controller was tested for varying kite parameters for completeness and to test the complexity of the controller. It was noted that the controller performs reliably using the kite parameters given in Tables 4.1 and 4.4.

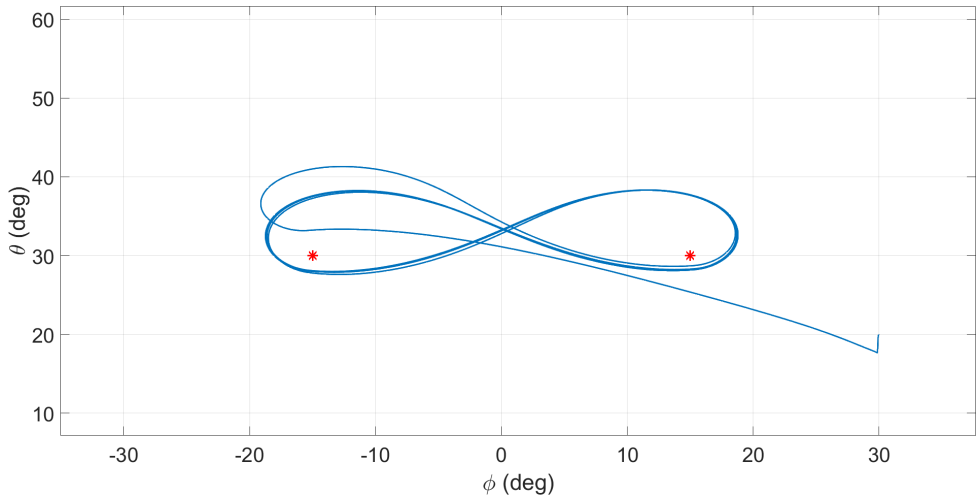

Figure 6.5 Trajectory of the kite plotted in the tangent plane for the tuned PID controller gains. $K_P = 3\,\mathbf{V_w}$, $K_I = 1$, $K_D = 0.5\,b$ and $\mathbf{V_w} = 10\ \mathrm{m/s}$

Fig.6.5 shows the 2D trajectory of the kite under the ambient wind of 10 $\mathrm{m/s}$. The

PID gains are set as $K_P = 3\ \mathbf{V_w}$, $K_I = 1$ and $K_D = 0.5\ b$, the cut-off frequency is kept constant at $\pi/2$ rad. It is observed that the kite efficiently tracks between the two reference points (marked as red asterisks), in the desired figure-of-eight trajectories. The comparison of Fig.6.6 with Fig.6.4 notes the difference in the steering input stimulated by an increased proportional gain.

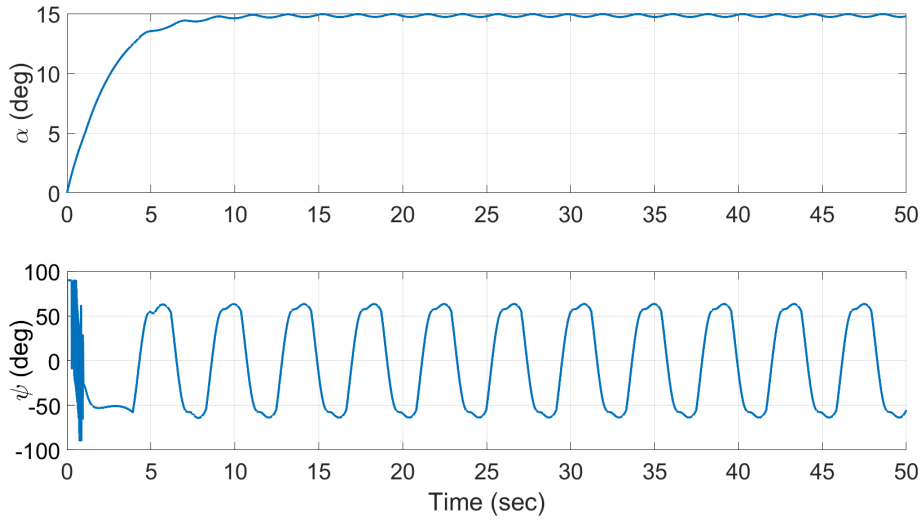

Figure 6.6 Control inputs to the system with the tuned controller PID gains. $K_P = 3$ $\mathbf{V_w}$, $K_I = 1$, $K_D = 0.5\ b$ and $\mathbf{V_w} = 10$ m/s

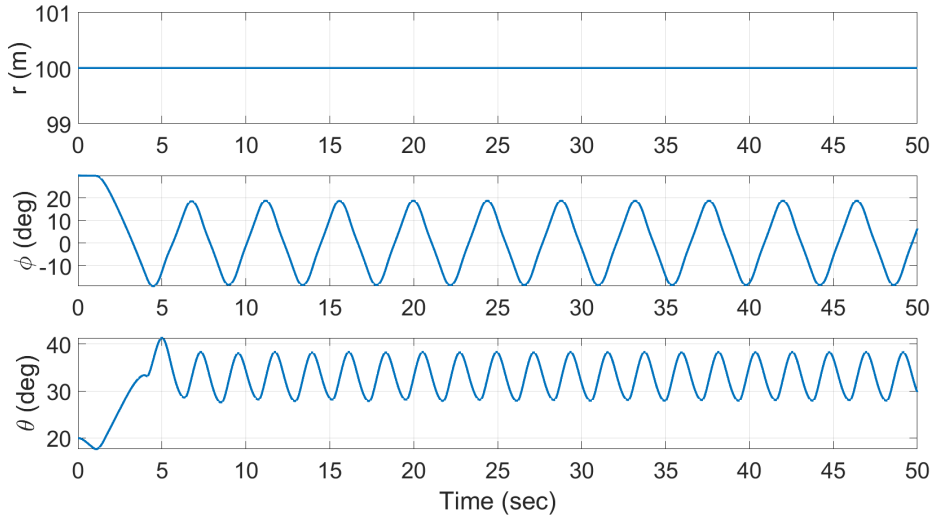

Figure 6.7 State variables of the system with the PID tuned controller gains. $K_P = 3$ $\mathbf{V_w}$, $K_I = 1$, $K_D = 0.5\ b$ and $\mathbf{V_w} = 10$ m/s

The robustness of the controller is also tested for different wind conditions. The resulting trajectories are illustrated in Fig.6.8. The controller performs effectively for different wind conditions under the updated PID gains. The resulting trajectories are observed to become wider as the wind speed increases. The width of the trajectories can be altered by regarding the cut-off frequency as another tuning control parameter. The effect of the cut-off frequency on the resulting trajectories is analyzed in Section 6.2.1 and optimized for maximum power production.

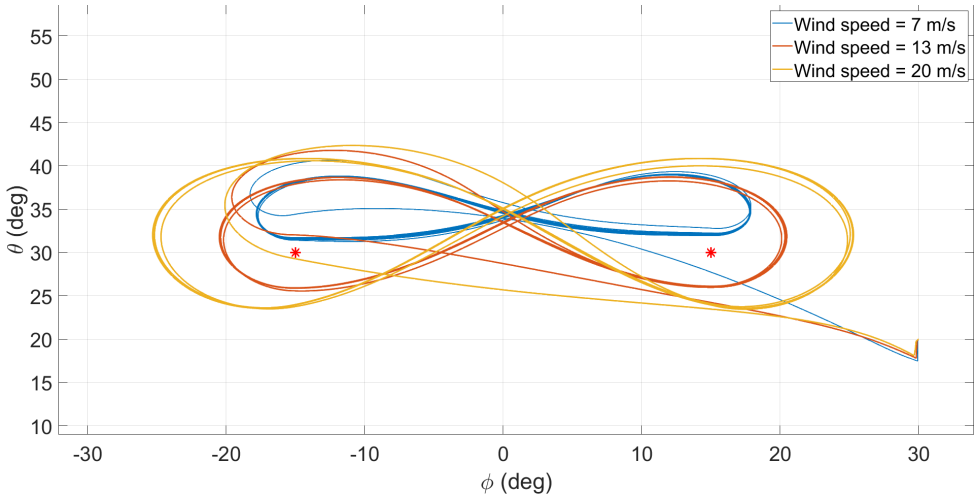

Figure 6.8 Trajectory of the kite plotted in the tangent plane for different wind speeds

6.2 Trajectory Optimization to maximize the power production

This section investigates the geometrical profile of a laying figure-of-eight trajectories in response to different inputs to maximize power production. The simulations are performed with a constant tether length. Therefore, the power output is analysed in terms of the tension force experienced by the tether. According to the discussion presented in Section 2.4, it should be observed that the maximum force is produced in the high power zone of the wind window. Therefore, this section aims to verify the assumption and tune the flight variables to optimize the flight trajectories restricted to the high power zone.

6.2.1 Effect of the cut-off frequency

As mentioned in Section 5.3.2, the reference course angle generated as an output of the trajectory generation algorithm is passed through a low pass filter that passes signals with a frequency lower than a selected cut-off frequency. Since the reference angle is changed abruptly as the kite passes the active reference tracking point, applying a low pass filter is necessary to provide a smooth reference course angle output signal. Higher cut-off frequencies correspond to sharper turns, and lower cut-off frequencies produce wider turns. The overall scale of the figure eight trajectory can be modified by altering the cut-off frequencies. The effect is evident in figure 6.9, which shows the obtained trajectories for three different cut-off frequencies. All three simulations keep the wind speed constant at 15 $\mathrm{m/s}$. The reference tracking points for the simulation are chosen as $T_+ = (+15°, +30°)$ and $T_- = (-15°, +30°)$, defined in the (e_ϕ, e_θ) plane. A higher cut-off frequency restricts the kite's trajectory around the reference tracking points by executing sharp turns. A lower cut-off frequency allows the kite to deviate further from the reference points.

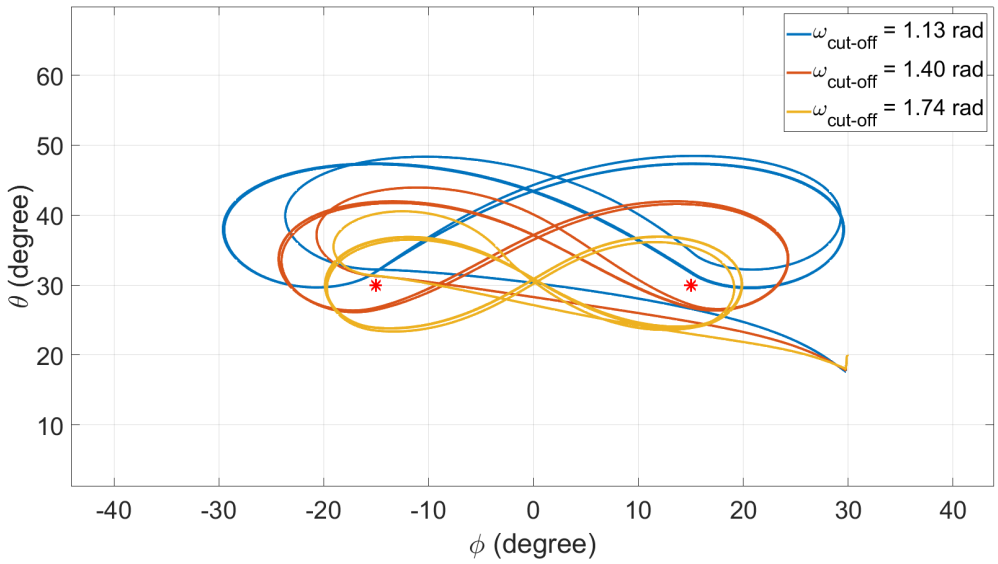

Figure 6.9 Kite trajectories plotted for different cut-off frequencies ($\omega_{cut-off}$), plotted for a constant wind speed of 15 $\mathrm{m/s}$

The power output of the kite is analyzed for the different trajectories. It is shown in

Fig.6.10 that the trajectories obtained with higher cut-off frequencies produce more Tension and consequently more power. The obtained results for the power output are as anticipated in reference to the discussion in Section 2.4, and the results presented in (Argatov & Silvennoinen, 2010). Lower cut-off frequencies allow the kite to deviate further in the wing window away from the high power zone. The selection of the reference target points is also an important parameter and must be placed within the high power zone of the wind window.

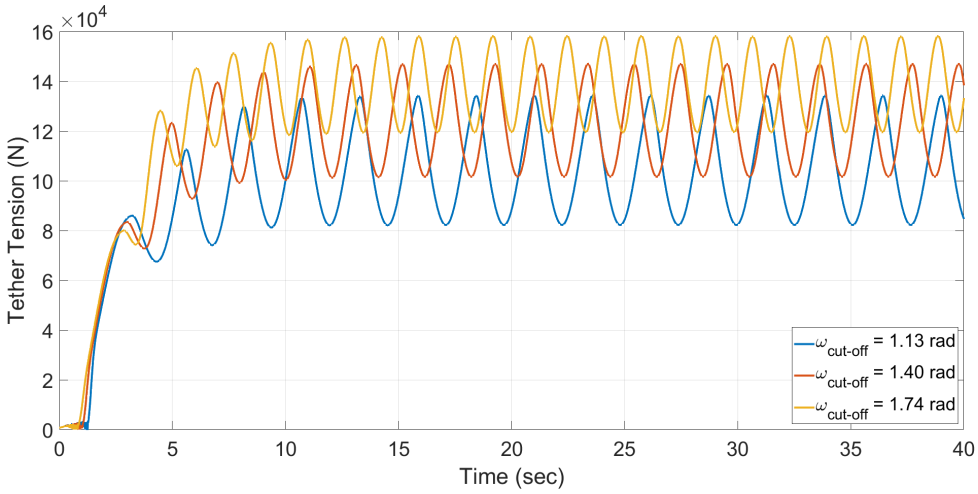

Figure 6.10 Tether tension for different cut-off frequencies ($\omega_{cut-off}$), for a constant wind speed of 15 $\mathrm{m/s}$

It is also observed in Fig.6.8 that the trajectories for a constant cut-off frequency still become wider around the tracking points as the wind speed increases. Although the power zone theoretically expands with greater wind speeds, the system's power output can be improved further by adjusting the cut-off frequency.

Instead of adjusting the cut-off frequency manually in each simulation for different speeds, it is related to the wind speed as $\omega_{cut-off} = k_c \mathbf{V_w}$. The cut-off gain k_c is initially adjusted manually to obtain an optimal value for the cut-off frequency for simulations performed at the wind speeds of 5 $\mathrm{m/s}$, 10 $\mathrm{m/s}$, 15 $\mathrm{m/s}$, 20 $\mathrm{m/s}$ and 25 $\mathrm{m/s}$. The system is automated by fitting a 3rd-order polynomial curve between these points. The selection of five points provides a good enough resolution for accurate curve fitting. A polynomial evaluation function in Matlab then returns the cut-off gain k_c for any input value of the wind speed $\mathbf{V_w}$ in the range of 5-25 $\mathrm{m/s}$. In

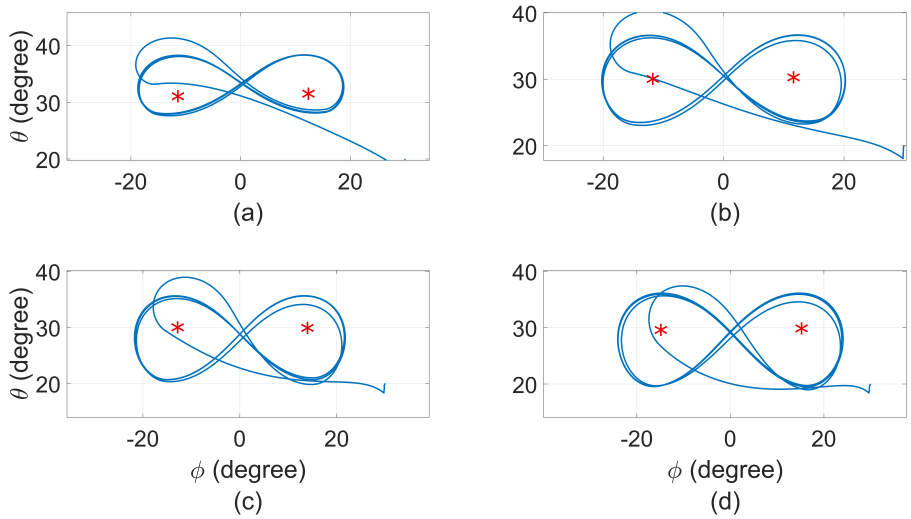

Figure 6.11 Kite trajectories plotted for different winds. The cut-off frequencies are optimized as a function of the wind speed. (a) $\mathbf{V_w}$ = 5 $\mathrm{m/s}$, $\omega_{cut-off}$ = 1.57 $\mathrm{rad/s}$ (b) $\mathbf{V_w}$ = 10 $\mathrm{m/s}$, $\omega_{cut-off}$ = 1.76 $\mathrm{rad/s}$ (c) $\mathbf{V_w}$ = 15 $\mathrm{m/s}$, $\omega_{cut-off}$ = 1.82 $\mathrm{rad/s}$ (d) $\mathbf{V_w}$ = 20 $\mathrm{m/s}$, $\omega_{cut-off}$ = 1.85 $\mathrm{rad/s}$.

Fig.6.11, Similar trajectories are shown to be obtained for different wind speeds by automatically adjusting the cut-off frequency.

6.2.2 Effect of the elevation angle

Two flight scenarios with different elevation angles are shown in Fig.6.12 to inspect the power output for both cases. The simulations are performed with a constant wind speed of 15 $\mathrm{m/s}$. The cut-off frequency, tether length and angle of attack are also kept constant for both cases. The tracking points are set at the elevations of 30°and 60°. A significant increase in the tension force is seen in Fig.6.13 as the kite lowers its elevation from 30°to 60°.

The notable increase in the tension force is directly attributed to the transition from the medium to the high power zone of the wing window, as illustrated in Fig.2.4. The results presented in this section seem to contradict one of the fundamental concepts of AWE systems: to extract wind power from high altitudes. It is important to note here that the wind velocity is assumed constant throughout the simulation. In reality,

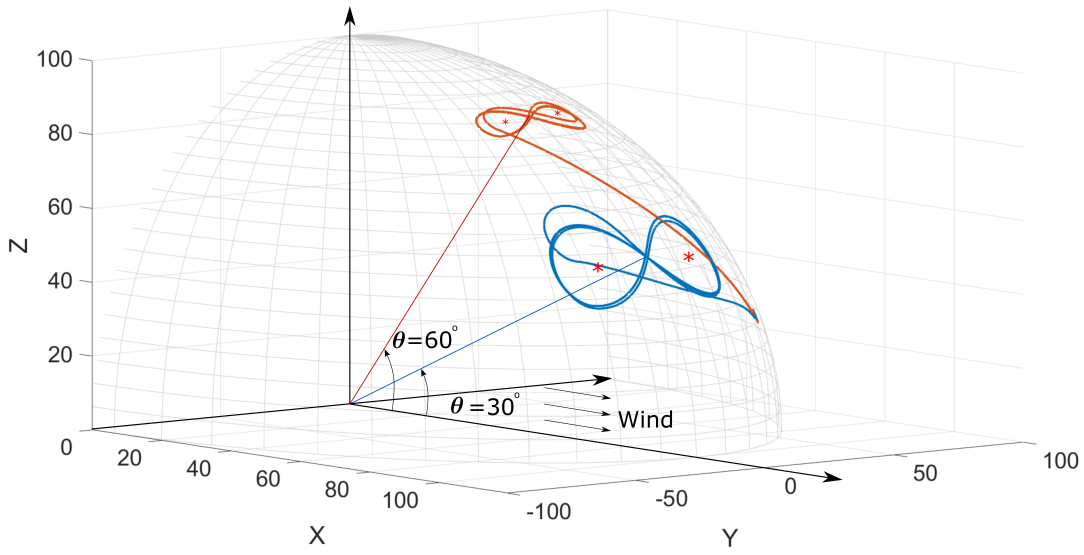

Figure 6.12 An illustration of kite trajectory for two different elevation angles

however, there is a wind velocity gradient and the wind speed inceases as the height from the ground level increases. The high altitude is achieved by increasing the tether length. A trade-off is generally made as a design characteristic between the tether length and the elevation angle. Most AWE systems operate with a tether length of 200-800 m. If the elevation angle is kept as 30°, it will correspond to an altitude of 100 - 400 m respectively. For comparison, one of the largest operational wind turbines, Haliade-X, has a maximum tip height of 260 m.

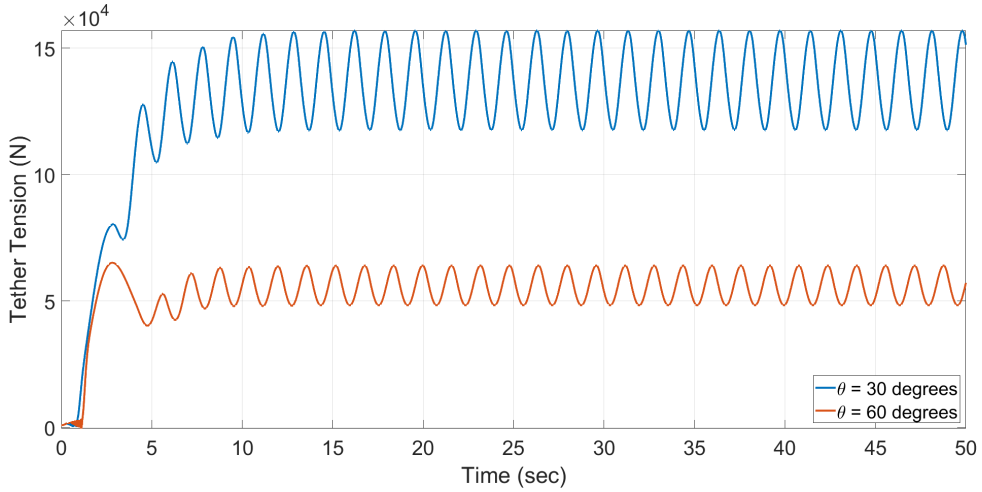

Figure 6.13 Tether tension plotted for two different elevation angles at a constant wind speed of 15 $\mathrm{m/s}$

6.2.3 Defining the trajectory in spherical vs inertial frame

During the traction phase, the tether length increases as it is reeled out constantly to produce power at the ground station. Until this point, the reference tracking points have been defined in the (e_ϕ,e_θ) plane to produce figure eight trajectories. An undesirable consequence of this method is observed in Fig.6.14. The kite's trajectory becomes wider along the Y-axis in the inertial frame as the kite is reeled out. As the trajectory becomes wider, it diverges from the high power zone. This result is shown in Fig.6.15, the tension force decreases as the trajectory becomes wider. Diverging trajectories along the Y axis also have implications for the operation of an AWE kite in a designated space as the area spanned by the kite becomes significantly larger.

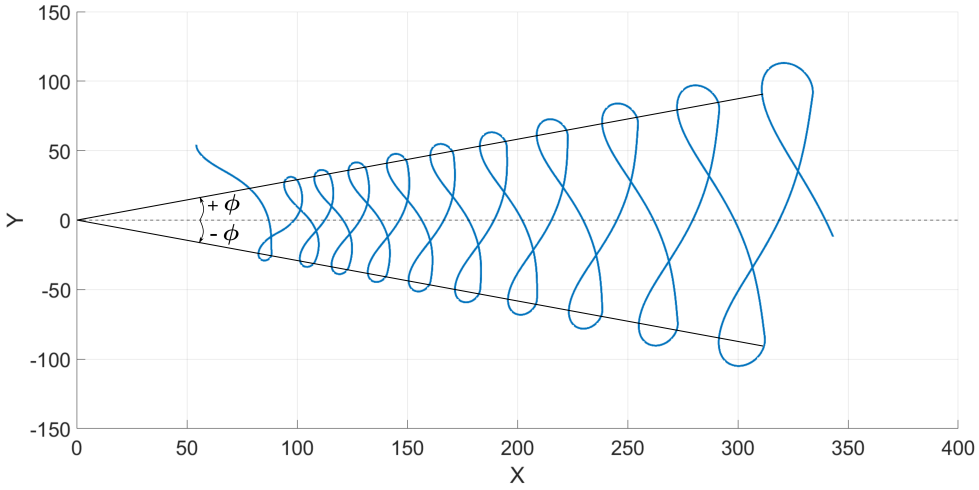

Figure 6.14 Kite's flight path in the X-Y plane in the inertial frame, with the reference tracking points defined in the local frame.

One way to avoid the divergence in trajectories with increasing tether length is to define the reference tracking points in the Intertial frame. Instead of defining the azimuth (ϕ) coordinate as a constant reference, the Y coordinate is defined and converted to its corresponding azimuth position. As a result, the azimuth coordinate is constantly updated as the kite propagates further in the X direction. The azimuth angle starts at a high value and is decreased as the length of the tether increases. This results in uniform trajectories in the inertial coordinates centered around the high power zone and constant tension, as seen in Figs. 6.16 and 6.17 respectively.

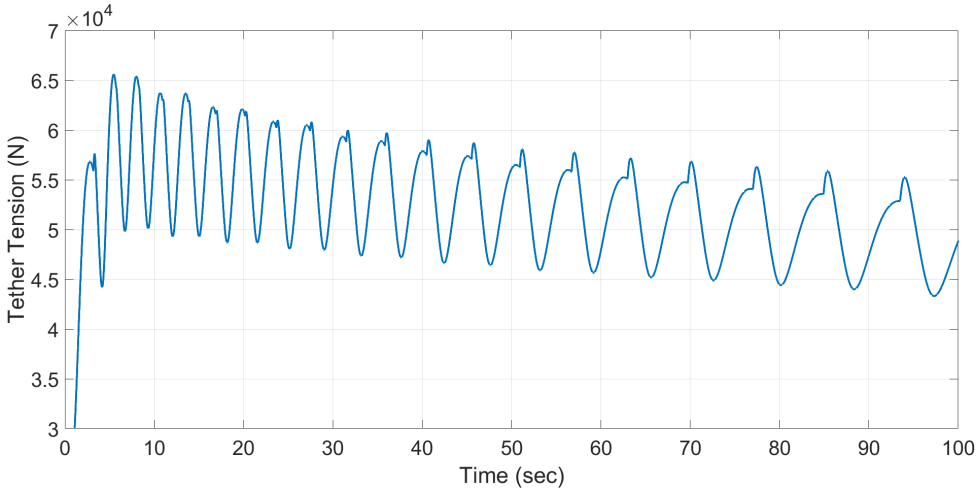

Figure 6.15 An illustration of reduction in the tension force when the reference tracking points are defined in the local frame, due to the deviation of the flight path from the mean Y-axis

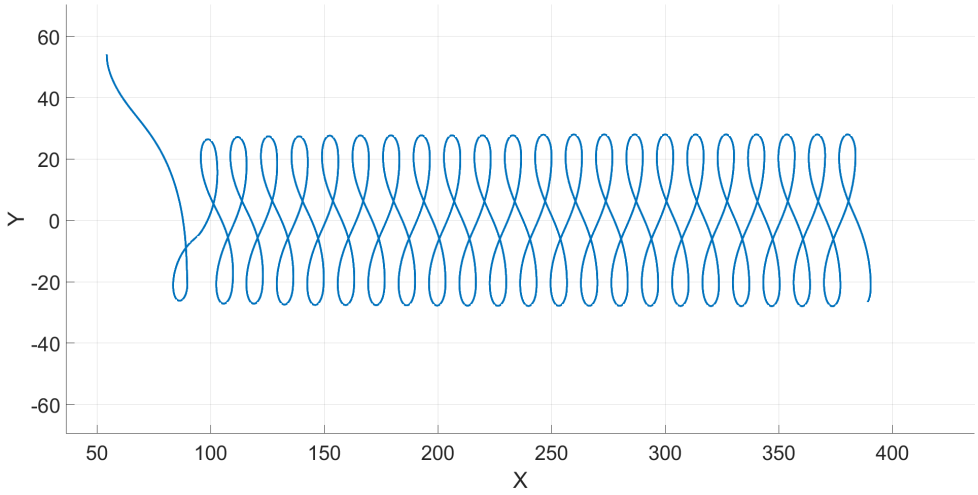

Figure 6.16 Kite's flight path in X-Y plane in the inertial frame, with the reference tracking points also defined in the inertial frame.

6.3 Power Generation With Trajectory Control

A complete production cycle of the kite is simulated to analyze the system's power output. The trajectory controller optimized in Section 6.2 is implemented to maximize the power production of the kite during the traction phase.

A simple state controller is designed that switches between reel-out and reel-in states

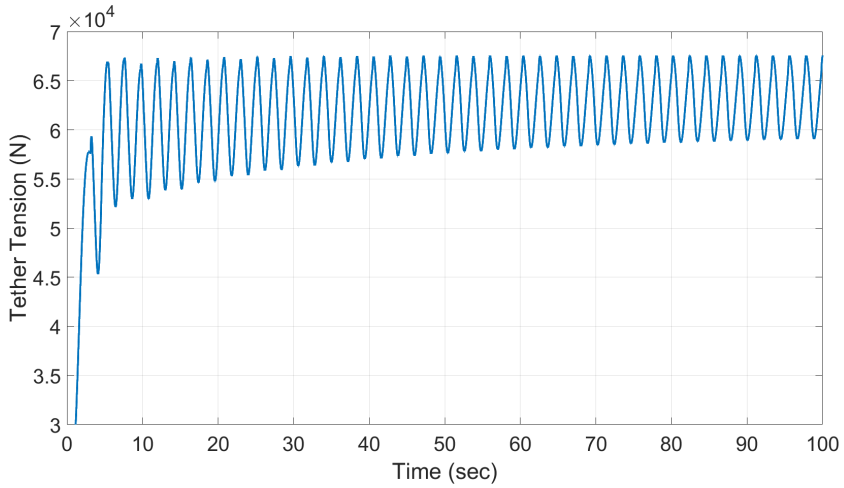

Figure 6.17 An illustration of a constant tether traction force obtained by defining the tracking reference points in the inertial frame.

as the tether reaches its maximum and minimum lengths, respectively. The reel-out and reel-in velocities are system control parameters to be defined. Higher reel-out velocities lead to higher power output but lower traction force, as indicated by Eq.(3.32). From the simulations performed, it is observed that power initially increases as the reel-out velocity is increased until an optimal value is reached and then decreases as the reel-out velocity is increased further. The optimum reel-out velocity is found very close to the value calculated by Lloyd (Loyd, 1980) as one-third of the wind speed. Similarly, the reel-in speed is another important control variable. Lower reel-in speeds lead to less power consumed during the retraction phase but increase the cycle time during which the system is not producing power, decreasing the system's overall efficiency. Higher reel-in speeds decrease the cycle time but increase the power consumption and make the kite difficult to control when retracting.

A similar state controller is designed that changes the kite's angle of attack between powered and depowered states. The powered state refers to the traction phase where the angle of attack is increased to increase the lift force and, consequently, the tether tension by increasing the lift coefficient as apparent from Eq.(3.22). During the retraction phase, the angle of attack is reduced to its minimum value to reduce the over tension to consume less power at the ground station. As stated in Section 3.3.4, the angle of attack needs to be limited to a certain range as a limitation of the thin airfoil

theory. It was noted in the experiments performed by Oehler and Schmehl (Oehler & Schmehl, 2018) that the angle of attack during the traction phase reaches a maximum value of 15° with lift coefficient as high as 1.6. Only the profile drag of the kite is considered, and the drag coefficient is kept constant. Considering the effects of tether drag, the drag coefficient is set as 0.3.

Table 6.2 Simulation parameters for a closed loop power production cycle with trajectory control

Initial Conditions		Control Variables	
Wind speed ($\mathbf{V_w}$)	10 m/s	Reel out velocity ($\dot{r}_{out}$)	3 m/s
Elevation angle ($\boldsymbol{\theta}$)	20°	Reel in velocity ($\dot{r}_{in}$)	-4 m/s
Azimuth angle ($\boldsymbol{\phi}$)	30°	Pitch angle (α_0) traction	10°
Initial tether length	100 m	Pitch angle (α_0) retraction	0°
Minimum tether length (r_{min})	100 m	Reference elevation (θ_{ref})	30°
Maximum tether length (r_{max})	300 m	Y reference coordinates	$\pm$20 m

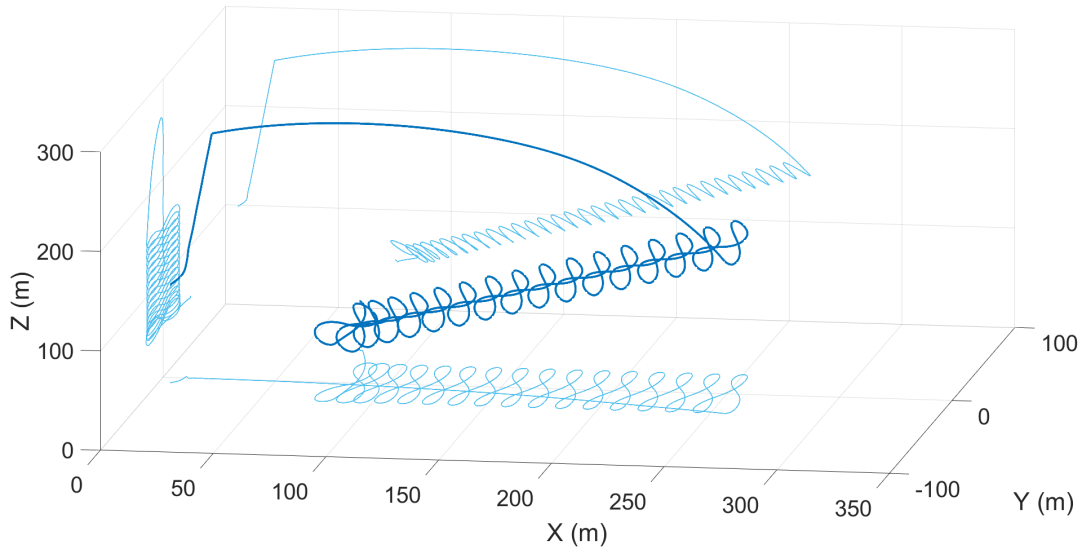

Figure 6.18 3-D trajectory of the kite plotted in the inertial frame for one power cycle.

The simulation parameters of the system are listed in Table 6.2. The kite's trajectory for a single power cycle is plotted in Fig.6.18. The kite is reeled out in the traction phase, flying a continuous figure-of-eight loops until the maximum tether length is

reached. The state controllers for the reel-out velocity and angle of attack are active during this stage. The controllers switch states as soon as the tether reaches its maximum length and the kite is reeled in. During the retraction phase, the elevation angle is increased to hover the kite in the low power zone of the wind window. The angle of attack is also decreased to depower the kite. The reel-in phase continues until the tether reaches its minimum length. The kite moves to its initial position, and the cycle is repeated. The change in state and control variables of the kite for one power cycle is shown in Figs. 6.20 and 6.19 respectively.

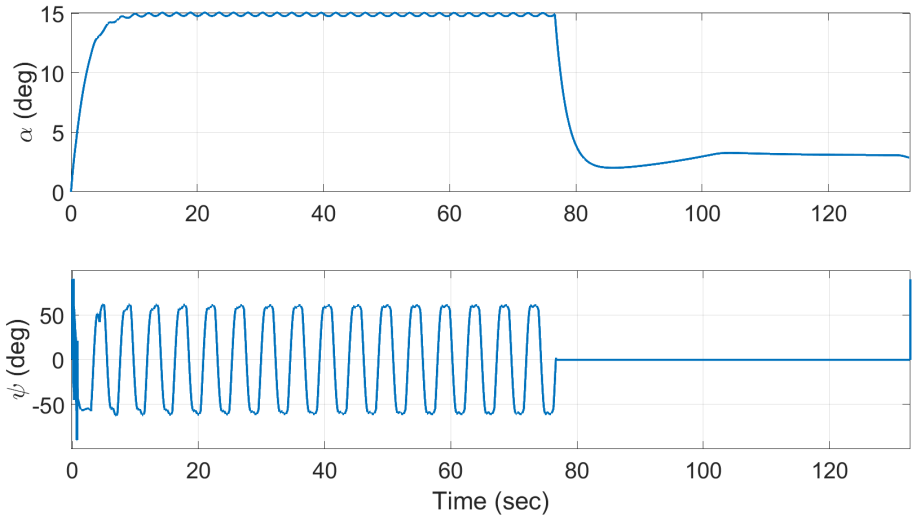

Figure 6.19 Control variables of the kite for one power cycle simulated with a wind speed of 10 $\mathrm{m/s}$

The power output for one power cycle is shown in Fig.6.21. The system produces an average power of 122 kW during the traction phase and consumes an average power of 14.5 kW in the retraction phase. The net power obtained for the complete cycle is 108 kW. The simulation is based on the kite specifications adapted from a prototype developed by Kitepower, which has a rated net power of 100 kW for a single cycle time of 100 seconds. The rated wind speed is unknown; however, the results shown in the simulation are considered close enough to the real-life data available. The wind speed specified as 10 $\mathrm{m/s}$ is a good estimate of wind speed at an average elevation of 150 m, which is the maximum height of the kite with a maximum tether length of 300 m. Another AWE company, skysails, has a rated power of 100 - 200 kW in an

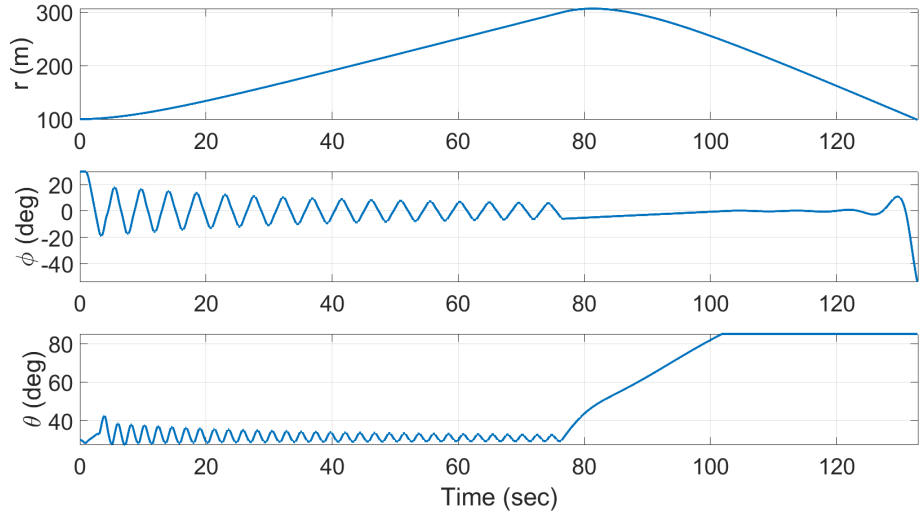

Figure 6.20 State variables of the kite for one power cycle simulated with a wind speed of 10 $\mathrm{m/s}$

operating wind range of 3 - 25 $\mathrm{m/s}$, with a kite surface area of 90 - 180 m^2 and a maximum tether length of 800 m.

6.3.1 Efficiency analysis

The system's overall performance in terms of the power output and cycle efficiency is also calculated based on the discussion presented in Section 2.3. The power harvesting factor of the kite model simulated is determined as ζ = 6.5. Hence, it can extract $\frac{27}{16}\zeta$ = 10.9 times more power than a wind turbine with a swept area A of 50 m^2. Consequently, it can also be stated that a kite wing with a surface area A of 50 m^2 can extract as much power from the wind as a wind turbine with a swept area of $\frac{27}{16}\zeta\ A$ = 548 m^2.

The cyclic efficiency is considered another good performance metric to evaluate the power output of a pumping AWE system. The efficiencies are calculated for the system power output shown in Fig.6.21 and listed in Table 6.3. The energy produced during the reel-out phase is shown as the area under the power curve in green. Energy consumed during the reel-in phase is shown in red. The average power generated during the reel-out and reel-in phases are shown with dashed green and red lines,

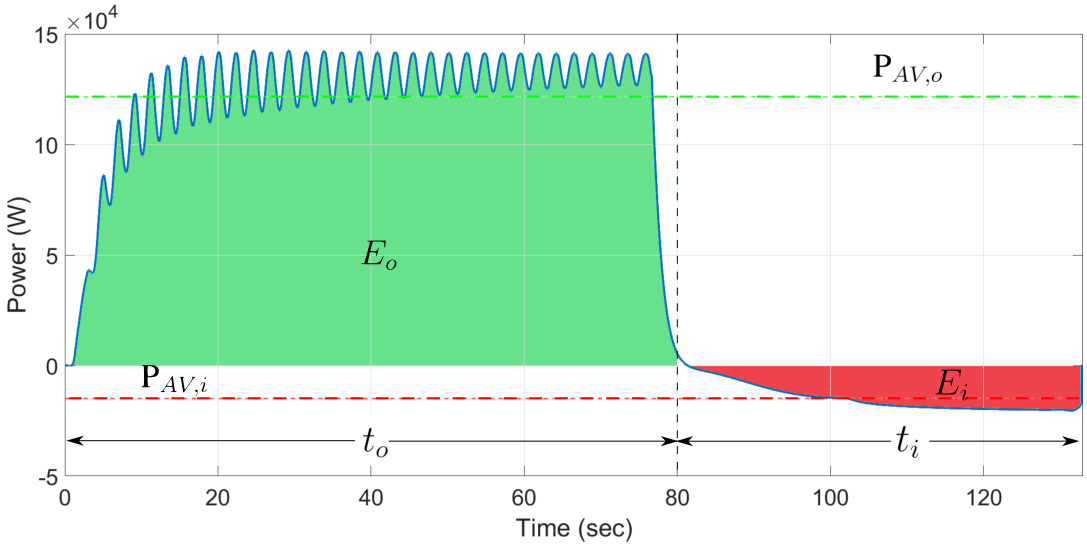

Figure 6.21 Power production of a kite for one power cycle, for a wind speed of 10 $\mathrm{m/s}$.

respectively. A cycle effeciecny of 51 % is observed. The cycle effeciency has a major depedance on the duration of reel-in and reel-out phases, and can be furter improved by adjusting the reeling speeds. Other efficiencies related to the electrical machinery at the ground station are neglected here.

Table 6.3 Performance parameters of a 50 m^2 kite operated at $\mathbf{V_w}$ = 10 $\mathrm{m/s}$, with $\dot{r_{out}}$ = 3 $\mathrm{m/s}$ and $\dot{r_{in}}$ = -4 $\mathrm{m/s}$

Parameter	Value	Description
$\mathrm{P}_{AV,o}$	122 kW	Average mechanical power produced - reel out phase
$\mathrm{P}_{AV,i}$	14.5 kW	Average mechanical power consumed - reel in phase
t_o	66 sec	Duration of reel-out phase
t_i	50 sec	Duration of reel-in phase
D	57%	Duty cycle
η_p	91%	Pumping efficiency
P_{AV}	63.7 kW	Average mechanical power over the complete cycle
η_{cyc}	51%	Cycle efficiency

6.3.2 Effect of reeling speeds

The choice of system parameters to obtain an efficient power cycle is based on the desired outcome and system constraints. For example, if the system requires to operate at its maximum power output, and the kite size and wind velocity are constrained, the efficiency of the power cycle can be increased by adjusting the reel-in velocity. Higher reel-in velocities will improve the duty cycle by shortening the amount of time power is consumed at the ground station but will also increase the magnitude of power consumption, hence decreasing the pumping efficiency of the system. Table 6.4 shows the simulation results for a reel-in velocity of -8 $\mathrm{m/s}$. A 10 % increase in the cycle efficiency is observed.

Table 6.4 Performance parameters of a 50 m^2 kite operated at $\mathbf{V_w}$ = 10 $\mathrm{m/s}$, with $\dot{r_{out}}$ = 3 $\mathrm{m/s}$ and $\dot{r_{in}}$ = -8 $\mathrm{m/s}$

Parameter	Value	Description
$P_{AV,o}$	122 kW	Average mechanical power produced - reel out phase
$P_{AV,i}$	41 kW	Average mechanical power consumed - reel in phase
t_o	66 sec	Duration of reel-out phase
t_i	25 sec	Duration of reel-in phase
D	72%	Duty cycle
η_p	85%	Pumping efficiency
P_{AV}	74.6 kW	Average mechanical power over the complete cycle
η_{cyc}	61%	Cycle efficiency

Faster reel-in speeds are not always the optimal solution to improve the system's efficiency, as there is a risk of losing control when the kite is reeled in very fast. If the system is not required to operate at its maximum power all the time, the efficiency of the power cycle can be significantly improved by increasing the time the kite stays in the traction phase. This can be achieved with lower reel-out speeds. Table 6.5 shows simulation results for a reel-out speed of 1 $\mathrm{m/s}$ and a reel-in speed of -3 $\mathrm{m/s}$. A cycle efficiency of 73 % is obtained. Based on the analysis of different simulations, the optimum reel-in speeds are around three times the reel-out speeds. A similar

correlation of the reeling speeds is observed in the results published by (Fechner & Schmehl, 2013).

Table 6.5 Performance parameters of a 50 m^2 kite operated at $\mathbf{V_w}$ = 10 $\mathrm{m/s}$, with $\dot{r_{out}}$ = 1 $\mathrm{m/s}$ and $\dot{r_{in}}$ = -3 $\mathrm{m/s}$

Parameter	Value	Description
$P_{AV,o}$	76.5 kW	Average mechanical power produced - reel out phase
$P_{AV,i}$	7.1 kW	Average mechanical power consumed - reel in phase
t_o	200 sec	Duration of reel-out phase
t_i	66 sec	Duration of reel-in phase
D	75%	Duty cycle
η_p	96%	Pumping efficiency
P_{AV}	55 kW	Average mechanical power over the complete cycle
η_{cyc}	73%	Cycle efficiency

6.3.3 Effect of atmospheric wind speed

So far, the simulations for the power production cycle have kept the wind speed at a constant value of 10 $\mathrm{m/s}$. AWE systems are, however, designed to harness high-speed winds at higher altitudes. The system's power production is observed at higher altitudes with minimum and maximum tether lengths redefined as 300 and 500 m, respectively. Assuming a constant wind of 15 $\mathrm{m/s}$, the results of the simulation are listed in Table 6.6. A noticeable increase in the power output of the system is observed. The average power produced during the production phase is 400 kW, and the average power over the complete power cycle is 277 kW.

A power output of 400 kW produced by a flexible wing of the comparable specification is experimentally not realized yet by tethered AWE systems with flexible wings. Larger prototypes are, however, being designed with more wing surface area to achieve a power production in the MW range. The hypothesis is also tested by the simulation model by using a kite with a surface area of around 150 - 200 m^2, and seems very plausible in the operating wind speed range of AWE systems.

Table 6.6 Performance parameters of a 50 m^2 kite operated at $\mathbf{V_w}$ = 15 $\mathrm{m/s}$, with $\dot{r_{out}}$ = 2.5 $\mathrm{m/s}$ and $\dot{r_{in}}$ = -6 $\mathrm{m/s}$

Parameter	Value	Description
$P_{AV,o}$	400 kW	Average mechanical power produced - reel out phase
$P_{AV,i}$	37 kW	Average mechanical power consumed - reel in phase
t_o	80 sec	Duration of reel-out phase
t_i	30 sec	Duration of reel-in phase
D	72%	Duty cycle
η_p	95%	Pumping efficiency
P_{AV}	277 kW	Average mechanical power over the complete cycle
η_{cyc}	69%	Cycle efficiency

The simulation model of the AWE kite derived in chapter 3 and the control architecture developed in chapter 5 is successfully implemented in this chapter to investigate the power potential of the kite. All the simulations are performed with the end goal of maximizing power production. The control parameters that effect the power output are tuned to operate in their optimal state, which maximizes power production. The only control variables that need consideration are the reeling speeds chosen according to the system-specific requirements. If the overall efficiency of the power cycle is in question, the optimal reel-in speeds are observed as three times the reel-out speed.

CHAPTER 7

CONCLUSION

Over the past decade, the focus of research in wind energy has shifted significantly from wind turbines to AWE Systems. AWE technology is rapidly progressing from experimental prototypes to commercial feasibility. The following are the two main factors encouraging the development and study of AWE systems. The first is that AWE devices may stay airborne by either aerodynamic or aerostatic forces. Therefore the need for a hefty and costly tower and other structural elements is made redundant. As a result, the frequently high construction, assembly, logistics, and installation costs are greatly reduced. The second compelling aspect of AWE systems is their potential to function at altitudes higher than those reached by the blade tips of the existing wind turbines. The high altitude is achieved by reeling out the tether in the traction phase.

The thesis provides an in-depth but not overly extensive analysis that might serve as a manuscript for those attempting to get acquainted with AWE technology works or as a reference for individuals looking for more focused studies in a specific field of AWE research. The main goals of the thesis are the development of a simulation model in Matlab/Simulink©that accurately simulates the dynamics of a kite in three dimensions and the development of a control architecture that controls the flight path in the desired trajectory and optimizes it for maximizing the power generation potential of the system.

It is verified through the simulations that the power production of a kite is significantly increased when it is flown in a specific trajectory. The comparison of the results presented in Chapter 5 shows that the net power produced for an arbitrary trajectory is twice more than that of a kite flying without a pre-defined trajectory. Furthermore, the power output can be increased to as much as ten times by imposing figure-of-

eight trajectories, as observed in Chapter 6. A laying figure-of-eight is the most desired trajectory found in the literature for an AWE system to maximize its power production. Controlling the kite's path in the desired trajectory is challenging due to its high operational velocities, distance from the ground to high operational altitudes, restrictions on the size and weight of the controller if it is airborne with the kite and its continuous autonomous operation. Although Non-linear Model Predictive Controllers (NMPC) are used extensively in the literature, they are not necessarily required for a regular kite operation.

For the control of the AWE system, a decentralized control approach is introduced in Chapter 5 that separates the control laws for the tethered kite and the ground station. The thesis focuses on the control law of the airborne kite in terms of its flight trajectory. A cascaded linear feedback controller designed consists of an outer and inner loop. The outer loop executes a guidance algorithm that generates a reference trajectory.The outer loop generates a reference course angle, and the inner loop utilizes PID control to minimize the course angle error. The reference course angle is fed through a low pass filter to smoothen the output for sudden changes in the reference signal due to the bang-bang controller. The kite's trajectory is modified by adjusting the filter's cut-off frequency and the PID gains.

The effect of different parameters on K_P is investigated. It is related to the wind speed as $K_P = 3\ \mathbf{V_w}$. As the wind speed increases, the steering input must be deflected more to execute a turning maneuver. Integral action has no specific contribution as the error is updated continuously over time. It is also shown that a derivative action is required for robust control as it avoids overshoots in high wind speed and keeps the flying smoothly in the desired trajectory. Upon investigating, K_D is related to the wing span b as $K_D = 0.5\ b$. The controller is tested for different wind speeds in the range of 5 - 25 $\mathrm{m/s}$, and the desired tracking results are achieved for every simulation.

The effect of the cut-off frequency on the trajectory output and power production is also analyzed. It is shown that higher cut-off frequencies produce smaller trajectories with sharp turns around the reference tracking points. Lower cut-off frequencies tend to produce wider trajectories. Consequently, the power output of trajectories restricted around the reference tracking points is higher, provided the points are defined

in the high power zone limits. For a constant wind speed of 15 $\mathrm{m/s}$, the average tension in the tether is reduced from 160 kN to 100 kN as the cut-off frequency is decreased from 1.74 $\mathrm{rad/s}$ to 1.13 $\mathrm{rad/s}$. The trajectories are also observed to change if the cut-off frequency is kept constant and the wind conditions are changed. To obtain a steady trajectory for any wind speed in the range of operational range of 5 - 25 $\mathrm{m/s}$, the cut-off frequency is related to the wind speed as $\omega_{cut-off} = k_c \mathbf{V_w}$. The cut-off gain k_c is found manually for a few intervals in the operational wind speed range. A 3rd order polynomial is fitted between the intervals, and K_c is evaluated automatically for any given wind speed.

Elevation of the kite affects its power potential. An average tension force of 60 kN is observed at an elevation of $60°$. If the elevation is reduced to $30°$, a significant increase is observed as the average tension jumps to 130 kN. The result at first appears to go against one of the core ideas of AWE systems, which is to harness wind energy at higher altitudes. It is crucial to emphasise that the wind velocity remains constant throughout the simulation. However, the wind speed rises with increasing height above the ground. The high-altitude wind is reached by increasing the tether length.

As a final contribution to the thesis, the power output of the AWE system is analyzed. The falcon-100 kite developed by Kitepower is taken as a physical reference to compare the results. The simulations are performed for 10 $\mathrm{m/s}$ wind speed. All the control variables have been optimized to produce the maximum power at any operating conditions, except for the reeling speeds. As the literature calculates, the optimal reel-out speed is one-third of the wind speed. However, the relation is only useful if the power output during the traction phase is considered. A complete power cycle includes reeling back the tether with a certain reel-in velocity that consumes power at the ground station. Setting the reel-out velocity as one-third of the wind speed is not the best metric as the efficiency of the complete power cycle is now in question, which is greatly affected by the reel-in speeds. Selecting the reeling velocities is regarded as a design parameter. If the overall efficiency of the power cycle is in question, the optimal reel-in speeds are observed as three times the reel-out speed. A cycle efficiency as high as 73% is possible with a reel-out speed of 1 $\mathrm{m/s}$ and reel-in speed of -3 $\mathrm{m/s}$. The average power produced during this cycle's reel-out is 76.5 kW. The maximum average power produced during the reel-out phase is 122 kW for a reel-out velocity

of 3 $\mathrm{m/s}$. This is comparable to the power produced by the falcon prototype used as a reference.

Lastly, It is also pertinent to highlight the environmental benefits of using an AWE system as opposed to the conventional methods of electricity production using fossil fuels. An AWE system with a net average power of 100 kW, similar to the one utilized in Chapter 6, is considered. The annual energy production if the system is run for 24 hours a day is calculated as $100\,\mathrm{kW} \times 24\,\mathrm{hours} \times 365\,\mathrm{days} = 876\,\mathrm{MWh/year}$. For a more realistic estimate, a capacity factor of 75 %, as reported by Enerkite, is considered, which estimates the power output at 657 $\mathrm{MWh/year}$. According to the data presented by U.S Energy Information Administration in regards to electricity generation and carbon emissions, the electricity produced from such an AWE system saves about 660,000 kg tonnes of annual carbon emissions as compared to electricity production from coal, 460,000 kg of annual carbon emissions as compared to electricity production from heavy oil, and 330,000 kg tonnes of annual carbon emissions as compared to electricity production from natural gas. Future prototypes with power capacities in the MW range would thus significantly contribute to reducing the overall carbon footprint of the electricity generation sector.

7.1 Future Work

The model can be simulated for any wind conditions and kite specifications to get an initial idea of the power potential for further analysis. The accuracy can be improved by adapting a higher-order model for the kite, such as a rigid body or high-fidelity model. The effects of tether mass and drag can also be added to improve the accuracy further. The trajectory is optimized by tuning a minimum number of control variables to maintain simplicity in the model and analyse each parameter's effect distinctively. The control logic can be upgraded by using NMPC laws that improve the control accuracy of a tethered flight which is a fast, strongly nonlinear, unstable and highly constrained process.

Developing autonomous launching and landing techniques for AWE pumping systems based on both flexible and stiff wings is possibly one of the most important tech-

nical difficulties in AWE research. The AWE power plant's operation expenses will be influenced by the complexity and automation and by how reliable these launching and landing mechanisms are. How competitive and at what power scale AWE pumping systems will be in relation to current conventional wind energy technologies will be determined by these expenses, combined with maintenance costs.

AWE's economic, social and environmental aspects can also be investigated by comparing it with wind turbines and other renewable and conventional energy sources. It is essential to comprehend how people view and react to technology for it to succeed. Concerns regarding the technology might impede adoption if they are not taken seriously, raising project developers' expenses and reducing their ability to contribute to renewable energy targets.

REFERENCES

Anderson, J. (2005). *Introduction to flight*. McGraw-Hill Higher Education. https://books.google.com.cy/books?id=pW8U-UddgDMC

Anderson, J. (2001). *Fundamentals of aerodynamics*. McGraw-Hill. https://books.google.com.cy/books?id=CaBTAAAAMAAJ

Argatov, I., & Silvennoinen, R. (2010). Energy conversion efficiency of the pumping kite wind generator. *Renewable Energy*, *35*, 1052–1060. https://doi.org/10.1016/j.renene.2009.09.006

Beard, R., & McLain, T. (2012). *Small unmanned aircraft: Theory and practice*. Princeton University Press. https://books.google.com.cy/books?id=YqQtjhPUaNEC

Behrooz, F., Mariun, N., Marhaban, M., Mohd Radzi, M. A., & Ramli, A. (2018). Review of control techniques for hvac systems—nonlinearity approaches based on fuzzy cognitive maps. *Energies*, *11*, 495. https://doi.org/10.3390/en11030495

Berndt, M. (2015). Influence of concrete mix design on co2 emissions for large wind turbine foundations. *Renewable Energy*, *83*, 608–614. https://doi.org/https://doi.org/10.1016/j.renene.2015.05.002

Betz, A. (1926). *Wind-energie und ihre ausnutzung durch windmühl.* Vandenhoeck.

Birkeland, C. (2011). *Assessing the life cycle environmental impacts of offshore wind power generation and power transmission in the north sea* (Master's thesis). Institutt for energi-og prosessteknikk.

Breukels, J., & Ockels, W. (2005). Tethered "kiteplane" design for the laddermill project. *World Wind Energy Conference, Melbourne, Australia, 2005*.

Breukels, J., & Ockels, W. (2008). Analysis of complex inflatable structures using a multi-body dynamics approach. *49th AIAA/ASME/ASCE/AHS/ASC Structures, Structural Dynamics, and Materials Conference, Schaumburg, IL, USA, April 7-10, 2008*. https://doi.org/10.2514/6.2008-2284

British Petroleum. (2019). Bp statistical review of world energy 2019. https://www.bp.com/content/dam/bp/business-sites/en/global/corporate/pdfs/energy-economics/statistical-review/bp-stats-review-2019-full-report.pdf

Canale, M., Fagiano, L., & Milanese, M. (2009). Kitegen: A revolution in wind energy generation [WESC 2006 Advances in Energy Studies]. *Energy*, *34*(3), 355–361. https://doi.org/https://doi.org/10.1016/j.energy.2008.10.003

Canale, M., Fagiano, L., Ippolito, M., & Milanese, M. (2007). Control of tethered airfoils for a new class of wind energy generator, 4020–4026. https://doi.org/10.1109/CDC.2006.376775

Cherubini, A., Papini, A., Vertechy, R., & Fontana, M. (2015). Airborne wind energy systems: A review of the technologies. *Renewable and Sustainable Energy Reviews*, *51*, 1461–1476. https://doi.org/https://doi.org/10.1016/j.rser.2015.07.053

Corke, P. (2011). *Robotics, vision and control - fundamental algorithms in matlab®* (Vol. 73). Springer.

Cousins, D. S., Suzuki, Y., Murray, R. E., Samaniuk, J. R., & Stebner, A. P. (2019). Recycling glass fiber thermoplastic composites from wind turbine blades. *Journal of cleaner production*, *209*, 1252–1263.

De Groot, S. (2010). *Modelling the dynamics of an arc-shaped kite for control law design: Design of a rigid body model for real-time simulation using a multi-body reference*.

Diehl, M. (2013). Airborne wind energy: Basic concepts and physical foundations. In U. Ahrens, M. Diehl, & R. Schmehl (Eds.), *Airborne wind energy* (pp. 3–22). Springer Berlin Heidelberg. https://doi.org/10.1007/978-3-642-39965-7_1

Diehl, M., Magni, L., & De Nicolao, G. (2004). Efficient nmpc of unstable periodic systems using approximate infinite horizon closed loop costing. *Annual Reviews in Control*, *28*(1), 37–45. https://doi.org/https://doi.org/10.1016/j.arcontrol.2004.01.011

Diehl, M., Uslu, I., Findeisen, R., Schwarzkopf, S., Allgöwer, F., Bock, H. G., Bürner, T., Gilles, E. D., Kienle, A., Schlöder, J. P., & Stein, E. (2001). Real-time optimization for large scale processes: Nonlinear model predictive control of a high purity distillation column. In M. Grötschel, S. O. Krumke, & J. Rambau

(Eds.), *Online optimization of large scale systems* (pp. 363–383). Springer Berlin Heidelberg. https://doi.org/10.1007/978-3-662-04331-8_20

Energy Information Administration. (2019a). World energy balances 2019. https://www.iea.org/reports/world-energy-balances-2019

Energy Information Administration. (2019b). World energy statistics 2019. https://www.iea.org/reports/world-energy-statistics-2019

Energy Information Administration. (2020). Annual energy outlook 2020. https://https://www.eia.gov/outlooks/aeo/pdf/electricity_generation.pdf

Erhard, M., & Strauch, H. (2012). Control of towing kites for seagoing vessels. *IEEE Transactions on Control Systems Technology*, *21*. https://doi.org/10.1109/TCST.2012.2221093

Etkin, B. (1959). *Dynamics of flight: Stability and control*. Wiley. https://books.google.com.cy/books?id=6BoIAQAAIAAJ

EWEA. (2022). The european wind energy association.

Fagiano, L., Zgraggen, A., Morari, M., & Khammash, M. (2013). Automatic crosswind flight of tethered wings for airborne wind energy: Modeling, control design, and experimental results. *IEEE Transactions on Control Systems Technology*, *22*. https://doi.org/10.1109/TCST.2013.2279592

Fagiano, L. M. (2009). *Control of tethered airfoils for high-altitude wind energy generation* (PhD dissertation). Politecnico di Torino.

Fechner, U., & Schmehl, R. (2013). Model-based efficiency analysis of wind power conversion by a pumping kite power system. https://doi.org/10.1007/978-3-642-39965-7_14

Fechner, U., van der Vlugt, R., Schreuder, E., & Schmehl, R. (2015). Dynamic model of a pumping kite power system. *Renewable Energy*, *83*, 705–716. https://doi.org/https://doi.org/10.1016/j.renene.2015.04.028

Furey, A., & Harvey, I. (2007). Evolution of neural networks for active control of tethered airfoils. *Proceedings of the 9th European Conference on Advances in Artificial Life*, 746–755.

Gros, S., Zanon, M., & Diehl, M. (2013). A relaxation strategy for the optimization of airborne wind energy systems. *2013 European Control Conference (ECC)*, 1011–1016. https://doi.org/10.23919/ECC.2013.6669670

Houska, B., & Diehl, M. (2007). Optimal control for power generating kites. *2007 European Control Conference (ECC)*, 3560–3567. https://doi.org/10.23919/ECC.2007.7068861

Ilzhöfer, A., Houska, B., & Diehl, M. (2007). Nonlinear mpc of kites under varying wind conditions for a new class of large-scale wind power generators. *International Journal of Robust and Nonlinear Control*, *17*, 1590–1599. https://doi.org/10.1002/rnc.1210

IndustryARC. (2022). *Airborne wind energy (awe) market– forecast (2022-2027)*. IndustryARC.

International Energy Agency. (2019). Renewables, market analysis and forecast from 2019 to 2024. https://www.iea.org/reports/renewables-2019

IRENA. (2019). *Renewable power generation costs in 2018* (tech. rep.). Abu Dhabi, The International Renewable Energy Agency.

Jehle, C., & Schmehl, R. (2014). Applied tracking control for kite power systems. *Journal of Guidance, Control, and Dynamics*, *37*. https://doi.org/10.2514/1.62380

JUN, J. Y., Hua, M.-D., & Amar, F. (2014). A trajectory tracking control design for a skid-steering mobile robot by adapting its desired instantaneous center of rotation. *Proceedings of the IEEE Conference on Decision and Control*, *2015*. https://doi.org/10.1109/CDC.2014.7040100

Kamien, M., & Schwartz, N. (2013). *Dynamic optimization, second edition: The calculus of variations and optimal control in economics and management*. Dover Publications. https://books.google.com.cy/books?id=liLCAgAAQBAJ

Karki, J. (2002). *Active low-pass filter design*. Texas Instruments.

Lansdorp, B., & Ockels, W. (2005). Design of a 100 mw laddermill for wind energy generation from 5 km altitude. *7th World Congress on Recovery Recycling and Reintegration (digitaal)*.

Lansdorp, B., Remes, B., & Ockels, W. (2005). Design and testing of a remotely controlled surfkite for the laddermill. *World Wind Energy Conference, Melbourne, Australia, 2005*.

Lansdorp, B., Ruiterkamp, R., & Ockels, W. (2007). Towards flight testing of remotely controlled surfkites for wind energy generation. In *Aiaa atmospheric flight mechanics conference and exhibit*. https://doi.org/10.2514/6.2007-6643

Liu, Z., Zhao, Y., Zhou, Y., & Guan, F. (2020). Modeling, simulation and test results analysis of tethered undersea kite based on bead model. *Renewable Energy*, *154*, 1314–1326. https://doi.org/https://doi.org/10.1016/j.renene.2020.03.013

Loyd, M. (1980). Crosswind kite power (for large-scale wind power production). *Journal of Energy*, *4*(3), 106–111. https://doi.org/10.2514/3.48021

Malcolm, D., & Hansen, A. (2002). Windpact turbine rotor design study: June 2000june 2002 (revised). https://doi.org/10.2172/15000964

Martínez, E., Sanz, F., Pellegrini, S., Jiménez, E., & Blanco, J. (2009). Life-cycle assessment of a 2mw rated power wind turbine: Cml method. *International Journal of Life Cycle Assessment - INT J LIFE CYCLE ASSESS*, *14*, 52–63. https://doi.org/10.1007/s11367-008-0033-9

McKenna, R., v.d. Leye, P. O., & Fichtner, W. (2016). Key challenges and prospects for large wind turbines. *Renewable and Sustainable Energy Reviews*, *53*, 1212–1221. https://doi.org/https://doi.org/10.1016/j.rser.2015.09.080

Melin, T. (2000). A vortex lattice matlab implementation for linear aerodynamic wing applications.

Ockels, W. J. (2001). Laddermill, a novel concept to exploit the energy in the airspace. *Aircraft Design*, *4*(2), 81–97. https://doi.org/https://doi.org/10.1016/S1369-8869(01)00002-7

Oehler, J., & Schmehl, R. (2018). Aerodynamic characterization of a soft kite by in situ flow measurement. *Wind Energy Science*, *4*, 1–21. https://doi.org/10.5194/wes-4-1-2019

Payne, P. R., & McCutchen, C. (1976). Self-erecting windmill [US Patent 3,987,987]. https://patents.google.com/patent/US3987987#patentCitations

Ritchie, H., & Roser, M. (2020). Co and greenhouse gas emissions. *Our World in Data*. https://ourworldindata.org/co2-and-other-greenhouse-gas-emissions

Rizvi, S. M. A. H., Bastas, A., & Liyanage, K. (2022). Sustainability assessment of electricity generation technologies: A transition pathway for pakistan. *International Journal of Sustainable Energy*, *0*(0), 1–22. https://doi.org/10.1080/14786451.2022.2039141

Sánchez-Arriaga, G., García-Villalba, M., & Schmehl, R. (2017). Modeling and dynamics of a two-line kite. *Applied Mathematical Modelling*, *47*, 473–486. https://doi.org/https://doi.org/10.1016/j.apm.2017.03.030

Stäblein, A. R., Hansen, M. H., & Pirrung, G. (2017). Fundamental aeroelastic properties of a bend–twist coupled blade section. *Journal of Fluids and Structures*, *68*, 72–89.

Thresher, R., & Laxson, A. (2006). Advanced wind technology: New challenges for a new century. *European Wind Energy Conference Athens, Greece*.

Vakitbilir, N., Hilal, A., & Direkoglu, C. (2022). Hybrid deep learning models for multivariate forecasting of global horizontal irradiation. *Neural Computing and Applications*, *34*. https://doi.org/10.1007/s00521-022-06907-0

Veers, P., Dykes, K., Lantz, E., Barth, S., Bottasso, C. L., Carlson, O., Clifton, A., Green, J., Green, P., Holttinen, H., Laird, D., Lehtomäki, V., Lundquist, J. K., Manwell, J., Marquis, M., Meneveau, C., Moriarty, P., Munduate, X., Muskulus, M., … Wiser, R. (2019). Grand challenges in the science of wind energy. *Science*, *366*(6464). https://doi.org/10.1126/science.aau2027

Williams, P. (2006). Optimal wind power extraction with a tethered kite. *Collection of Technical Papers - AIAA Guidance, Navigation, and Control Conference 2006*, *2*. https://doi.org/10.2514/6.2006-6193

Williams, P., Lansdorp, B., & Ockels, W. (2007). Flexible tethered kite with moveable attachment points, part i: Dynamics and control. In *Aiaa atmospheric flight mechanics conference and exhibit*. https://doi.org/10.2514/6.2007-6628

Williams, P., Lansdorp, B., & Ockels, W. (2008). Optimal cross-wind towing and power generation with tethered kites. *Journal of Guidance Control and Dynamics - J GUID CONTROL DYNAM*, *31*, 81–93. https://doi.org/10.2514/1.30089

Williams, P., Lansdorp, B., Ruiterkamp, R., & Ockels, W. (2008). Modeling, simulation, and testing of surf kites for power generation. *AIAA Modeling and Simulation Technologies Conference and Exhibition, Honolulu, Hawaii, 18-21 August, 2008*. https://doi.org/10.2514/6.2008-6693

Worrell, E., Price, L., Martin, N., Hendriks, C., & Meida, L. O. (2001). Carbon dioxide emissions from the global cement industry. *Annual Review of Energy and the Environment*, *26*(1), 303–329. https://doi.org/10.1146/annurev.energy.26.1.303

Zillmann, U., & Bechtle, P. (2018). Emergence and economic dimension of airborne wind energy", booktitle="airborne wind energy: Advances in technology de-

velopment and research. In R. Schmehl (Ed.). Springer Singapore. https://doi.org/10.1007/978-981-10-1947-0_1